Mineralogy, petrology, and oxygen-isotope compositions of magnetite $\pm$ fayalite assemblages in CO3, CV3, and LL3 chondrites

Alexander N. KROT [1*], Patricia M. DOYLE[2], Kazuhide NAGASHIMA [1], Elena DOBRICĂ [1], and Michail I. PETAEV[3]

[1]School of Ocean, Earth Science and Technology, Hawai'i Institute of Geophysics and Planetology, University of Hawai'i at Mānoa, Honolulu, Hawai'i 96822, USA
[2]International School of Cape Town, 4 Edinburgh Close, Western Cape, Wynberg 7708, South Africa
[3]Department of Earth and Planetary Sciences, Harvard University, Cambridge, Massachusetts 02138, USA
[*]Corresponding author. E-mail: sasha@higp.hawaii.edu

Abstract–We report on the mineralogy, petrology, and O-isotope compositions of magnetite and fayalite (Fa_{90-100}) from several metasomatically altered and weakly metamorphosed carbonaceous (Y-81020 [CO3.05], EET 90043 [CO3.1], MAC 88107 [CO3.1-like], and Kaba [oxidized Bali-like CV3.1]) and unequilibrated ordinary chondrites (UOCs; Semarkona [LL3.00], MET 00452 [LL3.05], MET 96503 [LL3.05], EET 910161 [LL3.05], Ngawi [LL3.0−3.6 breccia], and Vicência [LL3.2]). In MAC 88107, EET 90043, and Kaba, nearly pure fayalite (Fa_{98-100}) associates with phyllosilicates, magnetite, Fe,Ni-sulfides, and hedenbergite ($Fs_{\sim 50}Wo_{\sim 50}$), and occurs in all chondritic components—chondrules, matrices, and refractory inclusions. In UOCs, nearly pure fayalite (Fa_{95-98}) associates with phyllosilicates and magnetite, and occurs mainly in matrices and fine-grained chondrule rims. Oxygen-isotope compositions of fayalite and magnetite in UOCs, COs, CVs, and MAC 88107 are in disequilibrium with those of chondrule olivine and low-Ca pyroxene phenocrysts, and plot along mass-dependent fractionation lines with slope of ~0.5, but different $\Delta^{17}O$ (~+4.3 ± 1.4‰, −0.2 ± 0.6‰, −1.5 ± 1‰, and −1.8 ± 0.8‰, respectively). Based on the mineralogical observations, thermodynamic analysis, O-isotope compositions, and recently reported experimental data, we infer that (1) fayalite and magnetite in COs, CVs, MAC 88107, and UOCs resulted from aqueous fluid–rock interaction on the chondrite parent asteroids that occurred at low local water-to-rock mass ratios (0.1−0.4) and elevated temperatures (~100−300 °C), and (2) $\Delta^{17}O$ of fayalite and magnetite reflects O-isotope compositions of aqueous fluids on the host meteorite parent bodies. The observed differences in $\Delta^{17}O$ of fayalite–magnetite assemblages in UOCs, CVs, COs, and MAC 88107 suggest that water ices that accreted into the ordinary chondrite and carbonaceous chondrite parent asteroids had different $\Delta^{17}O$, implying spatial and/or temporal variations in O-isotope compositions of water in the protoplanetary disk.

INTRODUCTION

Iron-rich olivine (FeO-rich olivine—from ferroan olivine ~Fa_{50} to nearly pure fayalite Fa_{90-100}) is one of the major minerals in matrices of unequilibrated ordinary chondrites (UOCs) and weakly to moderately metamorphosed (petrologic type 3) CV (Vigarano type), CK (Karoonda type), and CO (Ornans type) carbonaceous

chondrites, which generally experienced aqueous/ metasomatic alteration to a relatively small degree (e.g., Zolensky et al. 2008; Brearley and Krot 2013; Dobrică and Brearley 2020). Iron-rich olivine appears to be absent in matrices of extensively aqueously altered carbonaceous chondrites (CM2 [Murchison type], CR2 [Renazzo type], and CI1 [Ivuna type]); pristine carbonaceous chondrites, which largely avoided thermal

metamorphism and/or aqueous alteration (e.g., Acfer 094 [C3.0 ungrouped] and CR3s); and highly reduced, enstatite (EH and EL) and Kakangari-like chondrites (e.g., Nagahara 1984; Brearley 1993, 1996; Weisberg et al. 1996; Greshake 1997; Brearley and Jones 1998; Scott and Krot 2014; Brearley and Krot [2013] and references therein). In spite of its ubiquitous presence, the origin of matrix ferroan olivine remains controversial. Two kinds of models are being discussed in the literature—(1) high-temperature, nebular (e.g., Palme and Fegley 1990; Weinbruch et al. 1990; Hua and Buseck 1995; Weisberg et al. 1997; Dohmen et al. 1998; Weisberg and Prinz 1998; Lauretta and Buseck 2003); and (2) relatively low-temperature, asteroidal (Wasson and Krot 1994; Kojima and Tomeoka 1996; Hutcheon et al. 1998; Krot et al. 1998, 2000, 2004, 2006; Brearley 1999; Zolotov et al. 2006; Jogo et al. 2009, 2010, 2011; Dobrică and Brearley 2011, 2014, 2020; Doyle et al. 2015; Dobrică et al. 2017a, 2017b, 2018; Marrocchi et al. 2018).
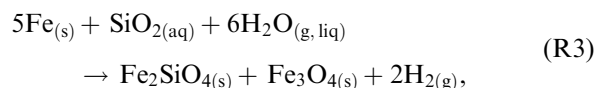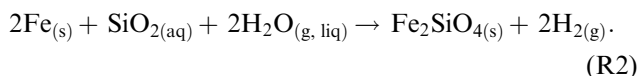
According to the nebular models, ferroan olivine formed as a result of high-temperature (1170−1260 K at a total pressure of 10^{-4} to 10^{-5} bars) oxidation of metal by a gas produced by evaporation of solids in nebular regions where water ice and silicate dust were enriched by a factor of >300 relative to solar dust/gas ratio of ~0.01:

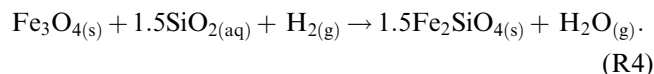$$2Fe_{(s)} + SiO_{(g)} + 3H_2O_{(g)} \rightarrow Fe_2SiO_{4(s)} + 3H_{2(g)}. \quad (R1)$$
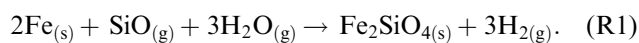
However, thermodynamic analysis of condensation in dust- and water-rich nebular regions (Ebel and Grossman 2000; Grossman et al. 2008; Fedkin and Grossman 2010; Grossman 2010) indicates that pure forsterite condenses prior to iron-bearing olivine and a condensation origin of the latter is inhibited by slow iron diffusion into the previously condensed forsterite. In addition, theoretical models of gravitational settling are unable to achieve dust enrichments of more than a factor of 120 (Cassen 2001), and those of inward migration of ice-bearing bodies are unable to achieve water enrichments greater than a factor of 10 relative to a system of solar composition (Ciesla and Cuzzi 2006). This limits fayalite content (=Fe/[Fe + Mg] × 100) in condensate olivine to ~2 mole% (Fedkin and Grossman 2010).

According to the asteroidal models, matrix FeO-rich olivine resulted from a fluid-assisted thermal metamorphism at 100−300 °C by several mechanisms (e.g., Krot et al. 2004):
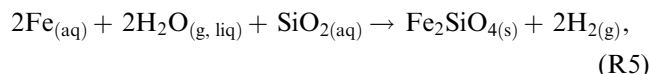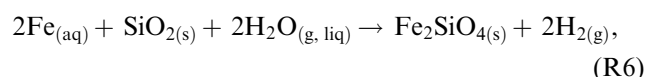(i) Oxidation of iron metal by water:

$$2Fe_{(s)} + SiO_{2(aq)} + 2H_2O_{(g, liq)} \rightarrow Fe_2SiO_{4(s)} + 2H_{2(g)}. \quad (R2)$$

$$5Fe_{(s)} + SiO_{2(aq)} + 6H_2O_{(g, liq)} \\ \rightarrow Fe_2SiO_{4(s)} + Fe_3O_{4(s)} + 2H_{2(g)}, \quad (R3)$$

(ii) Reduction of magnetite by hydrogen:

$$Fe_3O_{4(s)} + 1.5SiO_{2(aq)} + H_{2(g)} \rightarrow 1.5Fe_2SiO_{4(s)} + H_2O_{(g)}. \quad (R4)$$

(iii) Direct precipitation from a fluid:

$$2Fe_{(aq)} + 2H_2O_{(g, liq)} + SiO_{2(aq)} \rightarrow Fe_2SiO_{4(s)} + 2H_{2(g)}, \quad (R5)$$

(iv) Replacement of silica:

$$2Fe_{(aq)} + SiO_{2(s)} + 2H_2O_{(g, liq)} \rightarrow Fe_2SiO_{4(s)} + 2H_{2(g)}, \quad (R6)$$

(v) Replacement of low-Ca pyroxene:

$$Fe_{(aq)} + MgSiO_{3(s)} + H_2O_{(g, liq)} \\ \rightarrow (Fe, Mg)_2SiO_{4(s)} + Mg_{(aq)} + H_{2(g)}, \quad (R7)$$
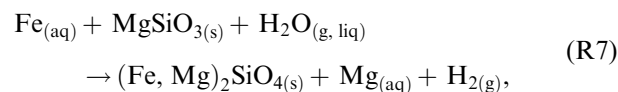
(vi) Replacement of forsteritic olivine:

$$Fe_{(aq)} + Mg_2SiO_{4(s)} + H_2O_{(g, liq)} \\ \rightarrow (Fe, Mg)_2SiO_{4(s)} + Mg_{(aq)} + H_{2(g)} \quad (R8)$$
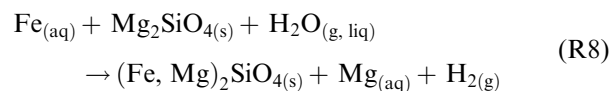
(vii) Dehydration of ferroan serpentine:

$$2(Fe, Mg)_3Si_2O_5(OH)_{4(s)} \\ \rightarrow 3(Fe, Mg)_2SiO_{4(s)} + SiO_{2(aq)} + 4H_2O_{(g, liq)}. \quad (R9)$$
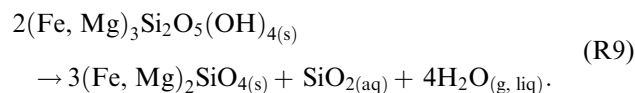
Note that only the first four mechanisms could result in the formation of nearly pure fayalite (Fa_{95-100}). Furthermore, recent experiments provide clear evidence that hydrothermal growth of elongated, iron-rich olivine can occur during thermal metamorphism in the presence of a fluid (220 °C, 0.4 W/R mass ratio, 6 days; Dobrica et al. 2017a, 2017b, 2018), as described previously in meteorites (Krot et al. 2004; Brearley 2009; Abreu and Brearley 2011; Dobrică and Brearley 2011, 2014). The results of these hydrothermal experiments show iron-rich olivine can form at low temperatures (220 °C), that is at the transition regime between aqueous alteration and thermal metamorphism (Brearley and Krot 2013). This is consistent with previous studies (Rasmussen et al. 1998; Zolotov et al. 2006), which suggest that two

variables appear to have a very important role in the formation of fayalite during hydrothermal growth, viz. the W/R ratio and the fluid composition.

To constrain the place, time, mechanisms, and conditions of FeO-rich olivine formation in chondrite matrices, we initiated a detailed study of iron-rich olivine-bearing assemblages (FeO-rich olivine, magnetite, andradite, hedenbergite, wollastonite, and kirschsteinite) in matrices and fine-grained rims of low petrologic type (3.0–3.3) ordinary and carbonaceous (CO, CV, and MAC 88107) chondrites.

Magnetite is a common secondary mineral in many aqueously altered ordinary and carbonaceous (CV, CK, CO, CM, CR) chondrites. It most likely formed on the chondrite parent bodies during aqueous fluid–rock interaction (e.g., Zolensky et al. 2008). Because magnetite mainly formed by oxidation of Fe,Ni-metal:

$$3Fe + 4H_2O_{(g, liq)} = Fe_3O_{4(s)} + 4H_{2(g)}, \qquad (R9)$$
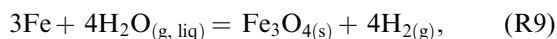
its $\Delta^{17}O$ ($= \delta^{17}O - 0.52 \times \delta^{18}O$) reflects oxygen isotopic composition of the fluid. In CO, CV, MAC 88107, and type 3 OCs, magnetite and fayalite often coexist (e.g., Doyle et al. 2015). If these minerals formed nearly contemporaneously during aqueous fluid–rock interaction on the chondrite parent asteroids, their $\Delta^{17}O$ values within an individual meteorite are expected to be similar (e.g., Choi et al. 1997, 2000). If this is the case, differences in $\delta^{18}O$ values of fayalite and magnetite can be used to constrain their formation temperature (Zheng 1991, 1993). If, however, formation of fayalite occurred in the solar nebula, prior to the formation of magnetite, their $\Delta^{17}O$ values are likely to be different. In addition, on a three-isotope oxygen diagram ($\delta^{17}O$ versus $\delta^{18}O$), oxygen isotopic composition of fayalite will most likely plot along the primitive chondrule mineral line with a slope of about one that reflects mixing of nebular reservoirs (Ushikubo et al. 2012).

Here, we report on the mineralogy, petrology, and high-precision in situ measured oxygen-isotope compositions of fayalite and magnetite in chondrules and matrices, and chondrule olivine and plagioclase/mesostases from MacAlpine Hills (MAC) 88107 (CO3.1-like), Yamato 81020 (CO3.05), Elephant Moraine (EET) 90043 (CO3.1), Kaba (CV$_{oxB}$3.1), Semarkona (LL3.00), EET 90161 (LL3.05), Meteorite Hills (MET) 00452 (LL3), MET 96503 (LL3), Ngawi (LL3.0–3.7 breccia), and Vicência (LL3.2). The mineralogy and oxygen-isotope compositions of magnetite and, occasionally, fayalite in some of these meteorites have been previously described by several research groups (e.g., Hua and Buseck 1995; Choi et al. 1997, 1998, 2000; Hua et al. 2005; Marrocchi et al. 2016). However, the reported

oxygen-isotope compositions of magnetite ± fayalite are often of low precision (2σ~3–4‰), and, in some cases, appear to be inconsistent or have been interpreted differently (see the Previous Results section).

PREVIOUS RESULTS

Fayalite–Magnetite Assemblages in CV3 Carbonaceous Chondrites

Nearly pure fayalite was first discovered in the Bali-like oxidized CV chondrites (CV$_{oxB}$) Kaba and Mokoia by Hua and Buseck (1995). Fayalite grains in these meteorites associate with magnetite, troilite, and pentlandite; reach up to 100 μm in size; and occur in the matrix, chondrules, and fine-grained rims around chondrules and Ca, Al-rich inclusions (CAIs). Hua and Buseck (1995) suggested fayalite formed through nebular reaction of gaseous SiO, released by decomposition of enstatite, with magnetite and sulfides under highly oxidizing conditions (H$_2$O/H$_2$ ratio much higher than the canonical solar nebula of ~5 × 10^{-4}; Lodders 2003). Subsequently, based on the mineralogical observations, including the presence of fayalite-bearing veins crosscutting fine-grained rims around chondrules, thermodynamic analysis, and ^{53}Mn-^{53}Cr isotope studies, it has been concluded that fayalite-bearing assemblages in Kaba and Mokoia formed during aqueous fluid–rock interaction on the CV chondrite parent asteroid (e.g., Hutcheon et al. 1998; Krot et al. 1998; Zolotov et al. 2006).

Using the UCLA Cameca ims-1270 and the ASU Cameca ims-6f, respectively, Choi et al. (2000) and Hua et al. (2005) reported relatively low-precision oxygen isotopic compositions ($\delta^{17,18}O$ ~3–4‰, 2σ) of fayalite and magnetite in Kaba and Mokoia (Figs. 1a and 1b). Both groups found that on a three-isotope oxygen diagram ($\delta^{17}O$ versus $\delta^{18}O$), the compositions of magnetite and fayalite plot along a mass-dependent fractionation line close to the terrestrial fractionation (TF) line with an average $\Delta^{17}O$ ~ −0.2 ± 1.5‰ (2SE). There is, however, a disagreement between these two data sets. Compositions of the Kaba fayalite and magnetite reported by Hua et al. (2005) have significantly different $\delta^{18}O$ than those reported by Choi et al. (2000), −5 to +10‰ and +17 to +24‰ versus +10 to +13‰ and +10 to +13‰, respectively. Assuming contemporaneous formation of magnetite and fayalite in equilibrium with an aqueous solution, these differences may significantly affect the temperature estimates of fayalite and magnetite formation (Zheng 1991, 1993).

Oxygen isotopic compositions of magnetite and olivine in chondrules from Allende (CV3.6) and Ningqiang (CV3 anomalous) measured with the UCLA
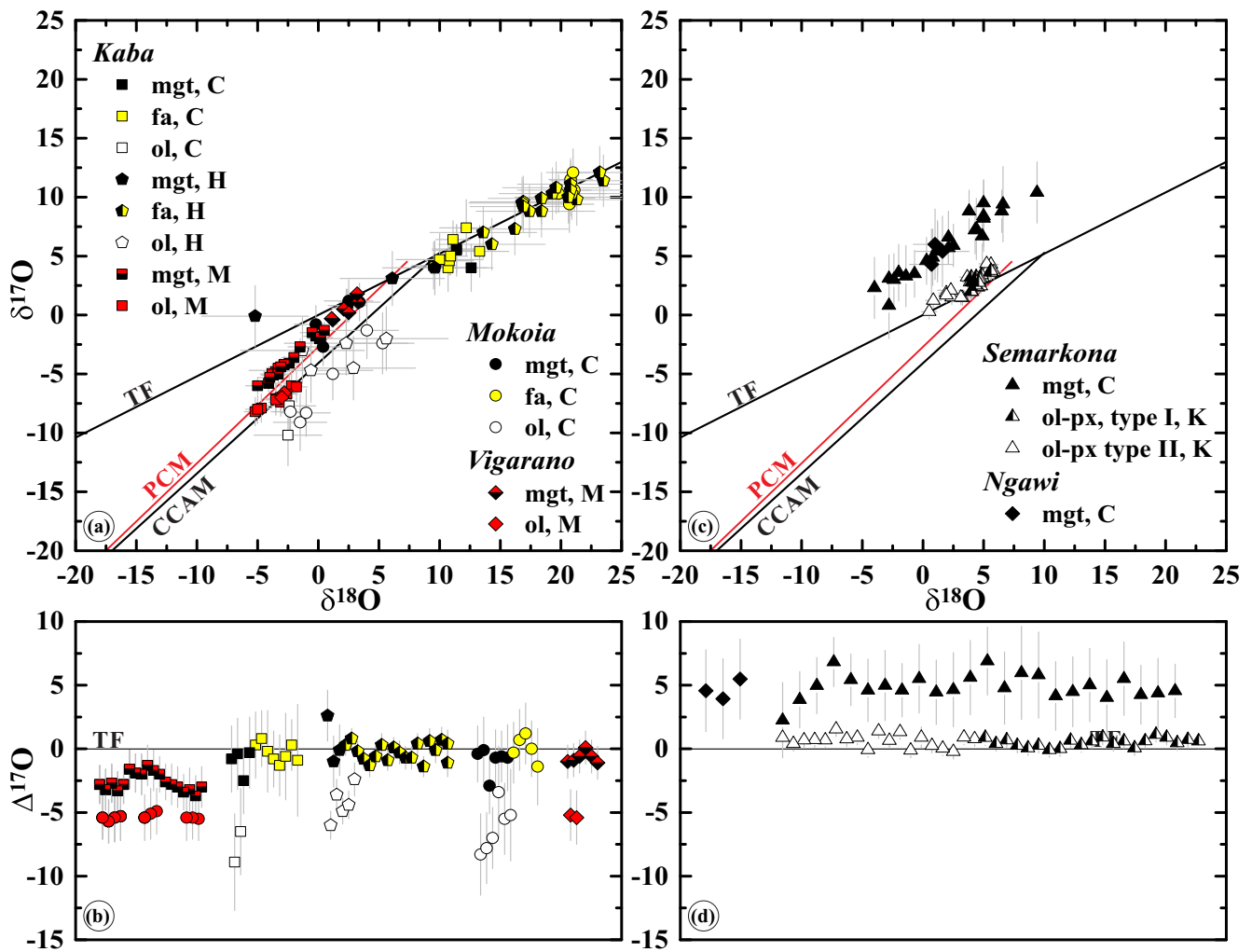
Fig. 1. Previously published oxygen-isotope compositions of magnetite, fayalite, and chondrule olivine, and low-Ca pyroxene phenocrysts from (a, b) CV3 carbonaceous chondrites Kaba (CV3.1), Mokoia (CV3.6), and Vigarano (CV3.1−3.4), and (c, d) ordinary chondrites Semarkona (LL3.00) and Ngawi (LL3.0−3.7 breccia). Data from Choi et al. (1998, 2000; labeled as "C"), Hua et al. (2005; labeled as "H"), Kita et al. (2010, labeled as "K"), and Marrocchi et al. (2016, labeled as "M"). fa = fayalite; mgt = magnetite; ol = type I and II chondrule ferromagnesian olivine; px = type I and II chondrule low-Ca pyroxene; CCAM = carbonaceous chondrite anhydrous mineral line (defined by Clayton et al. 1977); PCM = primitive chondrule mineral line (defined by Ushikubo et al. 2012); TF = terrestrial fractionation line. (Color figure can be viewed at wileyonlinelibrary.com.)

Cameca ims-1270 and the ASU Cameca ims-6f have been reported by Choi et al. (1997), Choi and Wasson (2003), and Hsu et al. (2006), respectively (Figs. 1c and 1d). The Allende magnetites show a smaller range of $\delta^{18}O$ (from −7.1 to −4.8‰; there are, however, several outliers) compared to those from Ningqiang (from −4.9 to 4.2‰ [Choi and Wasson 2003] and from −17.8 to −1.6‰ [Hsu et al. 2006]); ranges of $\Delta^{17}O$ are similar (from −3.6 to −0.6‰ and from −4.9 to −1.9‰, respectively; typical uncertainty is ~±2‰). On a three-isotope oxygen diagram, compositions of the Allende and Ningqiang magnetites plot along mass-dependent fractionation lines with a slope of ~0.5 and $\Delta^{17}O$ of

−2.4 ± 1.9‰ and −3 ± 2‰ (2SE), respectively. Chondrule olivines ($\Delta^{17}O$ range from −8.9 to −3.8‰) are in isotope disequilibrium with magnetites and on a three-isotope oxygen diagram plot along mass-independent fractionation line (due to large uncertainties on $\delta^{18}O$, ~±3‰, discrimination between the CCAM [carbonaceous chondrite anhydrous mineral] line having a slope of ~0.94 [Clayton et al. 1977] and PCM [primitive chondrule mineral] line having a slope of ~1.0 [Ushikubo et al. 2012] is precluded, Fig. 1c). Choi et al. (1997) and Choi and Wasson (2003) concluded that magnetite in Allende and Ningqiang formed during parent body oxidation of metal by water

that experienced some oxygen-isotope exchange with anhydrous silicates.

Recently, Marrocchi et al. (2016) reported high-precision oxygen-isotope compositions ($\delta^{17,18}$O ~0.5−1‰, 2σ) of magnetite and olivine in chondrules from Kaba and the reduced CV3.1 chondrite Vigarano using the Nancy Cameca ims-1290 (Figs. 1a and 1b). The magnetites show a range of δ^{18}O (−5 to 3.3‰) and Δ^{17}O (−3.7 to 0.1‰); they are in isotope disequilibrium with chondrule olivines (Δ^{17}O ~−5‰). On a three-isotope oxygen diagram, the Kaba and Vigarano magnetites plot close to the PCM line (Fig. 1a). In contrast to previously reached conclusions (Choi et al. 2000; Hua et al. 2005), Marrocchi et al. (2016) suggested that magnetite in Kaba and Vigarano chondrules crystallized from chondrule melts under highly oxidizing conditions. We note, however, that considering the observed range in δ^{18}O of ~8‰ and the typical uncertainties of Δ^{17}O of magnetite reported by Marrocchi et al. (2016), ~1.5‰ (2σ), the limited range of Δ^{17}O does not allow the distinction between mass-independent and mass-dependent fractionation lines (Figs. 1a and b). Oxygen-isotope compositions of fayalite, which appear to have formed contemporaneously with magnetite (e.g., Krot et al. 1998; Doyle et al. 2015), could help resolve this issue and provide additional constraints on the formation conditions of fayalite–magnetite–bearing assemblages (see the Results section).

Fayalite–Magnetite Assemblages in the CO3.1-like Carbonaceous Chondrite MAC 88107

The mineralogy, petrology, and ^{53}Mn-^{53}Cr systematics of fayalite in the CO3.1-like carbonaceous chondrite MAC 88107 have been previously reported by Krot et al. (2000). Fayalite coexists with magnetite; hedenbergite; Fe,Ni-sulfides; and, occasionally, kirschsteinite. Based on the mineralogical observations, thermodynamic analysis, and ^{53}Mn-^{53}Cr dating of fayalite, it was concluded that these secondary minerals formed in situ during relatively low-temperature (100−300 °C) aqueous alteration 9−18 Ma after the formation of CAIs, which are the oldest solids originating in the solar system (e.g., Amelin et al. 2002; Bouvier and Wadhwa 2010; Connelly et al. 2012), and, in cosmochemistry are considered to represent the beginning of the solar system formation. It was subsequently shown that the large range and apparently young formation ages of fayalite in MAC 88107 inferred by Krot et al. (2000) were incorrect: the former was due to a poorly defined initial ^{53}Mn/^{55}Mn ratio in the solar system ([0.8−4.5]×10^{-5}), whereas the latter resulted from improper standards used for Mn-Cr isotope measurements of fayalite. The currently inferred formation age of fayalite in MAC 88107 is 5.1$^{+0.5}_{-0.4}$ Ma after CV CAIs (Doyle et al.

2015). Oxygen-isotope compositions of fayalite and magnetite in MAC 88107 could provide additional constraints on the formation conditions of the fayalite-bearing assemblages.

Magnetite-Bearing Assemblages in CO3 Carbonaceous Chondrites

Magnetite replacing Fe,Ni-metal and associated with phyllosilicates, Fe,Ni-sulfides, ±Fe,Ni-carbides, ±fayalite, and ±hedenbergite is common in CO chondrites of low petrologic subtypes, for example, Yamato (Y) 81020 (CO3.0), Allan Hills (ALHA) 77307 (CO3.0), Dominion Range (DOM) 08006 (CO3.0), DOM 03238 (CO3.1), DOM 08004 (CO3.1), and EET 90043 (CO3.1; Brearley and Jones 1998; Grossman and Rubin 2006; Krot et al. 2013, 2017; Davidson et al. 2014; Howard et al. 2014; Rubin and Li 2019). However, only preliminary data on oxygen isotopic compositions of a limited number of magnetite grains from DOM 03238 have been previously reported (Choi et al. 2008). These compositions are similar to those of magnetite in CV chondrites: the weighted mean of Δ^{17}O is −2.3 ± 0.4‰; δ^{18}O range from 0.2 to 4 ± 0.8‰. Magnetite is in oxygen-isotope disequilibrium with chondrule olivine having Δ^{17}O of −5.2 ± 1.3‰. Based on these observations, Choi et al. (2008) concluded that magnetite in DOM 03238 formed by parent body alteration of preexisting metal. In addition, Kim et al. (2009) described wüstite (FeO) associated with magnetite, Fe,Ni-metal, and ±sulfide in DOM 03238, and concluded that it formed by reduction of magnetite during atmospheric passage.

Magnetite-Bearing Assemblages in Unequilibrated Ordinary Chondrites

Magnetite associated with phyllosilicates, Fe,Ni-carbides, Fe,Ni-metal, and Fe,Ni-sulfides in chondrules and matrices was described in a subset of UOCs of low petrologic subtypes, including meteorites studied here—Semarkona, Ngawi, and EET 90161 (Hutchison et al. 1987; Alexander et al. 1989; Krot et al. 1997; Grossman and Brearley 2005). Choi et al. (1998) reported the only in situ measured oxygen isotopic compositions of magnetite using the UCLA Cameca ims-1270 from Semarkona and Ngawi. The magnetites show a large range of δ^{18}O (−4 to 9.4‰) and very high Δ^{17}O (average value ~+5‰ with typical uncertainties of ~±3‰). Hitherto, the higher Δ^{17}O have been reported only for magnetite in cosmic symplectites in Acfer 094 (C3.0 ungrouped; Sakamoto et al. 2007). Magnetites are in oxygen-isotope disequilibrium with chondrule olivines and pyroxenes having Δ^{17}O of ~1‰ (Kita et al. 2010),

and on a three-isotope oxygen diagram plot along a regression line with a slope of ~0.7. Choi et al. (1998) concluded that magnetite in Semarkona and Ngawi formed in situ by the oxidation of Fe,Ni-metal by a limited amount of isotopically heavy water that was incorporated into the LL chondrite parent body and experienced some isotope exchange with anhydrous silicates. Doyle et al. (2015) first reported the presence of nearly pure fayalites in UOCs and their oxygen-isotope compositions ($\Delta^{17}O$ ~+5‰), but have provided only limited mineralogical description of their occurrences.

ANALYTICAL TECHNIQUES

Mineralogy and Petrology

Polished thin sections of MAC 88107, EET 90043, Y-81020, Kaba, Semarkona, EET 90161, MET 00452, MET 96503, Ngawi, and Vicência kindly provided by the Meteorite Working Group (Johnson Space Center), Natural History Museum (London), Natural History Museum (Paris), Smithsonian Institution, Arizona State University, and National Institute of Polar Research (Table 1) have been studied in reflected and transmitted light with an optical microscope and in backscattered electrons (BSE) with the University of Hawai'i (UH) scanning electron microscope (SEM) JEOL 5900LV and field emission electron microprobe (EPMA) JEOL JXA-8500F, both equipped with an energy-dispersive X-ray spectrometer. Electron microprobe analyses were performed with the UH JEOL JXA-8500F operated at 15 kV accelerating voltage, 20 nA beam current, and ~1 μm beam size using five wavelength spectrometers. For each element, counting times on both peak and background were 30 s. Minerals with known chemical compositions were used as standards: Verma garnet (Mn), San Carlos olivine (Fe, Mg, Si), fayalite (Fe), diopside (Ca, Si), anorthite (Al), orthoclase (K), albite (Na), chromite (Cr), sphene (Ti). Matrix effects were corrected using PAP procedures (Pouchou and Pichoir 1984). Electron microprobe analyses of fayalite, magnetite, hedenbergite, kirschsteinite, and chondrule olivines and pyroxenes measured for oxygen-isotope compositions are listed in Tables S1−S4 in supporting information.

Six electron transparent sections of representative areas of FeO-rich subhedral olivine overgrowths on type I and type II chondrule olivine fragments and isolated, subhedral to euhedral grains were prepared by the in situ focused ion beam (FIB) technique. For this sample preparation, we used the FEI Quanta 3D Dualbeam field emission gun (FEG) SEM/FIB operating at 30 kV at the University of New Mexico. A platinum protective layer (2 μm in thickness and 2 μm

Table 1. List of polished thin sections used in this study.

Chondrite	Classification	PTS	Source
MAC 88107	CO3.1-like	50	JSC
EET 90043	CO3.1	7	JSC
Y-81020	CO3.05	56	NIPR
Kaba	CV3.1	1052-1	SI
Kaba	-"-	HX3	ASU
Kaba	-"-	SG2	JSC
Kaba	-"-	35794	BMNH
Kaba	-"-	MP56	HU
Kaba	-"-	MP57	HU
EE 90161	LL3.05	15	JSC
MET 00426	LL3	16	JSC
MET 00452	LL3	18	JSC
MET 96503	LL3	7	JSC
MET 96503	LL3	14	JSC
MET 96503	LL3	17	JSC
Ngawi	LL3.0-3.7	2843-2	SI
Ngawi	-"-	44	UCLA
Semarkona	LL3.00	1805-5	SI
Semarkona	-"-	4128-4	SI

in width) was deposited on top of the regions of interest to avoid ion beam damage during the FIB sample preparation. The sections were transferred to Cu transmission electron microscope (TEM) half grids with an Omniprobe 200 micromanipulator. The final ion milling of the 2 μm thick sections (~20 μm in length and ~6 μm in width) to electron transparency was carried out with the samples attached to the TEM grids. The final thinning stages were performed at 5 kV with a Ga ion beam current of 10 pA.

Each FIB section was studied using a variety of TEM modes, including bright-field TEM imaging, high-angle annular dark-field scanning transmission electron microscopy (HAADF-STEM), selected area electron diffraction, and energy-dispersive X-ray spectroscopy (EDS). All imaging and analyses were carried out at 200 kV on a JEOL 2010F FEGTEM/scanning TEM. In situ EDS X-ray analyses and maps were obtained using an Oxford Instruments AZtec EDS system equipped with an Oxford X-MaxN 80T EDS detector. The Cliff–Lorimer thin film approximation was used for quantification of EDS data using theoretically determined k-factors. The individual EDS analyses were obtained by rastering the electron beam over the region or grain of interest (~10–100 nm) in STEM mode to minimize electron beam damage to the sample.

Oxygen-Isotope Measurements

Oxygen-isotope compositions of ferromagnesian olivine (Fa_{1-40}), fayalite (typically $Fa_{>90}$), magnetite, and

chondrule mesostasis/plagioclase were measured in situ with the UH Cameca ims-1280 secondary ion mass-spectrometer (SIMS or ion microprobe) using the analytical procedure described in detail by Makide et al. (2009). Prior to the measurements, the grains of interest were marked by an electron beam using JEOL LV5900 (for details see Nagashima et al. 2017). Grains larger than 10 μm in size were measured using a ~1 nA primary Cs^+ ion beam focused to ~5 μm. The beam was first rastered over a 10×10 $μm^2$ area for 250 s of presputtering to remove the carbon coating. Then, the raster size was reduced to 7×7 $μm^2$ for automated centering of the secondary beam to the mass spectrometer, followed by data collection. An energy window of 50 eV was used. A normal incident electron flood gun was used for charge compensation. Secondary ions of $^{16}O^-$, $^{17}O^-$, and $^{18}O^-$ were measured simultaneously in multicollection mode with the magnetic field controlled by a nuclear magnetic resonance probe. $^{16}O^-$ and $^{18}O^-$ were measured by multicollector Faraday cups (FCs) with low mass resolving power (MRP ~2000), while $^{17}O^-$ was measured using the axial monocollector electron multiplier (EM) in pulse counting mode with MRP of ~5600, sufficient to separate the interfering $^{16}OH^-$ signal. $^{16}OH^-$ signal was monitored after each measurement and was typically less than 3×10^5 cps in fayalite and less than 3×10^6 cps in magnetite, while typical $^{17}O^-$ count rate was ~2×10^5 cps. Contribution of $^{16}OH^-$ onto $^{17}O^-$ was corrected based on a peak/tail ratio. The correction was less than 0.05‰ in fayalite and less than 0.3‰ in magnetite. Huberty et al. (2010) described crystal orientation mass-dependent fractionation effects in oxygen isotopes for magnetite by the Wisconsin Cameca ims-1280 SIMS that significantly affect grain-to-grain precision of SIMS measurements. However, Caplan et al. (2015) were not able to attribute variations on O-isotope compositions of magnetite grains measured by the UH Cameca ims-1280 ion probe to crystal orientation; cracks crossing through the ion probe pit appear to lower $δ^{18}O$ values. Therefore, no crystal orientation effects on O-isotope composition of magnetite have been taken into account here; SIMS spots with cracks were eliminated.

Oxygen-isotope compositions of 5- to 10-μm-sized grains were measured using a 15−20 pA focused Cs^+ primary ion beam of 20 keV impact energy and ~2 μm in diameter. The ion microprobe was operated at −10 keV with a 50 eV energy window. $^{16}O^-$ and $^{18}O^-$ were measured on multicollector FC and EM, respectively. $^{17}O^-$ was measured with the axial EM. The MRP ($m/Δm$) for $^{16}O^-$ and $^{18}O^-$ was ~2000, and that for $^{17}O^-$ was ~5500, sufficient to separate interfering $^{16}OH^-$. A normal-incidence electron flood gun was used for charge compensation.

To verify the positions of the sputtered regions, the spots analyzed for oxygen isotopes were studied with secondary and BSE images using the UH JEOL JXA-8500F electron microprobe before and after SIMS measurements. X-ray elemental and/or BSE maps indicating locations of studied objects and BSE images of all SIMS spots in fayalite, magnetite, ferromagnesian olivine, and chondrule mesostases/plagioclase are shown in Figs. S5−S32 in supporting information.

Oxygen-isotope compositions are reported as $δ^{17}O$ and $δ^{18}O$, deviations from Vienna Standard Mean Ocean Water (VSMOW; $^{17}O/^{16}O_{VSMOW} = 0.000380$; $^{18}O/^{16}O_{VSMOW} = 0.002005$; De Laeter et al. 2003) in parts per thousand: $δ^{17,18}O_{SMOW} = ([^{17,18}O/^{16}O_{sample}]/[^{17,18}O/^{16}O_{VSMOW}] − 1) \times 1000$, and as deviation from the TF line, $Δ^{17}O$.

Data for fayalites, magnetites, plagioclase/mesostases, and ferromagnesian olivines were corrected using synthetic fayalite (Fa_{100}), magnetite, Miyake-jima anorthite, and San Carlos olivine ($Fa_{~11}$) standards, respectively. The reported 2σ uncertainties include both the internal measurement precision on an individual analysis and the external reproducibility for standard measurements during a given analytical session. The external reproducibility of the multiple analyses of the standard was ~0.7−1‰ and 1.5−2.5‰ (2σ) for both $δ^{17}O$ and $δ^{18}O$ using 1 nA and 15−20 pA beam, respectively. Oxygen-isotope compositions of individual minerals measured are listed in Tables 2−6 and shown later in Figs. 10−12. SIMS spots containing large cracks, holes, or inclusions, indicated by red color in Figures S2−S32, are excluded from Figs. 10−12.

RESULTS

Mineralogy and Petrology

MAC 88107 (CO3.1-like)

MAC 88107 is a CM/CO3.1-like carbonaceous chondrite (Krot et al. 2000). The mineralogy and petrology of the fayalite-bearing assemblages in MAC 88107 were characterized in detail by Krot et al. (2000). Here, we summarize our results only on the objects containing fayalite and/or magnetite measured for oxygen isotopes. Detailed TEM observations of two of these objects are included here.

There are three major textural occurrences of the fayalite-bearing assemblages in MAC 88107:

1. Isolated fayalite grains (up to 60 μm in size) and coarse-grained (10−20 μm in size) intergrowths of the compositionally nearly pure fayalite ($Fa_{98−100}$), hedenbergite ($Fs_{~50}Wo_{~50}$), magnetite, ±kirschsteinite ($CaFeSiO_4$), and ±Fe,Ni-sulfides in the matrix (Table EA2; Fig. 2). Fayalite grains have

Table 2. Oxygen-isotope compositions of magnetite and fayalite in MAC 88107 (CO3.1-like), Y-81020 (CO3.05), and EET 90043 (CO3.1).

Chondrite	Mineral	Object#	Spot#	$\delta^{18}O$	2σ	$\delta^{17}O$	2σ	$\Delta^{17}O$	2σ
MAC 88107	fa	mx#1	f1	13.9	±1.0	5.7	±1.2	−1.5	±1.3
-"-	-"-	-"-	f2	14.3	±1.1	5.7	±1.1	−1.7	±1.2
-"-	-"-	mx#2	f3	13.8	±1.0	5.5	±1.2	−1.6	±1.3
-"-	-"-	mx#3	f4	13.9	±0.9	4.6	±1.2	−2.6	±1.3
-"-	-"-	mx#4	f5	13.2	±0.9	4.6	±1.1	−2.3	±1.2
-"-	-"-	mx#5	f6	14.0	±0.9	6.0	±1.2	−1.3	±1.3
-"-	-"-	mx#6	f7	14.7	±1.1	5.5	±1.2	−2.2	±1.3
-"-	-"-	mx#7	f8	15.2	±1.0	6.8	±1.3	−1.1	±1.4
-"-	mgt	chd#7	m1	9.0	±1.6	3.4	±1.3	−1.2	±1.5
-"-	-"-	-"-	m2	9.2	±1.6	3.3	±1.3	−1.5	±1.5
-"-	-"-	-"-	m3	8.1	±1.6	2.9	±1.3	−1.4	±1.5
-"-	-"-	-"-	m4	9.3	±1.6	3.8	±1.3	−1.1	±1.5
-"-	-"-	chd#14	m5	10.1	±1.5	3.4	±1.3	−1.8	±1.5
-"-	-"-	-"-	m6	9.2	±1.5	3.2	±1.3	−1.6	±1.5
-"-	-"-	chd#15	m7	11.2	±1.5	3.5	±1.3	−2.3	±1.6
-"-	-"-	-"-	m8	12.5	±1.6	4.9	±1.3	−1.6	±1.5
-"-	-"-	-"-	m9	8.0	±1.7	1.9	±1.3	−2.3	±1.6
-"-	-"-	-"-	m10	11.9	±1.6	3.7	±1.3	−2.5	±1.6
-"-	-"-	mx#16	m11	12.0	±1.6	4.1	±1.3	−2.2	±1.5
-"-	-"-	-"-	m12	8.8	±1.6	2.7	±1.3	−1.9	±1.5
-"-	-"-	chd#16	m13	10.1	±1.6	3.8	±1.3	−1.5	±1.6
-"-	-"-	-"-	m14	12.0	±1.6	4.3	±1.3	−2.0	±1.5
-"-	-"-	-"-	m15	9.6	±1.6	3.0	±1.3	−2.0	±1.6
-"-	-"-	chd#10	m16	10.3	±1.6	3.4	±1.3	−1.9	±1.5
-"-	-"-	-"-	m17	11.2	±1.5	3.7	±1.3	−2.1	±1.5
-"-	-"-	-"-	m18	11.1	±1.6	4.2	±1.3	−1.6	±1.5
EET 90043	fa	mx#54	f1	9.8	±0.8	4.7	±0.6	−0.3	±0.8
-"-	-"-	mx#42	f2	10.6	±0.8	5.1	±0.7	−0.4	±0.8
-"-	-"-	-"-	f3	9.7	±0.8	4.4	±0.7	−0.7	±0.8
-"-	-"-	chd#32	f4	10.7	±0.8	4.7	±0.7	−0.9	±0.8
-"-	-"-	chd#151	f5	8.6	±2.8	3.8	±1.5	−0.6	±2.1
-"-	-"-	-"-	f6	7.1	±2.8	3.9	±1.5	0.2	±2.1
-"-	-"-	frg#150	f7	11.7	±2.9	6.3	±1.5	0.2	±2.1
-"-	-"-	mx#44	f8	8.2	±2.8	4.4	±1.5	0.1	±2.1
-"-	-"-	mx#134	f9	6.2	±2.8	3.6	±1.5	0.4	±2.1
-"-	-"-	frg#23	f10	9.7	±2.8	5.2	±1.6	0.1	±2.2
-"-	-"-	frg#125	f11	9.4	±2.8	5.1	±1.5	0.2	±2.1
-"-	mgt	chd#122	m1	10.7	±2.0	5.4	±1.1	−0.2	±1.5
-"-	-"-	mx#123	m2	10.0	±1.9	4.7	±1.0	−0.5	±1.4
-"-	-"-	mx#124	m3	8.0	±2.0	4.0	±1.1	−0.2	±1.5
-"-	mgt	mx#40	m4	10.3	±1.9	4.6	±1.0	−0.8	±1.4
-"-	-"-	-"-	m5	9.3	±2.0	4.1	±1.0	−0.7	±1.4
-"-	-"-	mx#37	m6	9.6	±1.9	4.7	±1.1	−0.3	±1.5
-"-	-"-	mx#146	m7	7.9	±1.9	3.3	±1.1	−0.8	±1.5
-"-	-"-	-"-	m8	6.6	±2.0	2.9	±1.0	−0.6	±1.4
-"-	-"-	chd#152	m9	7.8	±1.9	3.9	±1.0	−0.1	±1.5
-"-	-"-	chd#148	m10	11.7	±2.0	5.1	±1.0	−1.0	±1.5
-"-	-"-	-"-	m11	12.5	±2.0	6.3	±1.0	−0.2	±1.5
Y-81020	mgt	chd#56	m1	9.4	±1.1	4.9	±1.0	0.0	±1.1
-"-	-"-	-"-	m2	11.1	±1.1	5.9	±0.9	0.2	±1.1
-"-	-"-	chd#59	m3	12.2	±1.0	6.4	±0.9	0.0	±1.1
-"-	-"-	-"-	m4	11.9	±1.1	6.4	±0.9	0.2	±1.1
-"-	-"-	chd#60	m5	8.2	±1.1	4.3	±0.9	0.0	±1.1

Table 2. *Continued.* Oxygen-isotope compositions of magnetite and fayalite in MAC 88107 (CO3.1-like), Y-81020 (CO3.05), and EET 90043 (CO3.1).

Chondrite	Mineral	Object#	Spot#	$\delta^{18}O$	2σ	$\delta^{17}O$	2σ	$\Delta^{17}O$	2σ
-"-	-"-	-"-	m6	11.8	±1.1	5.8	±0.9	−0.4	±1.1
-"-	-"-	chd#2	m7	12.4	±1.1	6.0	±0.9	−0.4	±1.0
-"-	-"-	chd#5	m8	11.1	±1.0	5.9	±1.0	0.1	±1.1
-"-	-"-	-"-	m9	10.7	±1.1	5.7	±0.9	0.2	±1.1
-"-	-"-	chd#61	m10	10.5	±1.1	5.0	±0.9	−0.5	±1.1
-"-	-"-	-"-	m11	11.1	±1.1	5.2	±0.9	−0.5	±1.1
-"-	-"-	chd#6	m12	12.5	±1.1	6.4	±0.9	−0.1	±1.1
-"-	-"-	-"-	m13	12.1	±1.1	5.9	±0.9	−0.4	±1.1
-"-	-"-	chd#9	m14	11.7	±1.1	5.5	±0.9	−0.6	±1.1
-"-	-"-	-"-	m15	10.5	±1.1	4.9	±0.9	−0.5	±1.0

chd = chondrule; fa = fayalite; frg = chondrule fragment; gr = grain; mgt = magnetite; mx = matrix.

Table 3. Oxygen-isotope compositions of olivine grains in chondrules and chondrule fragments from MAC 88107 (CO3.1-like) and EET 90043 (CO3.1).

Chondrite	Object#	Spot#	$\delta^{18}O$	2σ	$\delta^{17}O$	2σ	$\Delta^{17}O$	2σ
Magnesian olivines from type I chondrules								
MAC 88107	frg#1	o3	−4.4	0.7	−8.2	0.8	−5.9	0.8
-"-	-"-	o4	−3.4	0.6	−8.2	0.7	−6.4	0.7
-"-	frg#2	o5	−1.9	0.6	−6.4	0.7	−5.4	0.8
-"-	frg#4	o7	−2.8	0.7	−7.6	0.7	−6.1	0.8
-"-	chd#5	o8	−2.1	0.8	−7.3	0.7	−6.2	0.8
-"-	chd#7	o12	−5.0	0.6	−9.9	0.7	−7.3	0.8
-"-	-"-	o13	−4.5	0.6	−9.5	0.7	−7.1	0.8
-"-	-"-	o14	−4.6	0.7	−9.3	0.7	−6.9	0.8
-"-	frg#8	o16	−4.2	0.6	−8.3	0.7	−6.2	0.8
-"-	-"-	o17	−4.5	0.7	−8.9	1.1	−6.6	1.2
-"-	chd#10	o19	−4.1	0.6	−8.9	0.7	−6.7	0.8
-"-	chd#13	o23	−4.3	0.8	−9.8	0.8	−7.6	0.9
-"-	-"-	o24	−8.5	0.7	−12.8	0.7	−8.4	0.8
-"-	-"-	o25	−8.3	0.7	−12.9	0.8	−8.6	0.8
-"-	-"-	o26	−7.9	0.8	−12.6	0.7	−8.5	0.8
-"-	-"-	o27	−0.2	0.7	−6.6	0.8	−6.5	0.8
-"-	chd#14	o28	−2.1	0.7	−8.4	0.8	−7.3	0.9
-"-	-"-	o29	−2.0	0.7	−8.2	0.7	−7.1	0.8
EET 90043	frg#67a	o1	−0.6	1.3	−4.5	0.8	−4.2	1.0
-"-	frg#45a	o2	−6.5	1.3	−9.8	0.7	−6.4	0.9
-"-	frg#42	o3	−3.1	1.2	−6.3	0.7	−4.7	0.9
-"-	chd#32	o4	−3.7	1.2	−6.6	0.7	−4.7	0.9
Ferroan olivines from type II chondrules								
MAC 88107	frg#3	o6	3.1	0.6	−0.8	0.7	−2.4	0.7
-"-	chd#6	o9	2.3	0.6	−2.4	0.7	−3.6	0.8
-"-	-"-	o10	2.7	0.6	−1.9	0.7	−3.3	0.7
-"-	-"-	o11	1.6	0.6	−2.8	0.7	−3.6	0.8
-"-	frg#9	o18	2.3	0.6	−1.6	0.7	−2.8	0.8
-"-	frg#11	o20	2.1	0.7	−2.4	0.7	−3.4	0.8
-"-	frg#12	o21	−0.1	0.6	−3.5	0.7	−3.5	0.7
-"-	-"-	o22	0.2	0.7	−3.1	0.7	−3.2	0.8
EET 90043	frg#67b	o5	3.0	1.2	−0.1	0.6	−1.6	0.9
-"-	frg#45b	o6	4.1	1.2	0.4	0.7	−1.7	0.9

chd = chondrule; frg = chondrule fragment.

Table 4. Oxygen-isotope compositions of olivine and plagioclase in chondrules from Kaba.

Mineral	PTS	Object#	Spot#	$\delta^{18}O$	2σ	$\delta^{17}O$	2σ	$\Delta^{17}O$	2σ
ol	1052-1	chd#2	o1	−4.9	±1.2	−7.4	±1.2	−4.8	±1.4
-"-	-"-	-"-	o2	−3.7	±1.2	−6.7	±1.3	−4.8	±1.4
-"-	-"-	-"-	o3	−3.4	±1.2	−6.4	±1.3	−4.6	±1.4
-"-	-"-	-"-	o4	−3.0	±1.2	−6.2	±1.3	−4.6	±1.4
-"-	-"-	-"-	o5	−4.1	±1.3	−6.6	±1.3	−4.4	±1.4
-"-	-"-	chd#6	o6	−7.0	±1.2	−8.8	±1.3	−5.1	±1.4
-"-	-"-	-"-	o7	−6.1	±1.2	−9.3	±1.2	−6.1	±1.4
-"-	-"-	-"-	o8	−5.6	±1.2	−8.4	±1.3	−5.5	±1.4
-"-	-"-	chd#1	o9	−6.6	±1.2	−8.7	±1.2	−5.2	±1.4
-"-	-"-	-"-	o10	−6.2	±1.2	−8.9	±1.3	−5.6	±1.4
-"-	-"-	-"-	o11	−5.5	±1.2	−9.1	±1.3	−6.2	±1.4
-"-	-"-	-"-	o12	−5.6	±1.2	−8.7	±1.2	−5.8	±1.4
-"-	-"-	-"-	o13	−5.5	±1.2	−8.2	±1.2	−5.4	±1.4
-"-	-"-	chd#4	o14	−8.4	±1.2	−11.1	±1.3	−6.8	±1.4
-"-	-"-	-"-	o15	−8.9	±1.2	−10.7	±1.3	−6.1	±1.4
-"-	-"-	-"-	o16	−6.8	±1.2	−9.9	±1.2	−6.4	±1.4
-"-	-"-	-"-	o17	−9.3	±1.2	−11.4	±1.2	−6.6	±1.4
-"-	-"-	-"-	o18	−8.2	±1.2	−11.6	±1.3	−7.3	±1.4
-"-	-"-	chd#10	o19	−6.5	±1.2	−9.9	±1.3	−6.5	±1.4
-"-	-"-	-"-	o20	−7.4	±1.2	−10.1	±1.3	−6.3	±1.4
-"-	-"-	-"-	o21	−6.6	±1.2	−9.5	±1.2	−6.1	±1.4
-"-	HX3	chd#1	o1	−9.3	±1.3	−12.0	±1.3	−7.2	±1.4
-"-	-"-	-"-	o2	−9.9	±1.3	−12.4	±1.4	−7.3	±1.5
-"-	-"-	-"-	o3	−8.5	±1.3	−12.1	±1.3	−7.6	±1.4
-"-	-"-	-"-	o4	−8.7	±1.3	−11.9	±1.3	−7.4	±1.4
-"-	-"-	chd#2	o5	−4.8	±1.2	−9.0	±1.3	−6.5	±1.4
-"-	-"-	-"-	o6	−5.2	±1.2	−8.9	±1.2	−6.3	±1.4
-"-	-"-	-"-	o7	−5.5	±1.2	−9.4	±1.3	−6.5	±1.4
-"-	SG2	chd#8	o1	−8.7	±0.8	−10.4	±0.6	−5.8	±0.7
pl	SG2	chd#3	p1	14.2	±0.9	7.1	±1.0	−0.3	±1.1
-"-	-"-	-"-	p2	15.1	±0.9	6.5	±1.1	−1.3	±1.2
-"-	-"-	chd#7	p3	13.4	±0.9	7.0	±1.1	0.0	±1.2
-"-	-"-	chd#9	p4	13.9	±0.9	6.6	±1.1	−0.6	±1.2
-"-	-"-	chd#8	p5	13.8	±0.9	7.0	±1.1	−0.2	±1.2
	-"-	chd#8	p6	13.0	±0.9	6.7	±1.1	−0.1	±1.2
-"-	HX3	chd#1	p10	15.6	±1.0	7.0	±1.1	−1.1	±1.2
-"-	-"-	-"-	p11	13.8	±0.9	6.8	±1.1	−0.4	±1.2
-"-	-"-	chd#2	p8	13.0	±0.9	6.7	±1.1	−0.1	±1.2
-"-	-"-	-"-	p9	13.8	±1.0	6.7	±1.1	−0.5	±1.2

chd = chondrule; ol = olivine; pl = plagioclase/mesostasis.

euhedral outlines and often contain inclusions of hedenbergite, magnetite, and sulfides. Although TEM study revealed the presence of saponite and serpentine in the MAC 88107 matrix, there is no evidence for corrosion of fayalite grains by the phyllosilicates.

2. Fayalite ± hedenbergite ± magnetite overgrowths on ferromagnesian olivines of type I and type II chondrules or chondrule fragments (Fig. 3). In a type II chondrule, composed of olivine phenocrysts, chromite, and the apparently hydrated mesostasis (as revealed by low totals of electron probe analyses), the olivine phenocrysts along a boundary with the mesostasis are overgrown by fayalite–hedenbergite rims containing inclusions of subhedral magnetite, suggesting partial leaching of the mesostasis prior to crystallization of the fayalite-bearing assemblage (Figs. 3a−c). The magnetite crystals are rare in fayalite, but abundant in hedenbergite (Fig. 3c). The overgrowths contain nearly pure fayalite (Fa_{98-100}; Table S2) and show no or little evidence for Fe-Mg interexchange with the host chondrule olivines (Figs. 3a−c). Occasionally, some fayalite overgrowths (~6.5 μm in

Table 5. Oxygen-isotope compositions of fayalite and magnetite in Kaba (CV3.1) chondrite.

Mineral	PTS	Object#	Spot#	$\delta^{18}O$	2σ	$\delta^{17}O$	2σ	$\Delta^{17}O$	2σ
fa	35794	mx#2a	f1	8.4	±1.1	3.0	±1.1	−1.4	±1.2
-"-	-"-	-"-	f2	8.5	±1.1	2.9	±1.1	−1.6	±1.2
-"-	-"-	mx#2b	f3	8.9	±1.1	3.5	±1.1	−1.1	±1.2
-"-	-"-	mx#1a	f4	8.0	±1.1	3.1	±1.1	−1.1	±1.2
-"-	-"-	mx#1b	f5	8.3	±1.1	2.4	±1.1	−1.9	±1.2
-"-	-"-	mx#1c	f6	8.3	±1.1	2.3	±1.1	−2.0	±1.3
-"-	-"-	mx#1d	f7	8.2	±1.1	2.3	±1.2	−2.0	±1.3
-"-	-"-	mx#3	f8	8.8	±1.1	2.0	±1.1	−2.6	±1.2
-"-	-"-	chd#5	f9	8.2	±1.1	3.2	±1.1	−1.0	±1.2
-"-	-"-	-"-	f10	6.9	±1.1	2.8	±1.1	−0.8	±1.2
-"-	-"-	-"-	f11	8.1	±1.1	2.9	±1.1	−1.3	±1.2
-"-	-"-	mx#7	f12	8.9	±1.1	2.8	±1.1	−1.8	±1.2
-"-	-"-	mx#8	f13	8.2	±1.1	3.0	±1.1	−1.3	±1.2
-"-	-"-	-"-	f14	8.4	±1.1	3.0	±1.1	−1.3	±1.2
-"-	-"-	frg#6	f15	7.7	±1.1	2.7	±1.0	−1.3	±1.2
-"-	1052-1	chd#2	m1	0.1	±1.1	−0.2	±1.0	−0.2	±1.1
-"-	-"-	-"-	m2	1.2	±1.0	0.2	±1.0	−0.4	±1.1
-"-	-"-	-"-	m3	2.0	±1.1	0.4	±1.0	−0.7	±1.1
-"-	-"-	-"-	m4	5.5	±1.0	1.6	±1.0	−1.3	±1.1
-"-	-"-	-"-	m5	−1.2	±1.2	−1.3	±1.0	−0.7	±1.2
-"-	-"-	-"-	m6	2.1	±1.1	0.0	±1.0	−1.1	±1.2
-"-	-"-	-"-	m7	2.3	±1.1	−0.2	±1.0	−1.4	±1.1
-"-	-"-	-"-	m8	2.8	±1.1	−0.5	±1.0	−1.9	±1.2
-"-	-"-	-"-	m9	4.6	±1.0	0.8	±1.0	−1.5	±1.1
-"-	-"-	-"-	m10	4.7	±0.9	1.1	±1.0	−1.3	±1.1
-"-	-"-	-"-	m11	3.6	±1.0	0.6	±1.0	−1.3	±1.2
-"-	-"-	-"-	m12	4.0	±1.0	0.6	±1.0	−1.5	±1.1
-"-	-"-	-"-	m13	2.7	±1.1	0.5	±1.0	−1.0	±1.2
-"-	-"-	-"-	m14	3.2	±1.1	0.6	±1.0	−1.1	±1.1
-"-	-"-	chd#6	m15	3.1	±1.1	−0.2	±1.0	−1.8	±1.1
-"-	-"-	-"-	m16	2.5	±1.2	0.0	±1.0	−1.3	±1.2
-"-	-"-	-"-	m17	3.5	±1.0	0.1	±1.0	−1.7	±1.1
-"-	-"-	-"-	m18*	2.5	±1.0	−0.8	±1.0	−2.1	±1.1
-"-	-"-	-"-	m19*	3.6	±1.1	−0.6	±1.0	−2.4	±1.1
-"-	-"-	chd#4	m20*	0.4	±1.4	−1.3	±1.1	−1.5	±1.3
-"-	-"-	-"-	m21	2.5	±1.1	−0.2	±1.0	−1.5	±1.1
-"-	-"-	-"-	m22	3.0	±1.0	0.0	±1.0	−1.6	±1.1
-"-	-"-	-"-	m23	4.1	±1.0	0.7	±1.0	−1.4	±1.2
-"-	-"-	-"-	m24	4.5	±1.0	0.5	±1.0	−1.9	±1.1
-"-	-"-	-"-	m25	3.0	±1.1	−0.2	±1.0	−1.7	±1.1
-"-	SG2	chd#7	m1	1.9	±1.7	0.7	±1.1	−0.3	±1.4
-"-	-"-	-"-	m2*	2.9	±1.5	1.7	±1.0	0.2	±1.3
-"-	-"-	-"-	m3	4.5	±1.3	2.2	±1.1	−0.2	±1.2
-"-	-"-	-"-	m4	5.0	±1.2	2.3	±1.1	−0.3	±1.3
-"-	-"-	-"-	m5	5.1	±1.3	2.1	±1.1	−0.5	±1.3
-"-	-"-	-"-	m6	3.5	±1.2	1.6	±1.1	−0.3	±1.3
-"-	-"-	-"-	m7	5.4	±1.4	1.4	±1.2	−1.4	±1.4
-"-	-"-	-"-	m8*	2.6	±1.3	0.2	±1.1	−1.2	±1.2
-"-	-"-	-"-	m9*	5.3	±1.4	0.2	±1.2	−2.6	±1.4
-"-	-"-	-"-	m10*	2.8	±1.7	−0.6	±1.1	−2.1	±1.4
-"-	-"-	chd#2	m11	−8.3	±1.4	−6.1	±1.1	−1.7	±1.3
-"-	-"-	-"-	m12	−12.5	±1.3	−8.4	±1.1	−1.9	±1.3
-"-	-"-	-"-	m13	−9.2	±1.3	−6.0	±1.0	−1.2	±1.2
-"-	MP57	chd#4	m14*	6.3	±1.2	1.9	±1.1	−1.4	±1.2

Table 5. *Continued.* Oxygen-isotope compositions of fayalite and magnetite in Kaba (CV3.1) chondrite.

Mineral	PTS	Object#	Spot#	$\delta^{18}O$	2σ	$\delta^{17}O$	2σ	$\Delta^{17}O$	2σ
-"-	-"-	-"-	m15*	7.8	±1.2	2.1	±1.1	−2.0	±1.2
-"-	-"-	-"-	m16*	8.5	±1.2	3.3	±1.1	−1.1	±1.2
-"-	-"-	chd#5	m17*	4.0	±1.4	−0.6	±1.1	−2.6	±1.3
-"-	-"-	-"-	m18*	5.4	±1.4	1.0	±1.1	−1.8	±1.3

Chd = chondrule; frg = chondrule fragment; mx = matrix.
*Excluded.

thickness) around an individual forsteritic olivine (Fa_2) show a wide range of fayalite content (Fa_{28-100}) indicating a postcrystallization Fe-Mg exchange with the host olivine and/or with the surrounding matrix minerals (Figs. 3d−f). Additionally, our TEM observations indicate that the porosity and the Mg-rich diffusion laths (Fa_{28}), up to 1.5 μm wide and 5.5 μm long, depend on the crystal orientation of the MgO-rich host olivine.

3. Fayalite–magnetite–hedenbergite veins around type I chondrules (Fig. 4). The veins commonly start at the opaque nodules, composed mainly of magnetite and Fe,Ni-sulfides, in the peripheral portions of the host chondrules, crosscut fine-grained rims around them, and terminate at the boundary with the fine-grained rims around neighboring chondrules. Magnetite nodules typically contain detectable Ca, P, Cr, and Ni, most likely due to the presence of tiny inclusions of Ca-phosphate, Ni-bearing sulfides, and chromite (Fig. 4). The nodules are often surrounded by a compositionally pure magnetite ($FeFe_2O_4$) that occasionally occupies an interstitial region between chondrule phenocrysts (Fig. 4b). The compositionally pure magnetite grains are also commonly observed in the MAC 88107 matrix and around fine-grained chondrule rims crosscut by the magnetite-bearing veins. Chondrule mesostasis is replaced by phyllosilicates and is partially leached out (Figs. 3b and 4b). Chondrule olivines and pyroxenes show little evidence for aqueous alteration; however, inclusions of Fe,Ni-metal in olivine phenocrysts are often surrounded by ferroan olivine haloes (Fig. 4b).

EET 90043 (CO3.1)

EET 90043 is the anomalous, magnetite-rich CO3 chondrite that was originally classified as a CM2 because of the presence of phyllosilicates (Choe et al. 2010). Based on the petrographic, radiochemical neutron activation analysis and spectroscopic study, Tonui et al. (2001, 2002) suggested that the meteorite experienced heating at ~600−700 °C that resulted in partial dehydration and loss of some mobile trace elements (Cd, Tl, Bi, In, and Zn).

Our mineralogical observations indicate the common presence of fayalite–magnetite ± hedenbergite assemblages in EET 90043. Textural occurrences of these assemblages are similar to those in MAC 88107, but hedenbergite is quite rare. These include (1) coarse euhedral and subhedral fayalite grains with small inclusions of magnetite in the matrix (Fig. 5a), (2) fayalite ± magnetite overgrowths on olivine of type I and II chondrules and chondrule fragments (Figs. 5b−f), and (3) fayalite–magnetite veins crosscutting fine-grained rims around chondrules (Figs. 5g−j). In addition, coarse fayalite grains closely associated with magnetite nodules occur inside type I chondrules (Figs. 5e and 5f). Most fayalite grains are nearly pure Fe_2SiO_4 ($Fa_{>96}$; Table S1) and even in direct contact with forsteritic olivines show no evidence for Fe-Mg interdiffusion. However, this is not always the case (e.g., Fig. 5f).

As in MAC 88107, there are two major textural occurrences of magnetite (1) magnetite replacing Fe,Ni-metal ± sulfide nodules in chondrules and matrix, and (2) anhedral-to-subhedral magnetite grains overgrowing metal-sulfide nodules (Figs. 5i,k and S5). Magnetite replacing Fe,Ni-metal nodules contains elevated Cr, Ni, and P (up to 1 wt%), whereas massive magnetite grains and magnetite veins are compositionally pure $FeFe_2O_4$.

Y-81020 (CO3.05)

The Y-81020 (CO3.05) carbonaceous chondrite contains relatively common magnetite, but only rare occurrences of fayalite and hedenbergite (Figs. 6 and S8). Fayalite grains, 3−5 μm in size, overgrow ferromagnesian olivines of type I and II chondrule fragments (Figs. 6a and 6b). Hedenbergite grains are found only in veins crosscutting the Y-81020 matrix (Figs. 6c and 6d).

There are two major textural occurrence of magnetite in Y-81020 (1) magnetite with small inclusions of other phases replacing Fe,Ni-metal ± sulfide nodules, and (2) massive subhedral magnetite grains, often overgrowing magnetite nodules, in chondrules and matrix (Figs. 6e,f and S6). In contrast to MAC 88107 and EET 90043, many Fe,Ni-metal nodules in Y-81020 chondrules are incompletely replaced by magnetite

Table 6. Oxygen-isotope compositions of fayalite and magnetite in unequilibrated ordinary chondrites.

Chondrite	PTS	Mineral	Object#	spot#	δ¹⁸O	2σ	δ¹⁷O	2σ	Δ¹⁷O	2σ
Semarkona	1805-5	mgt	chd#1	m1	3.1	±0.5	5.8	±0.5	4.2	±0.5
-"-	-"-	-"-	-"-	m2	0.7	±0.6	5.3	±0.4	4.9	±0.5
-"-	-"-	-"-	-"-	m3	1.9	±0.5	5.8	±0.5	4.8	±0.5
-"-	-"-	-"-	-"-	m4	2.7	±0.5	5.5	±0.4	4.1	±0.5
-"-	-"-	-"-	-"-	m5*	0.0	±0.5	4.4	±0.5	4.4	±0.6
-"-	-"-	-"-	-"-	m6	2.5	±0.6	5.4	±0.5	4.1	±0.6
-"-	-"-	-"-	-"-	m7*	0.2	±0.8	4.2	±0.6	4.1	±0.8
-"-	-"-	-"-	-"-	m8	3.0	±0.5	6.2	±0.4	4.7	±0.5
-"-	-"-	-"-	nod#1	m9	3.2	±0.5	5.8	±0.5	4.1	±0.6
-"-	-"-	-"-	-"-	m10	1.4	±0.5	5.1	±0.4	4.4	±0.5
-"-	-"-	-"-	-"-	m11	0.8	±0.4	4.8	±0.5	4.3	±0.6
-"-	-"-	-"-	nod#2	m12	−0.3	±0.5	2.6	±0.5	2.8	±0.5
-"-	-"-	-"-	-"-	m13*	−3.5	±1.1	1.9	±0.7	3.7	±0.9
-"-	-"-	-"-	-"-	m14*	−0.5	±0.5	3.3	±0.4	3.6	±0.5
-"-	-"-	-"-	-"-	m15*	0.4	±0.5	4.0	±0.4	3.8	±0.5
-"-	-"-	-"-	nod#3	m16	2.5	±0.6	4.8	±0.4	3.5	±0.5
-"-	-"-	-"-	-"-	m17*	−2.8	0.97	2.8	0.61	4.3	±0.8
-"-	-"-	-"-	-"-	m18	2.0	±0.8	4.7	±0.5	3.6	±0.7
-"-	-"-	-"-	-"-	m19*	1.5	±0.5	4.9	±0.5	4.1	±0.5
-"-	4218-4	mgt	nod#1	m1*	1.4	±0.6	5.4	±0.4	4.6	±0.5
-"-	-"-	-"-	-"-	m2*	2.9	±0.4	5.7	±0.4	4.2	±0.5
-"-	-"-	-"-	-"-	m3	2.4	±0.4	5.8	±0.4	4.5	±0.4
-"-	-"-	-"-	-"-	m4	3.5	±0.3	6.4	±0.4	4.6	±0.4
-"-	-"-	-"-	-"-	m5	1.6	±0.5	5.2	±0.4	4.3	±0.5
-"-	-"-	-"-	-"-	m6	2.8	±0.6	6	±0.3	4.6	±0.5
-"-	-"-	-"-	-"-	m7	3.1	±0.5	5.9	±0.4	4.2	±0.5
-"-	-"-	-"-	-"-	m8	4.1	±0.4	6.4	±0.4	4.3	±0.5
-"-	-"-	-"-	-"-	m9*	0.2	±0.8	4.4	±0.5	4.3	±0.6
-"-	-"-	-"-	-"-	m11	2.4	±0.5	4.4	±0.3	3.1	±0.4
-"-	-"-	-"-	-"-	m12	1.3	±0.5	4.4	±0.5	3.7	±0.5
-"-	-"-	-"-	nod#2	m13	1.6	±0.4	5.4	±0.4	4.6	±0.5
-"-	-"-	-"-	-"-	m14	2.8	±0.5	5.8	±0.5	4.4	±0.6
-"-	-"-	-"-	-"-	m15	2.3	±0.6	6.1	±0.4	4.9	±0.5
-"-	-"-	-"-	-"-	m16*	−0.9	±0.6	4.3	±0.4	4.8	±0.5
-"-	-"-	-"-	-"-	m17	3.1	±0.6	7	±0.4	5.4	±0.5
-"-	-"-	-"-	nod#3	wus18	−1.3	±0.5	3.6	±0.5	4.3	±0.6
-"-	-"-	-"-	-"-	wus19	−1.2	±0.6	4.3	±0.5	5	±0.6
-"-	-"-	-"-	-"-	wus20*	0.3	±0.8	4.5	±0.5	4.3	±0.6
MET 00452	16	mgt	chd#1	m1	6.2	±0.4	7.6	±0.4	4.4	±0.5
-"-	-"-	-"-	-"-	m2*	1.8	±0.6	5.6	±0.4	4.7	±0.5
-"-	-"-	-"-	-"-	m3*	0.9	±0.9	5.5	±0.5	5	±0.7
-"-	-"-	-"-	nod#2	m4*	0.4	±0.7	5.4	±0.5	5.2	±0.6
-"-	-"-	-"-	-"-	m5*	0.2	±0.7	4.8	±0.6	4.7	±0.7
-"-	-"-	-"-	-"-	m6	2.3	±0.5	6.2	±0.5	4.9	±0.6
-"-	-"-	-"-	nod#3	m7	3.3	±0.4	5.8	±0.4	4.1	±0.4
-"-	-"-	-"-	-"-	m8*	2.2	±0.5	6.2	±0.6	5.1	±0.6
-"-	-"-	-"-	nod#4	m9	4.00	±0.5	6.3	±0.5	4.2	±0.5
-"-	-"-	-"-	nod#5	m10	4.6	±0.4	6.5	±0.5	4.2	±0.5
-"-	-"-	-"-	-"-	m11*	3.2	±0.5	5.6	±0.5	4	±0.6
-"-	-"-	-"-	-"-	m12	4.00	±0.4	6.7	±0.4	4.7	±0.5
MET 00452	18	mgt	chd#1	m1	3.3	±0.5	5.6	±0.6	3.9	±0.6
-"-	-"-	-"-	-"-	m2	3.0	±0.4	5.9	±0.4	4.4	±0.5
-"-	-"-	-"-	-"-	m3	3.2	±0.8	6.3	±0.5	4.7	±0.7
-"-	-"-	-"-	-"-	m4*	−3.6	±1.0	3.9	±0.6	5.8	±0.8

Table 6. *Continued*. Oxygen-isotope compositions of fayalite and magnetite in unequilibrated ordinary chondrites.

Chondrite	PTS	Mineral	Object#	spot#	δ¹⁸O	2σ	δ¹⁷O	2σ	Δ¹⁷O	2σ
-"-	-"-	-"-	-"-	m5*	2.1	±0.5	3.9	±0.6	2.8	±0.6
-"-	-"-	-"-	-"-	m6*	3.6	±0.5	4.6	±0.4	2.7	±0.5
-"-	-"-	-"-	nod#2	m7*	1.3	±0.8	5.1	±0.5	4.4	±0.6
-"-	-"-	-"-	-"-	m8	4.0	±0.3	6.9	±0.5	4.8	±0.5
MET 00452	18	mgt	nod#2	m9	3.7	±0.6	6	±0.5	4.1	±0.6
-"-	-"-	-"-	nod#3	m10	5.2	±0.4	7.2	±0.5	4.5	±0.5
-"-	-"-	-"-	-"-	m11	3.6	±0.5	6.1	±0.4	4.2	±0.4
-"-	-"-	-"-	-"-	m12	4.4	±0.6	6.8	±0.6	4.6	±0.7
-"-	-"-	-"-	-"-	m13*	2.9	±0.7	5.7	±0.6	4.2	±0.7
-"-	-"-	-"-	-"-	m14*	2.8	±0.7	5.3	±0.5	3.8	±0.7
-"-	-"-	-"-	-"-	m15	4.6	±0.6	6.7	±0.5	4.4	±0.6
-"-	-"-	-"-	-"-	m16	3.8	±0.5	6.3	±0.4	4.3	±0.5
-"-	-"-	-"-	-"-	m17*	−2.5	±1.1	3.3	±0.7	4.6	±0.9
-"-	-"-	-"-	nod#4	m18	6.1	±0.3	6.6	±0.5	3.4	±0.5
-"-	-"-	-"-	-"-	m19*	−0.1	±1.0	4.0	±0.8	4.0	±0.9
-"-	-"-	-"-	-"-	m20	6.9	±0.6	6.9	±0.6	3.3	±0.6
-"-	-"-	-"-	-"-	m21*	4.6	±0.6	4.6	±0.5	2.2	±0.6
Ngawi	2843-2	mgt	reg#1	m1	1.4	±1.2	6.3	±0.9	5.6	±1.1
-"-	-"-	-"-	-"-	m2*	−2.7	±1.4	3.4	±0.9	4.8	±1.2
-"-	-"-	-"-	-"-	m3*	−1.9	±1.2	4.8	±0.9	5.8	±1.1
-"-	-"-	-"-	reg#2	m4*	−1.7	±1.2	3.7	±0.9	4.6	±1.1
-"-	-"-	-"-	-"-	m7*	−0.6	±1.2	4.1	±0.9	4.4	±1.1
-"-	-"-	-"-	-"-	m8	1.1	±1.3	5.3	±0.9	4.7	±1.1
-"-	-"-	-"-	-"-	m9	−0.6	±1.2	5.0	±0.9	5.3	±1.1
-"-	-"-	-"-	reg#3	m10	7.4	±1.2	8.8	±0.9	5.0	±1.1
-"-	-"-	-"-	-"-	m11*	5.8	±1.4	8.2	±1.0	5.2	±1.2
-"-	-"-	-"-	-"-	m12	7.0	±1.3	9.5	±0.9	5.9	±1.1
-"-	-"-	-"-	reg#4	m13	1.8	±1.2	6.1	±0.9	5.2	±1.1
-"-	-"-	-"-	-"-	m14	1.8	±1.2	6.0	±0.9	5.1	±1.1
-"-	-"-	-"-	reg#5	m15*	0.0	±1.3	5.0	±0.9	5.0	±1.1
-"-	-"-	mgt	reg#3	m1	8.4	±3.1	8.9	±2.5	4.5	±3.0
-"-	-"-	-"-	-"-	m2*	−0.3	±3.1	3.8	±2.5	4.0	±3.0
-"-	-"-	-"-	-"-	m3*	1.5	±3.1	6.1	±2.4	5.4	±2.9
Ngawi	2843-2	mgt	reg#3	m4	6.0	±3.6	6.4	±2.7	3.3	±3.3
-"-	-"-	-"-	-"-	m5	6.5	±3.2	7.6	±2.6	4.2	±3.1
-"-	-"-	-"-	-"-	m6	8.2	±3.1	8.3	±2.5	4.1	±3.0
-"-	-"-	-"-	-"-	m7	9.1	±3.1	9.7	±2.5	4.9	±3.0
-"-	-"-	-"-	-"-	m8	7.4	±3.2	7.7	±2.4	3.8	±2.9
-"-	-"-	-"-	reg#1	m9	−3.0	±3.1	2.3	±2.4	3.8	±2.9
-"-	-"-	-"-	-"-	m10	−1.2	±3.2	4.3	±2.6	4.9	±3.0
-"-	-"-	-"-	-"-	m11	0.3	±3.1	3.4	±2.5	3.2	±3.0
-"-	-"-	-"-	-"-	m12	0.1	±3.2	4.5	±2.4	4.5	±2.9
-"-	-"-	-"-	-"-	m13	0.5	±3.1	6.0	±2.5	5.8	±3.0
-"-	-"-	-"-	-"-	m14	−0.3	±3.1	4.0	±2.4	4.1	±2.9
-"-	-"-	-"-	-"-	m15	−0.1	±3.2	5.2	±2.5	5.2	±3.0
-"-	-"-	-"-	reg#4	m16	0.9	±3.1	3.9	±2.5	3.5	±3.0
-"-	-"-	-"-	-"-	m17	1.2	±3.1	4.2	±2.5	3.6	±3.0
-"-	-"-	-"-	reg#3	m18	−2.1	±3.1	3.8	±2.6	4.9	±3.1
-"-	-"-	-"-	-"-	m19	3.0	±3.2	7.3	±2.5	5.7	±3.0
-"-	-"-	-"-	-"-	m20	2.7	±3.2	5.6	±2.4	4.2	±2.9
-"-	-"-	-"-	-"-	m21	−2.7	±3.2	3.4	±2.6	4.8	±3.0
-"-	-"-	-"-	-"-	m22	−0.3	±3.1	4.0	±2.5	4.1	±3.0
-"-	-"-	-"-	-"-	m23	−1.8	±3.2	4.0	±2.5	4.9	±3.0
Ngawi	44	fa	reg#1	f1	8.3	±1.5	9.0	±1.9	4.7	±2.1

Table 6. *Continued.* Oxygen-isotope compositions of fayalite and magnetite in unequilibrated ordinary chondrites.

Chondrite	PTS	Mineral	Object#	spot#	$\delta^{18}O$	2σ	$\delta^{17}O$	2σ	$\Delta^{17}O$	2σ
-"-	-"-	-"-	-"-	f2	6.5	±1.5	7.3	±1.9	3.9	±2.0
-"-	-"-	-"-	-"-	f3	7.6	±1.5	9.1	±1.7	5.2	±1.9
-"-	-"-	-"-	-"-	f4	7.3	±1.6	8.4	±2.1	4.7	±2.2
-"-	-"-	-"-	-"-	f5	6.1	±1.5	8.0	±1.9	4.8	±2.1
-"-	-"-	-"-	reg#2	f6	6.2	±1.6	8.2	±1.7	5.0	±1.9
-"-	-"-	-"-	-"-	f7	8.4	±1.6	9.1	±1.9	4.7	±2.0
-"-	-"-	-"-	-"-	f8	4.7	±1.6	6.5	±1.9	4.7	±2.0
-"-	-"-	-"-	reg#3	f1	10.4	±0.9	8.9	±1.5	3.5	±1.9
Ngawi	44	fa	reg#3	f2	10.5	±0.8	8.4	±1.7	2.9	±2.0
-"-	-"-	-"-	-"-	f3	8.3	±0.8	8.1	±1.5	3.8	±1.9
-"-	-"-	-"-	reg#4	f4	8.5	±0.8	7.5	±1.6	3.1	±2.0
-"-	-"-	-"-	-"-	f5	7.9	±0.8	8.7	±1.5	4.6	±1.9
-"-	-"-	-"-	-"-	f6	8.4	±0.8	8.6	±1.6	4.2	±2.0
-"-	-"-	-"-	-"-	f7	9.3	±0.9	9.2	±1.5	4.3	±1.9
-"-	-"-	-"-	-"-	f9	8.4	±0.8	7.2	±1.9	2.9	±2.2
-"-	-"-	-"-	-"-	f10	8.3	±0.8	8.6	±1.6	4.3	±2.0
-"-	-"-	-"-	reg#6	f13	8.6	±0.9	8.9	±1.7	4.4	±2.1
-"-	-"-	-"-	reg#5	f15	7.6	±1.0	7.1	±1.7	3.2	±2.1
Vicência	UH	fa	reg#105	f1	10.7	±0.4	9.7	±0.5	3.9	±0.5
-"-	-"-	-"-	reg#69	f2	9.4	±0.5	9.4	±0.6	4.3	±0.6
-"-	-"-	-"-	reg#31	f3	9.8	±0.5	9.1	±0.4	3.7	±0.5
-"-	-"-	-"-	reg#31	f4	10.2	±0.4	9.6	±0.4	3.9	±0.5
-"-	-"-	-"-	reg#66	f5*	12.5	±0.4	8.9	±0.6	2.1	±0.7
-"-	-"-	-"-	reg#4a	f6	6.3	±0.4	8.0	±0.4	4.4	±0.4
-"-	-"-	-"-	reg#4a	f7*	7.2	±0.5	7.3	±0.4	3.3	±0.4
MET 96503	7	fa	1-1	f1	4.0	±1.8	6.3	±3.0	4.3	±3.2
-"-	-"-	-"-	1-1	f2	3.3	±1.3	6.8	±2.5	5.1	±2.6
-"-	17	-"-	5-1	f3	5.2	±1.5	6.7	±2.8	3.9	±2.9
-"-	14	-"-	36-76	f4	9.6	±1.0	9.1	±2.0	4.1	±2.0
-"-	-"-	-"-	9-27	f5	7.5	±0.9	7.9	±2.2	3.9	±2.2
-"-	-"-	-"-	8-20	f6	7.0	±1.1	9.3	±2.3	5.7	±2.3
-"-	-"-	-"-	21-6	f7	6.3	±2.1	8.7	±2.9	5.4	±3.1
-"-	-"-	-"-	31-60	f8	8.9	±1.1	8.8	±2.3	4.1	±2.4
-"-	-"-	-"-	31-60	f9	10.4	±1.0	8.6	±2.0	3.2	±2.1
-"-	-"-	-"-	2-4	f10	8.0	±1.3	6.7	±2.3	2.6	±2.4
-"-	-"-	-"-	29-56	f11	8.7	±1.0	8.9	±2.9	4.4	±2.9
-"-	-"-	-"-	35-72	f12	8.3	±1.1	7.7	±2.3	3.4	±2.4
MET 96503	14	fa	25-39	f13	7.3	±0.9	8.0	±2.2	4.3	±2.2
-"-	-"-	-"-	25-41	f14	8.4	±1.0	9.1	±1.9	4.8	±2.0
-"-	-"-	-"-	2b-7	f15	8.5	±1.0	8.3	±1.9	3.8	±2.0
EET 90161	15	fa	23-20p	f1	7.5	±1.4	8.2	±2.3	4.3	±2.4
-"-	-"-	-"-	7-47p	f2	8.7	±1.4	9.6	±2.4	5.0	±2.5
-"-	-"-	-"-	5-36p	f3	9.6	±1.4	9.5	±2.4	4.5	±2.5
-"-	-"-	-"-	27-40p	f4	10.8	±1.4	9.6	±2.7	4.0	±2.8
-"-	-"-	-"-	23-23c	f5	8.6	±1.4	10.3	±2.5	5.9	±2.6
-"-	-"-	-"-	23-20c	f6	10.9	±1.4	10.9	±2.5	5.2	±2.6
-"-	-"-	-"-	20-8c	f7	9.3	±1.3	9.7	±2.4	4.8	±2.5
-"-	-"-	-"-	20-8c	f8*	10.1	±1.3	8.3	±2.4	3.0	±2.5
-"-	-"-	-"-	7-48c	f9	9.0	±1.4	9.9	±2.4	5.2	±2.5
-"-	-"-	-"-	28-44c	f10	9.1	±1.4	11.0	±2.4	6.3	±2.5
-"-	-"-	-"-	28-44c	f11	8.7	±1.4	9.3	±2.6	4.8	±2.7
-"-	-"-	-"-	29-47c	f12	9.0	±1.4	9.6	±2.4	4.9	±2.5
-"-	-"-	-"-	4-29c	f13	9.9	±1.3	8.7	±2.4	3.5	±2.5
-"-	-"-	-"-	4-31c	f14	8.5	±1.3	9.5	±2.4	5.1	±2.5
-"-	-"-	-"-	3-18c	f15	9.1	±1.3	9.7	±2.3	5.0	±2.4

*Excluded from diagrams.
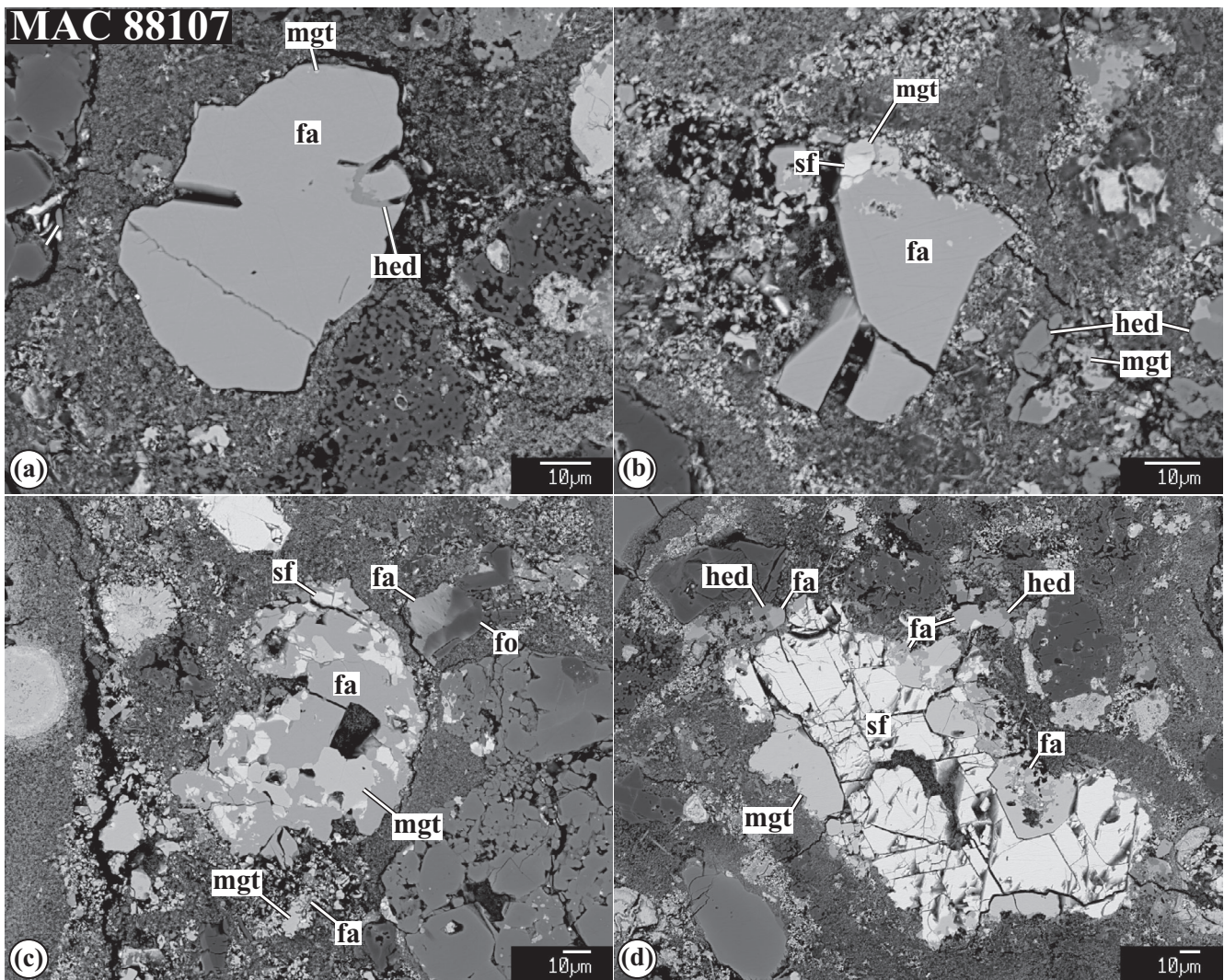
Fig. 2. Backscattered electron images of the fayalite ± hedenbergite–magnetite assemblages in matrix of MAC 88107 (CO3.1-like). a, b) Isolated coarse fayalite grains, containing small inclusions of magnetite, ±sulfide and ±hedenbergite. c, d) Coarse-grained magnetite–fayalite–sulfide particles. Magnetite appears to be corroded by fayalite; fayalite and hedenbergite are intergrown. fa = fayalite; fo = type I chondrule forsteritic olivine; hed = hedenbergite; mgt = magnetite; sf = Fe,Ni-sulfide.

(Figs. 6e and 6f), suggesting a smaller degree of aqueous alteration.

Kaba (CV3.1)

Fayalite–magnetite ± hedenbergite assemblages occur in all Kaba components—refractory inclusions, chondrules, and matrix, and have been previously characterized in detail (Hua and Buseck 1995; Krot et al. 1998; this study). In Fig. 7, we illustrate only typical occurrences of fayalite and magnetite measured for oxygen isotopic compositions (additional images are shown in Figs. S9–S20). These include (1) coarse fayalite grains in the matrix (Fig. 7a), (2) fayalite ± hedenbergite overgrowths on chondrule fragments (Figs. 7b and 7c), (3) fayalite–magnetite–

sulfide veins crosscutting fine-grained rims around chondrule (Figs. 7d and 7e), and (4) coarse fayalite grains inside type I chondrules (Figs. 7f and 7g). All fayalite grains measured for oxygen isotopes are nearly endmember fayalite.

There are two major textural occurrences of magnetite in Kaba (1) magnetite–sulfide nodules replacing Fe,Ni-metal in type I chondrules, and (2) massive subhedral magnetite grains, often with elongated inclusions of Fe,Ni-sulfides, overgrowing magnetite–sulfide nodules (Figs. 7h and 7i). Nodular magnetite contains high chromium contents, whereas massive magnetite is compositionally pure $Fe^{2+}Fe^{3+}_2O_4$.

Plagioclase and glassy mesostasis in Kaba chondrules are replaced by phyllosilicates (see fig. 2 in
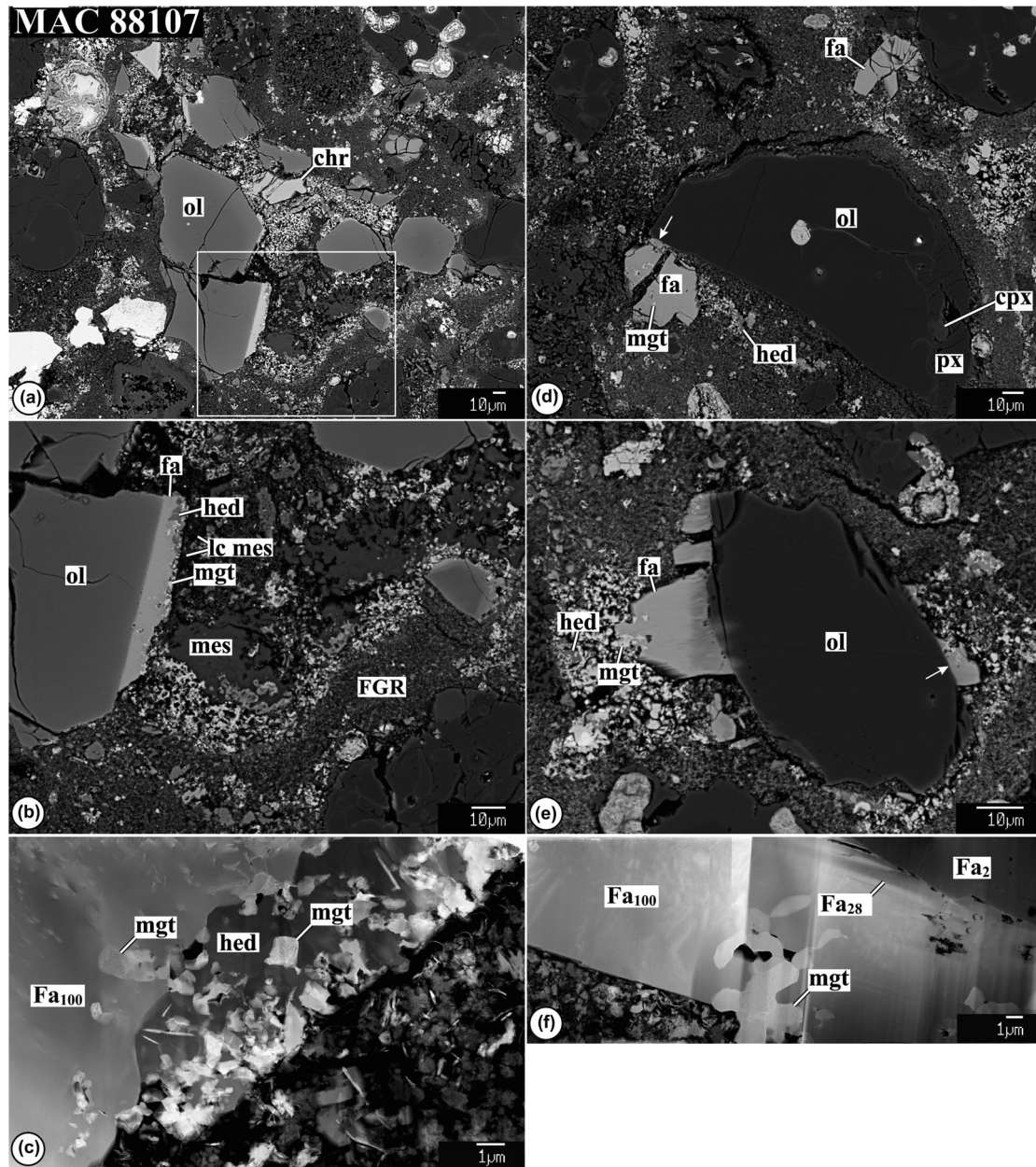
Fig. 3. Backscattered electron (a, b, d, e) and dark-field STEM images (c, f) of the fayalite–hedenbergite–magnetite assemblages overgrowing type I and II chondrule olivines in the MAC 88107 (CO3.1-like) chondrite. a–c) Type II chondrule with mesostasis partly leached out by an aqueous fluid. Olivine phenocrysts are overgrown by fayalite with tiny inclusions of magnetite and hedenbergite. Region outlined in (a) is shown in (b). Detailed TEM micrograph of the fayalite–hedenbergite–magnetite assemblage overgrowing the chondrule olivine is shown in (c). Both fayalite (Fa_{100}) and hedenbergite contain anhedral magnetite inclusions. These inclusions are rare in the fayalite rim, but abundant in the exterior rim made of hedenbergite. d, e) Fragments of type I chondrules overgrown by fayalite with inclusions of magnetite and ±hedenbergite. Some fayalite grains experienced Fe-Mg interexchange with the host forsteritic olivine, whereas others (indicated by arrows in [c] and [d]) avoided it. f) Detailed TEM micrograph of a fayalite rim (Fa_{100}) in contact with forsteritic olivine (Fa_2) and showing evidence for Fe-Mg interdiffusion (Fa_{28}). The fayalite rim contains euhedral, polycrystalline magnetite inclusions. chr = chromite; cpx = high-Ca pyroxene; fa = fayalite; FGR = fine-grained rim; hed = hedenbergite; lc mes = leached mesostasis; mes = mesostasis; mgt = magnetite; ol = type I and II chondrule ferromagnesian olivine; px = type I chondrule magnesian low-Ca pyroxene; sf = Fe,Ni-sulfide.
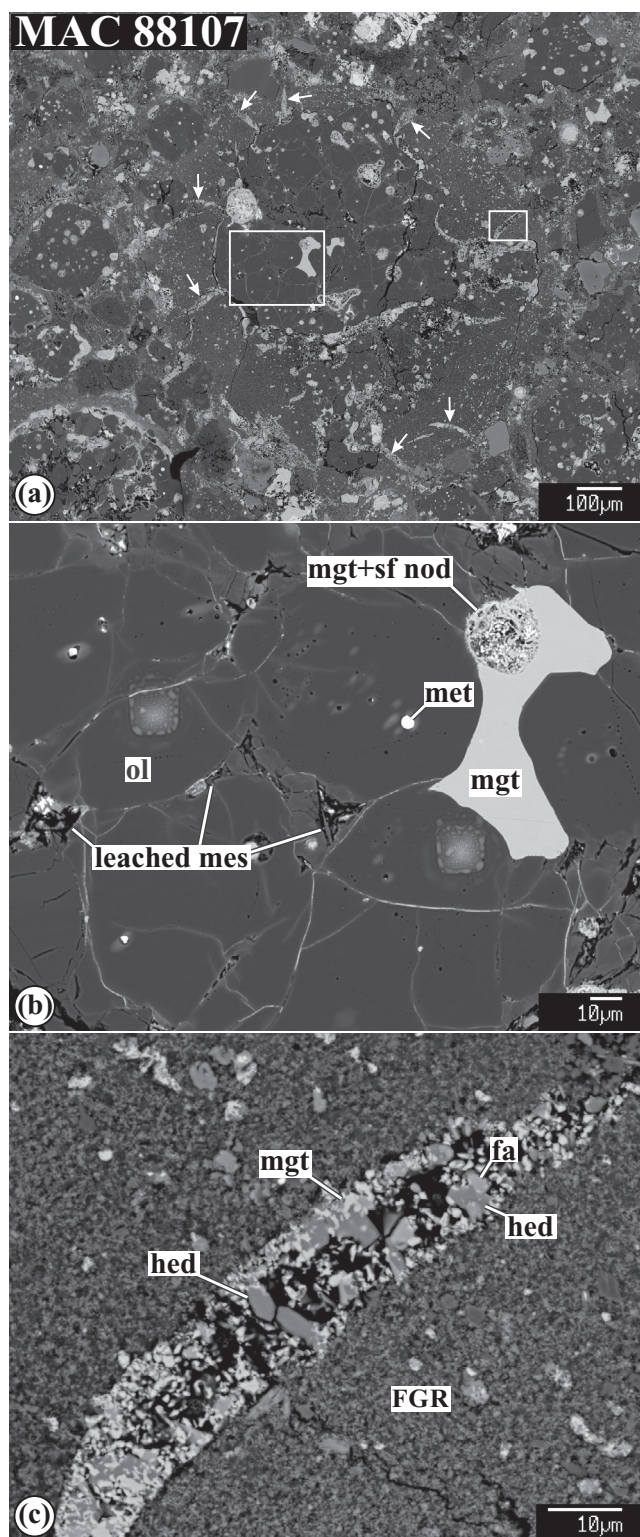
Fig. 4. Backscattered electron images of a type I chondrule in the MAC 88107 (CO3.1-like) chondrite. Opaque nodules composed predominantly of Fe,Ni-metal and sulfides in the chondrule appear to be porous and consist of magnetite and sulfides; they are overgrown by massive magnetite. Chondrule mesostasis is partly leached out. Fine-grained rim is crosscut by multiple fayalite–hedenbergite–magnetite veins (indicated by arrows in [a]). Regions outlined in (a) are shown in detail in (b) and (c). fa = fayalite; FGR = fine-grained rim; hed = hedenbergite; mes = mesostasis; met = Fe,Ni-metal; nod = nodule; mgt = magnetite; ol = type I chondrule forsteritic olivine; sf = Fe,Ni-sulfides.

Unequilibrated Ordinary Chondrites

Semarkona (LL3.00)

The mineralogy, chemical compositions, and textural occurrences of magnetite-bearing assemblages in Semarkona have been previously characterized in detail by Hutchison et al. (1987), Alexander et al. (1989), Krot et al. (1997), and Choi et al. (1998). In two Semarkona sections studied here, 1805-5 and 4128-4, magnetite associated with Ni-rich metal, troilite, and Fe,Ni-carbides occurs in chondrules and matrix where it typically replaces and overgrows Fe,Ni-metal ± sulfide nodules (Figs. S21−S24). In the thin section 4128-4, nearly completely surrounded by a fusion crust (Fig. S23), magnetite in several nodules is replaced to various degrees by wüstite (Figs. 8, S24a,e,f).

Ferroan olivine/fayalite is not uncommon in the Semarkona matrix and matrix-like rims around type I chondrules and opaque nodules, but it is very fine-grained (Fig. 9). It occurs as isolated submicron-sized subhedral-to-euhedral grains and as rims around ferromagnesian olivines of chondrule fragments (Figs. 9a−f). Some ferroan olivines show inverse compositional zoning (Figs. 9i and 9j).

EET 90161 (L3.05), MET 96523 (L3.1), and MET 00452 (L3.05)

The mineralogy and textural occurrences of magnetite ± Fe,Ni-metal ± Fe,Ni-carbide ± Fe,Ni-sulfide assemblages in EET 90161, EET 96523, and MET 00452 are similar to those in Semarkona, and have been described in detail by Krot et al. (1997). BSE images of magnetite grains analyzed in MET 00452 are illustrated in Figs. S25−S28.

There are several textural occurrences of fayalite in EET 90161, MET 96523, and MET 00452. (1) Fayalite grains that overgrow ferromagnesian olivines, occasionally associated with low-Ca pyroxenes and probably representing fragments of type I and II chondrules (Figs. 10a and 10b). (2) Abundant anhedral

Nagashima et al. 2017) and unidentified Fe-rich fine-grained secondary minerals to various degrees (Figs. 7j−l).
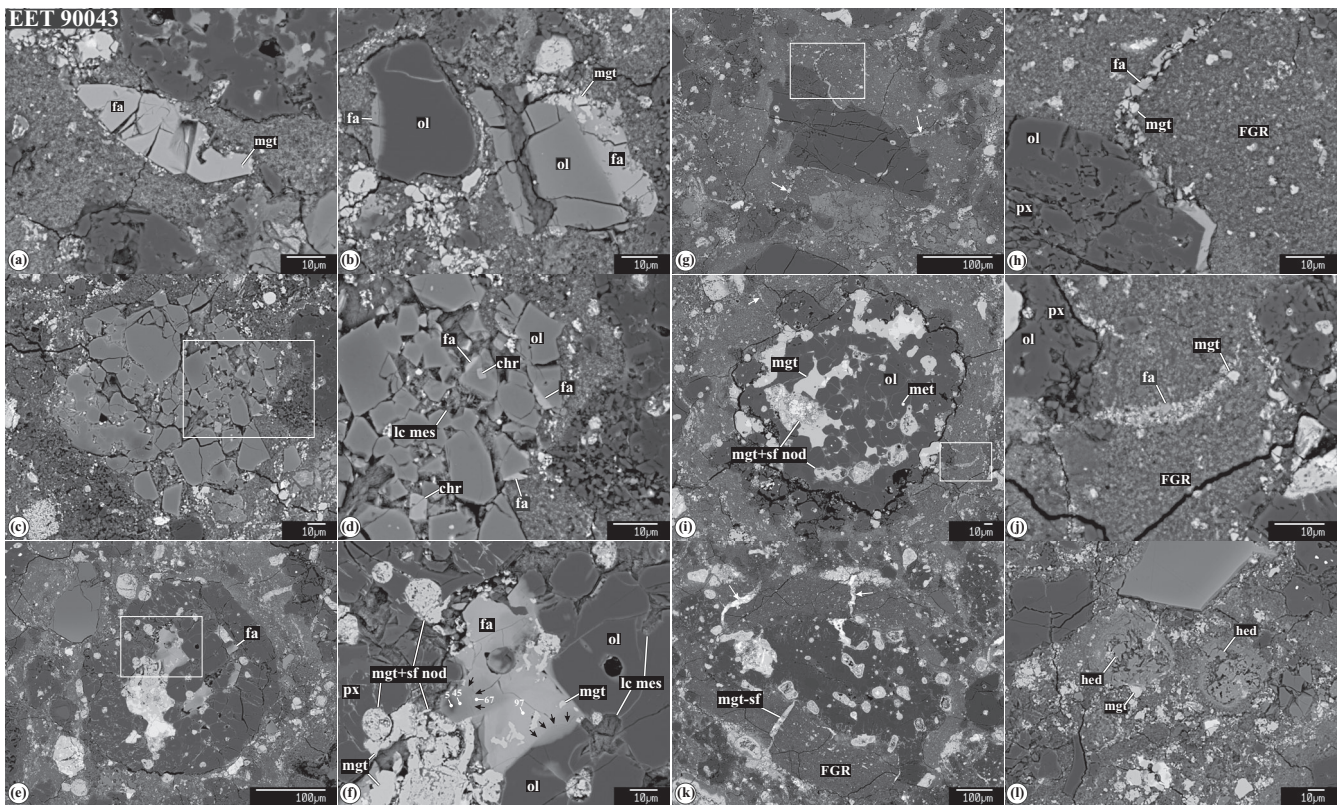
Fig. 5. Backscattered electron images of fayalite–magnetite ± hedenbergite assemblages in the EET 90043 (CO3) chondrite. a) Subhedral fayalite grain in the matrix. b) Fayalite ± magnetite overgrowths of type I and II chondrule olivine fragments. c, d) Fayalite overgrowths of olivine phenocrysts in a type II chondrule with mesostasis partly leached out. e, f) Type I chondrule with fayalite grains overgrowing forsteritic olivine phenocrysts. Portions of olivine phenocrysts in contact with fayalite are pseudomorphically replaced by ferroan olivine (edges of the grains are indicated by black arrows; numbers near white dots correspond to fayalite contents). Chondrule mesostasis is partly leached out. Metal nodules are replaced by magnetite. g–k) Type I chondrules with fine-grained rims crosscut by magnetite ± fayalite ± sulfide veins (indicated by white arrows). l) Hedenbergite nodules in matrix. Regions outlined in (c), (e), (g), and (i) are shown in detail in (d), (f), (h), and (j), respectively. chr = chromite; fa = fayalite; FGR = fine-grained rim; lc mes = leached mesostasis; met = Fe,Ni-metal; mgt = magnetite; nod = nodule; ol = ferromagnesian type I and II chondrule olivine; sf = Fe,Ni-sulfides.

and subhedral fayalite grains occurring in fine-grained rims around type I chondrules typically containing heavily altered opaque nodules in the peripheral portions (Figs. 10c–f). The subhedral fayalite grains are commonly observed in the outermost portions of the rims where they appear to grow into the host meteorite matrices. Chondrule phenocrysts and even glassy mesostasis show little evidence for alteration. (3) FeO-rich olivine ($Fa_{35–95}$) replacing amorphous material+phyllosilicate objects in chondrite matrices (Figs. 10g–m). The FeO-rich olivine rims vary in size from 350 nm up to 5 µm. Similar FeO-rich olivine overgrowths were recently described in Dobrică and Brearley (2021). However, the amorphous silicates associated with fayalite are enriched in CaO (15 wt% CaO) compared with those described in Semarkona (<0.9 wt% CaO, Dobrică and Brearley 2020). (4) Rare

isolated euhedral fayalite grains in matrices (Fig. 10n). Ferroan olivine grains show a range of fayalite content ($Fa_{84–98}$; Table S4); most grains are nearly pure fayalite ($Fa_{>95}$). The most magnesian compositions are found in fayalite overgrowing ferromagnesian olivines.

Ngawi (LL3.0–3.6 Breccia) and Vicência (LL3.2)

The mineralogy and textural occurrences of magnetite in Ngawi and Vicência are similar to those in Semarkona and have been previously described in detail by Krot et al. (1997), Choi et al. (1998), and Keil et al. (2015). Magnetite replaces and overgrows Fe,Ni-metal-sulfide ± Fe,Ni-carbide nodules in chondrules and matrices of these meteorites (Fig. S31). Fayalite occurs preferentially in chondrite matrices, where it forms coarse isolated grains and aggregates of grains; it also overgrows ferromagnesian olivines, most
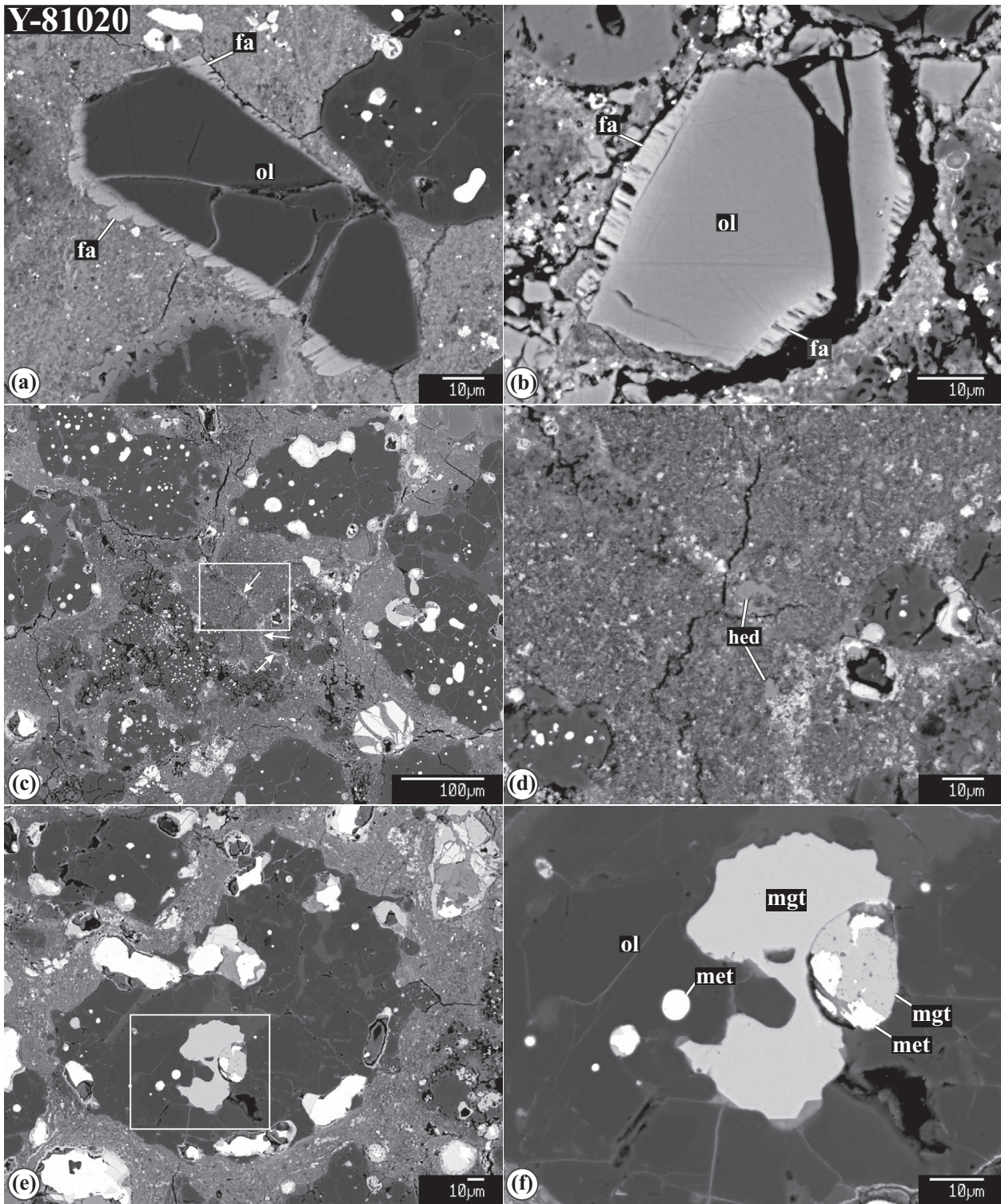
Fig. 6. Backscattered electron images of secondary fayalite, magnetite, and hedenbergite in Y-81020 (CO3.05). a, b) Fayalite overgrowths on type I and II chondrule fragments. c, d) Hedenbergite-bearing vein crosscutting fine-grained matrix. e, f) Type I chondrule with Fe,Ni-metal nodules oxidized to magnetite to various degrees. One of the nodules is overgrown by massive magnetite. Regions outlined in (c) and (e) are shown in detail in (d) and (f), respectively. fa = fayalite; met = Fe,Ni-metal; mgt = magnetite; ol = olivine.
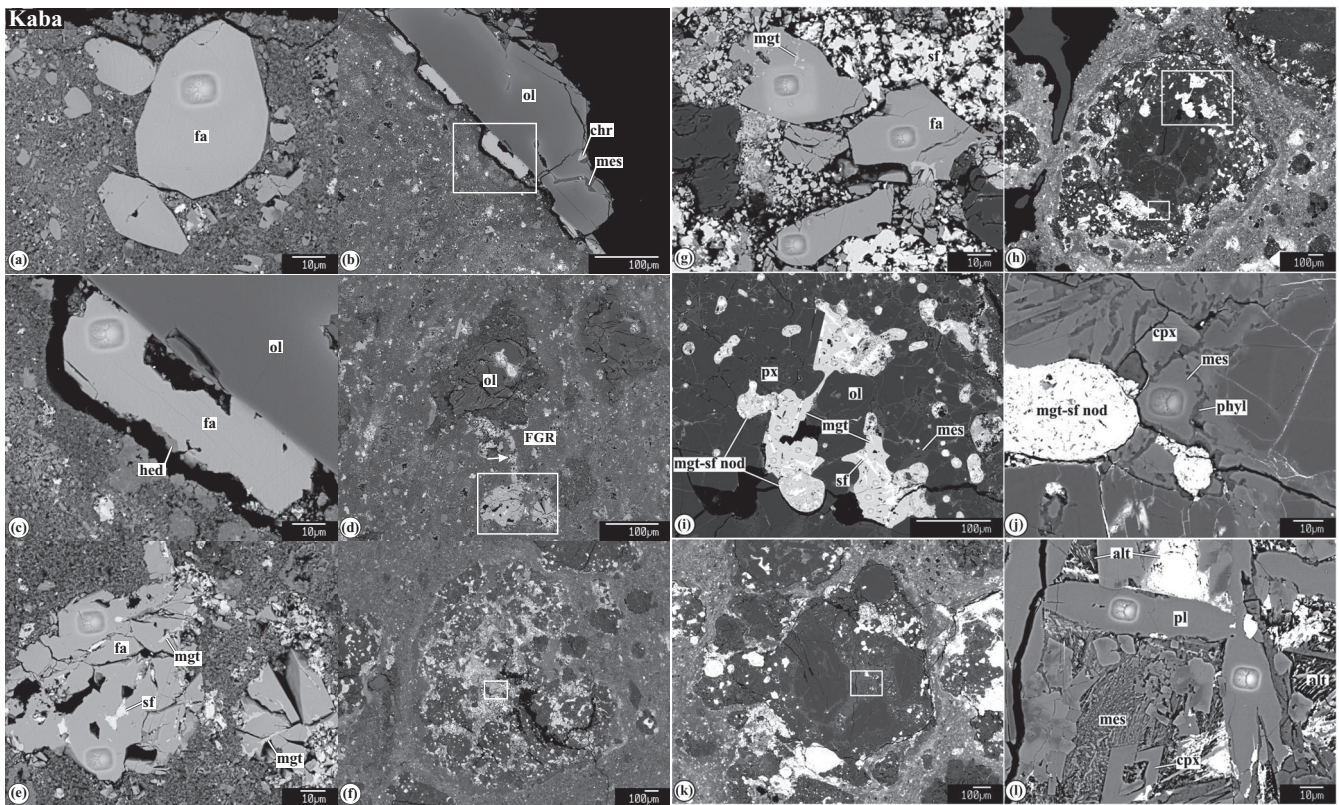
Fig. 7. Backscattered electron images of secondary fayalite, magnetite, hedenbergite, and altered chondrule mesostasis in Kaba ($CV_{oxB}3.1$) measured for oxygen isotopes; SIMS spots are clearly visible. a) Subhedral-to-euhedral fayalite grains in the matrix. b, c) Fayalite ± hedenbergite overgrowths on a type II chondrule fragment. c, d) Type I chondrule surrounded by a fine-grained rim crosscut by a fayalite–magnetite–sulfide vein (indicated by arrow in [d]). The vein is connected to a coarse-grained fayalite with inclusions of magnetite and sulfides. f, g) Type I chondrule with Fe,Ni-metal nodules extensively replaced by magnetite, sulfides, and fayalite. h−j) Type I chondrule with Fe,Ni-metal nodules replaced by magnetite and Fe,Ni-sulfides. The nodules are overgrown by massive magnetite containing elongated inclusions of Fe,Ni-sulfides. Chondrule mesostasis is corroded by phyllosilicates. k, l) Type I chondrule with fine-grained mesostasis and lath-shaped plagioclase replaced by secondary alteration minerals. Regions outlined in (b), (d), (f), (h), and (k) are shown in detail in (c), (e), (g), (i, j), and (l), respectively. alt = secondary alteration minerals; fa = fayalite; hed = hedenbergite; mes = mesostasis; mgt = magnetite; ol = olivine; phyl = phyllosilicates; pl = plagioclase; px = low-Ca pyroxene; sf = Fe,Ni-sulfide.

likely chondrule fragments (Figs. 11 and S32). Most ferroan olivines in Ngawi and some in Vicência show inverse compositional zoning (Fa_{83-64}; Table S4; Fig. 11). Compositionally nearly pure fayalite grains (Fa_{94-98}) are found almost exclusively in Vicência (Table S4).

Oxygen Isotopic Compositions

MAC 88107 (CO3.1-Like)

Because fayalite and magnetite in veins are too fine-grained, only the coarse fayalite grains in the matrix and compositionally pure magnetite grains in chondrules and matrix were analyzed (Figs. 4 and S1−3 in supporting information). We also measured oxygen-isotope compositions of ferromagnesian olivines in chondrules

and chondrule fragments (1) overgrown by fayalite ± magnetite ± hedenbergite, (2) containing coarse magnetite grains, and (3) having fine-grained rims crosscut by the fayalite–magnetite–hedenbergite veins (Fig. S4 in supporting information). Oxygen-isotope compositions of the measured grains are listed in Tables 2 and 3 and shown in Figs. 12a and 12b. Chondrule olivines plot along a ~slope-1 line, close to the CCAM line. Like in the Y-81020 and EET 90043 chondrules, the olivine grains in type I chondrules are ^{16}O-enriched relative to those in type II chondrules: $\Delta^{17}O$ range from −8.6‰ to −5.9‰ and from −3.6‰ to −2.4‰, respectively. Fayalite and magnetite are ^{16}O-depleted compared to chondrule olivine phenocrysts, and plot along a mass-dependent fractionation line with a slope of ~0.5 and $\Delta^{17}O$ of −1.8 ± 0.9‰. Fayalite
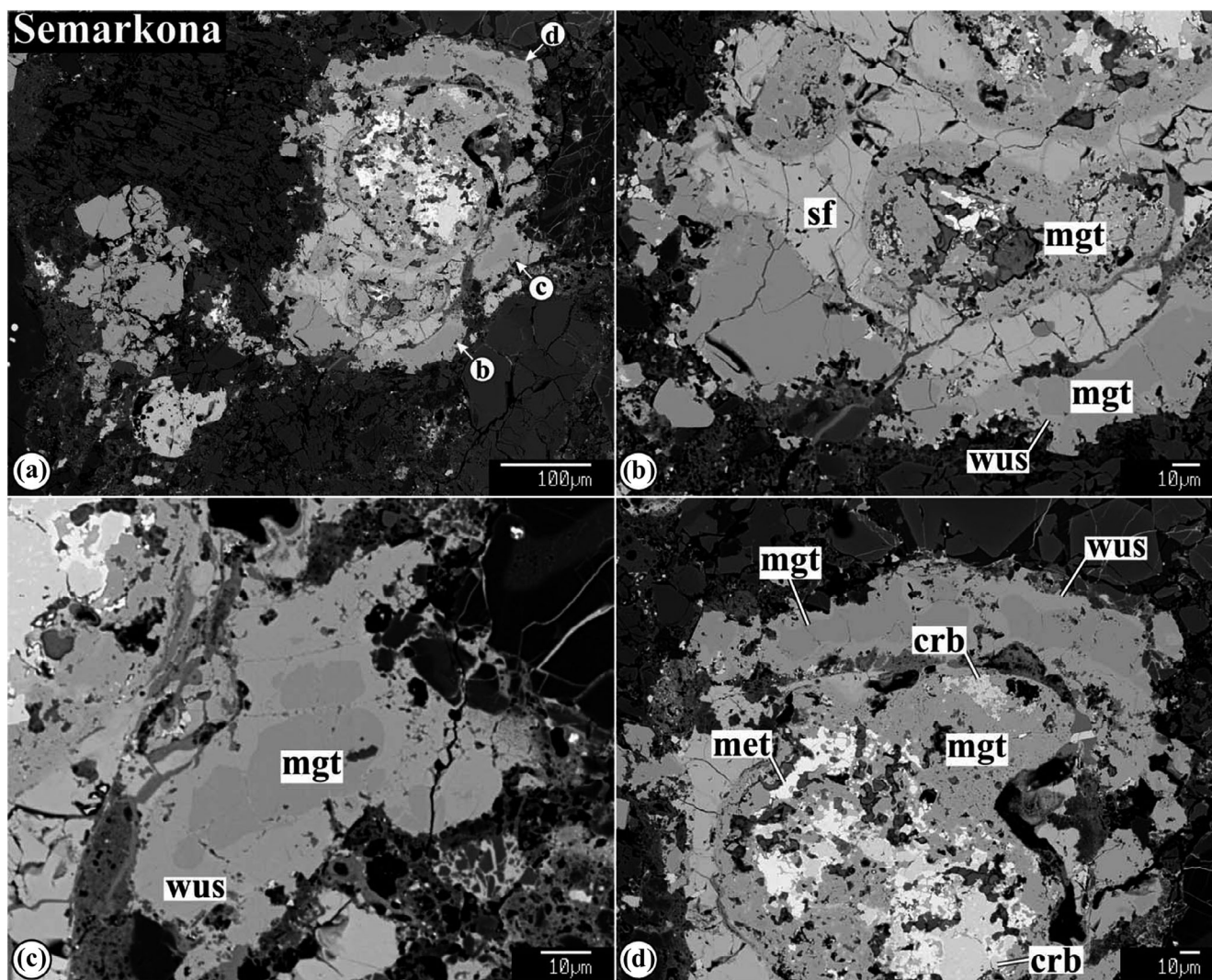
Fig. 8. Backscattered electron images of a magnetite–sulfide-Fe,Ni-metal-carbide nodule overgrown by coarse-grained magnetite in Semarkona, 4128-4. a) Arrows indicate locations of images shown in (b)–(d). Magnetite grains are extensively replaced by wüstite. crb = Fe,Ni-carbides; met = Fe,Ni-metal; mgt = magnetite; sf = sulfide; wus = wüstite.

grains have larger $\delta^{18}O$ values than magnetites (13−15‰ versus 8−13‰).

EET 90043 (CO3.1)

In EET 90043, we measured oxygen-isotope compositions of (1) fayalite grains in chondrules, matrix, and rims overgrowing chondrule fragments (Fig. S5), (2) compositionally pure coarse magnetite grains in chondrules and matrix (Fig. S6), and (3) chondrule olivines associated with fayalite (Fig. S7). These data are listed in Tables 2 and 3 and plotted in Figs. 12c and 12d. Compositions of chondrule olivines are similar to those in Y-81020, and plot along the PCM line. Olivines of type II chondrules are generally

^{16}O-depleted relative to those of type I chondrules ($\Delta^{17}O = -2$ versus -6 to -4‰, respectively). Fayalite and magnetite grains of different textural occurrences have similar oxygen-isotope compositions and plot along the mass-dependent fractionation line with $\Delta^{17}O$ of $\sim-0.3 \pm 0.8$‰; $\delta^{18}O$ range from ~6 to ~13‰. They are in oxygen-isotope disequilibrium with chondrule olivine phenocrysts.

Y-81020 (CO3.05)

Oxygen-isotope compositions of olivine and low-Ca pyroxene phenocrysts in the Y-81020 chondrules have been studied in detail by Tenner et al. (2013). The phenocrysts of type I chondrules are ^{16}O-enriched
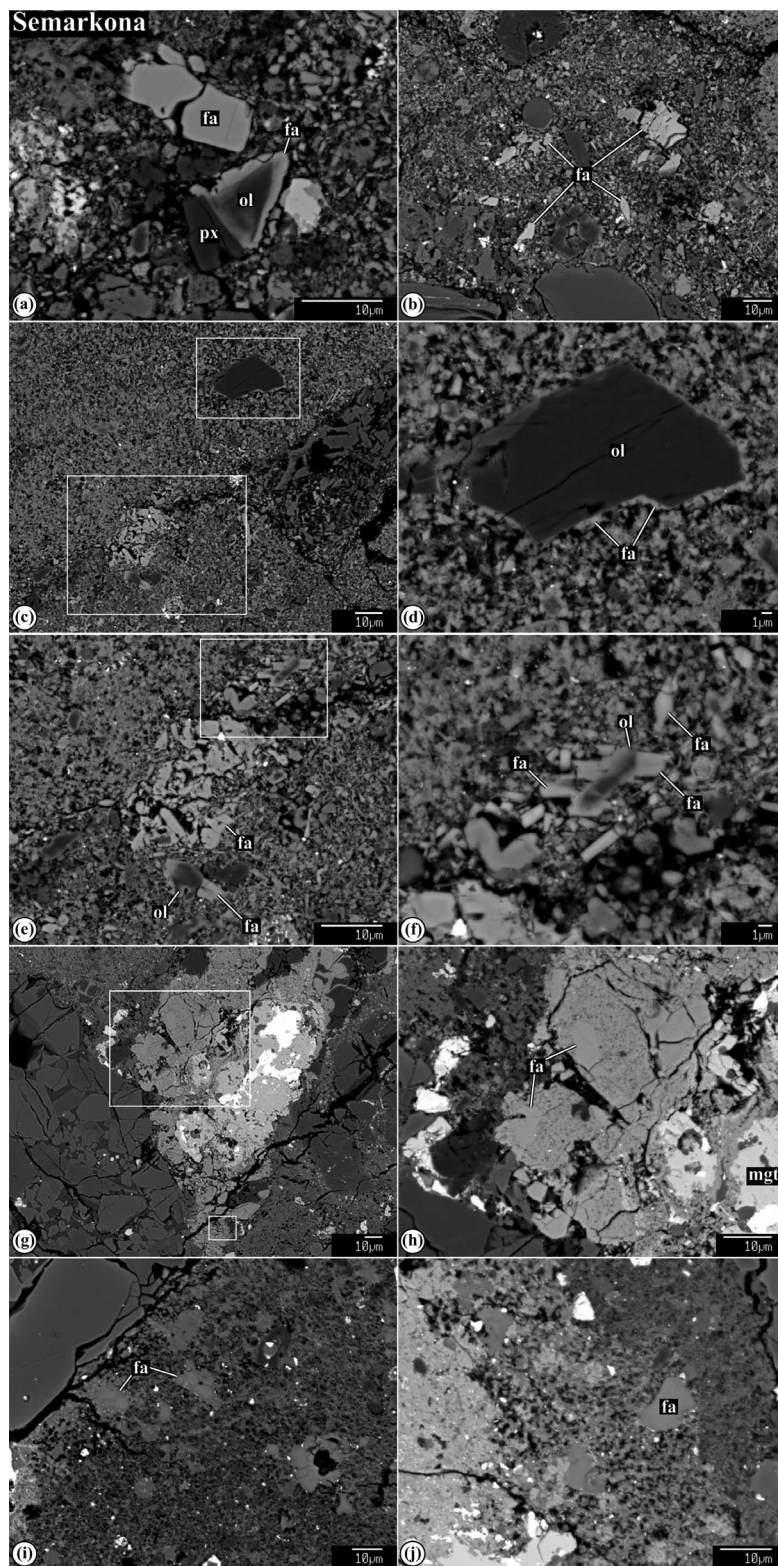
Fig. 9. Backscattered electron images of different textural occurrences of fayalite/ferroan olivine in matrix and fine-grained chondrule rims in Semarkona. Regions outlined in (c), (e), and (g) are shown in detail in (d), (f), and (h), respectively. fa = fayalite/ferroan olivine; mgt = magnetite; ol = ferromagnesian olivine.
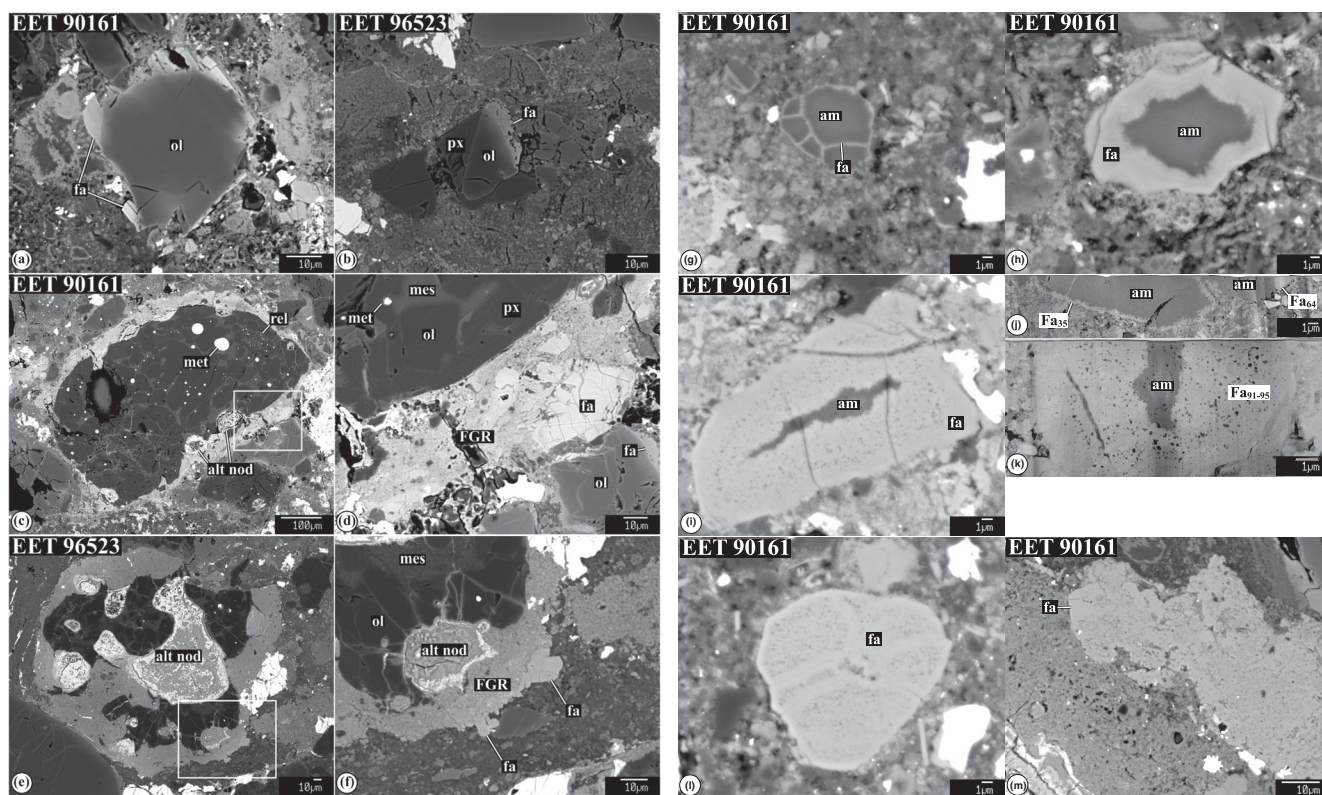
Fig. 10. Backscattered electron (a–i, l–n) and dark-field TEM (j, k) images of different textural occurrences of secondary fayalite in EET 90161, 15 (LL3.05) and EET 96523, 14 (LL3). a, b) Type II and I chondrule fragments overgrown by fayalite. c, d) Type I chondrule with a relict dusty olivine grain surrounded by a fine-grained rim containing abundant fayalite. The peripheral part of the chondrule contains abundant heavily altered opaque nodules. Type II chondrule fragment in the left-bottom corner is overgrown by fayalite. e, f) Type I chondrule with heavily altered opaque nodules surrounded by a fine-grained rim containing abundant fayalite. Subhedral fayalite grains occur in the outermost part of the rim. g–l) Fayalite replacing matrix amorphous silicates to various degrees. m) An aggregate of fine-grained fayalite in the matrix; subhedral fayalite grains occur in its peripheral part. n) Euhedral fayalite grain in the matrix. Regions outlined in (c) and (e) are shown in detail in (d) and (f), respectively. alt nod = altered opaque nodules; am = amorphous material; fa = fayalite; mes = mesostasis; met = Fe,Ni-metal; ol = olivine; phyl = phyllosilicates; px = low-Ca pyroxene.

relative to those of type II chondrules ($\Delta^{17}O$ range from −6.5 to −2.3 and from −2.9 to −1.6‰, respectively); both plot along the PCM line (Figs. 12e and 12f). Because of small grain sizes of fayalite in Y-81020, only compositionally pure magnetite grains overgrowing magnetite ± metal ± sulfide nodules in type I chondrules were measured (Fig. S8). Magnetite grains ($\Delta^{17}O = −0.2 \pm 0.6$‰) are in oxygen-isotope disequilibrium with chondrule phenocrysts and on a three-isotope oxygen diagram plot to the right from the PCM line ($\delta^{18}O$ range from ~8 to ~13‰; Table 2).

Kaba (CV3.1)

Oxygen isotopic compositions of fayalite, magnetite, chondrule olivine phenocrysts, and mesostasis/plagioclase (only type I chondrules were measured) are listed in Tables 4 and 5 and plotted in Fig. 13. Chondrule olivines

show a range of $\Delta^{17}O$ (−7.6 to −4.4‰) and on a three-isotope oxygen diagram plot along the PCM line. Similar results for chondrule olivine and low-Ca pyroxene phenocrysts in Kaba were reported by Hertwig et al. (2016). In contrast to isotopically uniform chondrules from Acfer 094 (Ushikubo et al. 2012), the plagioclase and glassy mesostasis in Kaba chondrules ($\Delta^{17}O = −0.5 \pm 0.9$‰) are in oxygen-isotope disequilibrium with olivine phenocrysts, and plot to the right of the CCAM line ($\delta^{18}O$ range from 13 to 15.6‰).

All three textural occurrences of fayalite (matrix, chondrule overgrowths, and coarse grains inside chondrules) analyzed in the same thin section, 35794, have similar oxygen isotopic compositions: $\delta^{18}O$ range from ~7 to ~9‰; $\Delta^{17}O$ range from −2.6 to −0.8‰ (average ± 2SE = −1.5 ± 1.3‰). Massive magnetite grains in type I chondrules measured in three different sections, 1052-1, SG2, and MP57, have a nearly identical
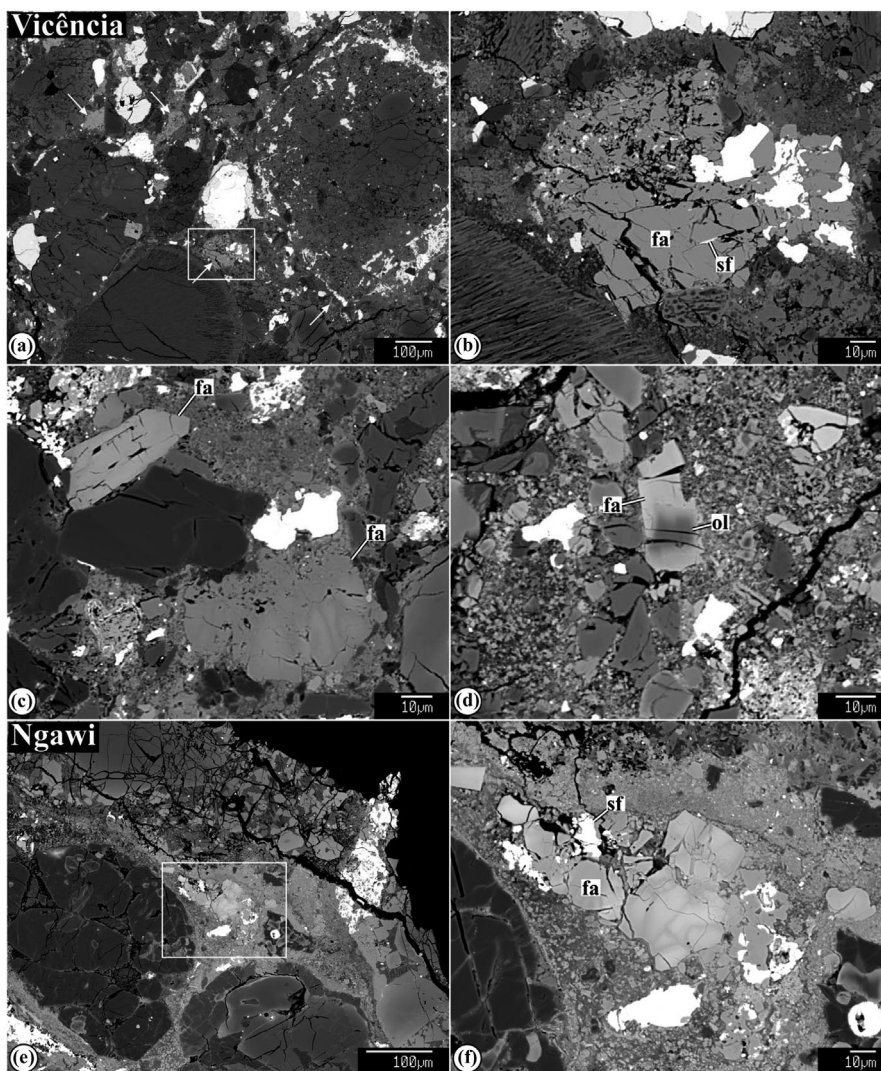
Fig. 11. Backscattered electron images of fayalite in unequilibrated ordinary chondrites Vicência (LL3.2) and Ngawi (LL3.0−3.6 breccia). Coarse fayalite grains occur in matrices of these meteorites and as overgrowths around chondrule fragments and opaque nodules. The fayalite grains often show inverse compositional zoning (see [c] and [f]). Regions outlined in (a) and (e) are shown in detail in (b) and (f), respectively. fa = fayalite; ol = ferromagnesian olivine; sf = sulfide.

average $\Delta^{17}O$, $-1.2 \pm 1.1‰$, and a relatively small range of $\delta^{18}O$, from ~0 to ~6‰. On a three-isotope oxygen diagram, compositions of fayalite and magnetite plot along the same mass-dependent fractionation line with $\Delta^{17}O$ of $-1.5 \pm 1‰$. Within uncertainty of our measurements, compositions of chondrule plagioclase/ mesostasis plot along this line as well.

Unequilibrated Ordinary Chondrites

Semarkona (LL3.0)

Oxygen-isotope compositions were measured in massive compositionally pure magnetite grains surrounding polymineralic opaque nodules composed of Fe,Ni-metal, Fe,Ni-carbides, magnetite, and sulfides in matrix and chondrules of Semarkona (Figs. S21−24). Due to small grain sizes, no oxygen-isotope compositions were measured in fayalite. The data obtained are listed in Table 6 and plotted in Figs. 14a and 14b. On a three-isotope oxygen diagram, magnetite grains plot along a mass-dependent fractionation line with $\Delta^{17}O$ of $4.3 \pm 1.2‰$, and show a much smaller range of $\delta^{18}O$ than previously reported by Choi et al. (1998), ~0 to ~+4‰ versus ~−4 to ~+9‰, respectively (Figs. 1c,d and 14a,b). The latter is at least partly due to the removal of SIMS spots with cracks and holes (Figs.S21−S24); these spots tend to have low $\delta^{18}O$ values (Table 6). In addition, several spots measured with a magnetite standard are in fact wüstite replacing magnetite (spots #18−20 in nodules #2 and #3 in
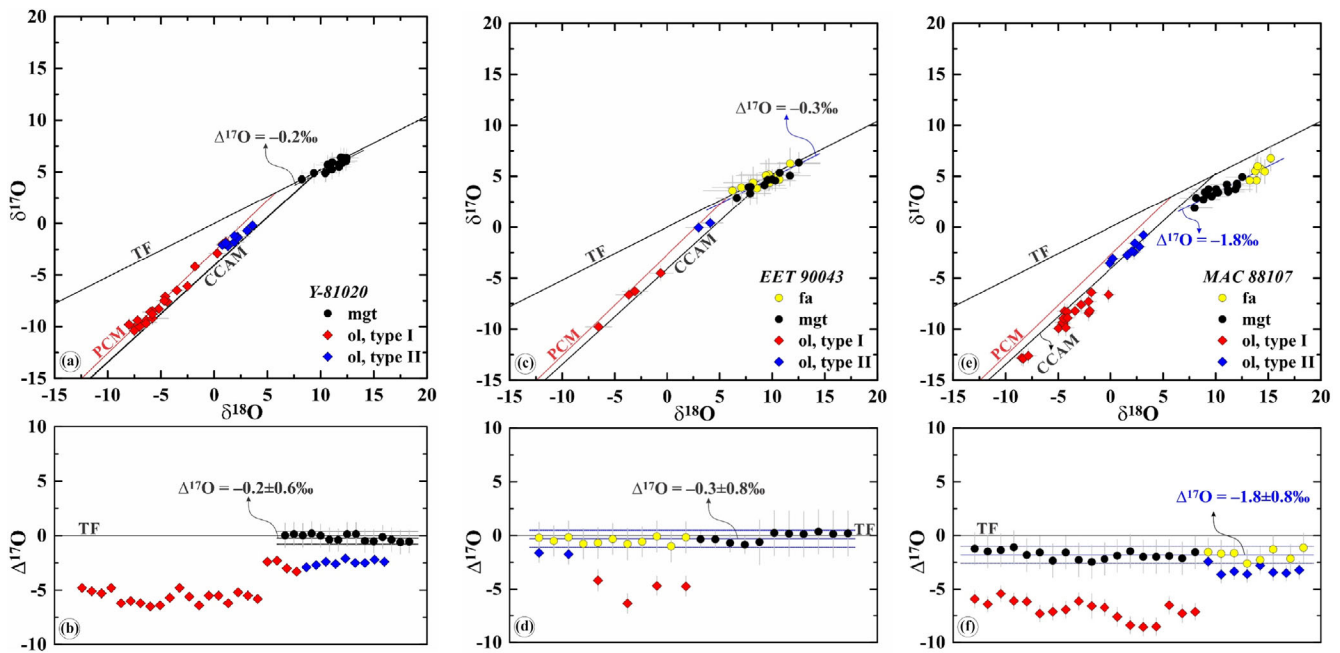
Fig. 12. Oxygen-isotope compositions of ferromagnesian olivines in type I and type II chondrules, fayalite, and magnetite in (a, b) MAC 88107 (CO3.1-like), (c, d) EET 90043 (CO3), and (e, f) Y-81020 (CO3.05). The terrestrial fractionation line (TFL), carbonaceous chondrite anhydrous mineral (CCAM) line, and primitive chondrule mineral (PCM) line are shown for reference. In (a), (c), and (e), the data are plotted as $\delta^{17}O$ versus $\delta^{18}O$; in (b), (d), and (f), the same data are plotted as $\Delta^{17}O$ ($=\delta^{17}O - 0.52 \times \delta^{18}O$). Ferromagnesian olivines from chondrules plot along ~slope-1 line; olivines in type I chondrules are ^{16}O-enriched relative to olivines in type II chondrules. In contrast, fayalite and magnetite plot along mass-dependent fractionation lines with a slope of ~0.5 and are ^{16}O-depleted relative to chondrule olivines. chd = chondrule; fa = fayalite; mgt = magnetite; ol = olivine. (Color figure can be viewed at wileyonlinelibrary.com.)

section 4218-4; Table 6). The coexisting wüstite and magnetite have similar $\Delta^{17}O$, but different $\delta^{18}O$, most likely due to use of an improper standard for wüstite. Oxygen isotopic compositions of magnetite and wüstite are in isotopic disequilibrium with olivine and low-Ca pyroxene phenocrysts in Semarkona chondrules having average $\Delta^{17}O$ of 0.6 ± 0.8‰ (Kita et al. 2010). Glassy mesostases in some of the Semarkona chondrules measured by Kita et al. (2010) are also in isotopic disequilibrium with chondrule phenocrysts, and follow a trend toward $\Delta^{17}O$ of magnetite (Figs. 14a and 14b).

EET 90161 (L3.05), MET 96523 (L3.1), and MET 00452 (L3.05)

Oxygen-isotope compositions of massive compositionally pure magnetite grains in chondrules and matrix of MET 00452 have similar $\Delta^{17}O$ to those in Semarkona (4.3 ± 0.9‰), but have slightly higher $\delta^{18}O$ (+2 to +7‰) (Table 6; Figs. 14c and 14d). No fayalite grains suitable for SIMS measurements have been identified in MET 00452.

In EET 90161 and MET 96503, only oxygen isotopic compositions of fayalite grains were measured. These grains have similarly high $\Delta^{17}O$ (4.8 ± 1.7‰ and 4.2 ± 1.6‰, respectively) and overlapping $\delta^{18}O$

($8-11$‰ and $3-10$‰, respectively; Table 6; Figs. 14c and 14d). Considering typical uncertainties of fayalite analyses, $2-3$‰, the average $\delta^{18}O$ values of ~7 and ~9‰, respectively, statistically are not different.

Ngawi (LL3.0–3.6 breccia) and Vicência (LL3.2)

Oxygen-isotope compositions of fayalite and magnetite in Ngawi and Vicência are listed in Table 6 and shown in Figs. 14e and 14f. Fayalite in both meteorites has similar $\Delta^{17}O$ of 4.1 ± 1.5‰ and 4.0 ± 0.6‰, respectively; $\delta^{18}O$ range from ~ 6 to ~11‰. Magnetite grains, measured only in Ngawi, have similar $\Delta^{17}O$ (4.5 ± 1.4‰), but a larger range in $\delta^{18}O$ (-3‰ to ~9‰). Most magnetite grains have lower $\delta^{18}O$ (-3‰ to ~3‰) than fayalite.

DISCUSSION

Origin of Magnetite and Fayalite in Ordinary and Carbonaceous Chondrites

The lack of oxygen isotopic equilibrium between chondrule phenocrysts and magnetite in all chondrites measured precludes formation of the latter by oxidation of chondrule melts followed by igneous
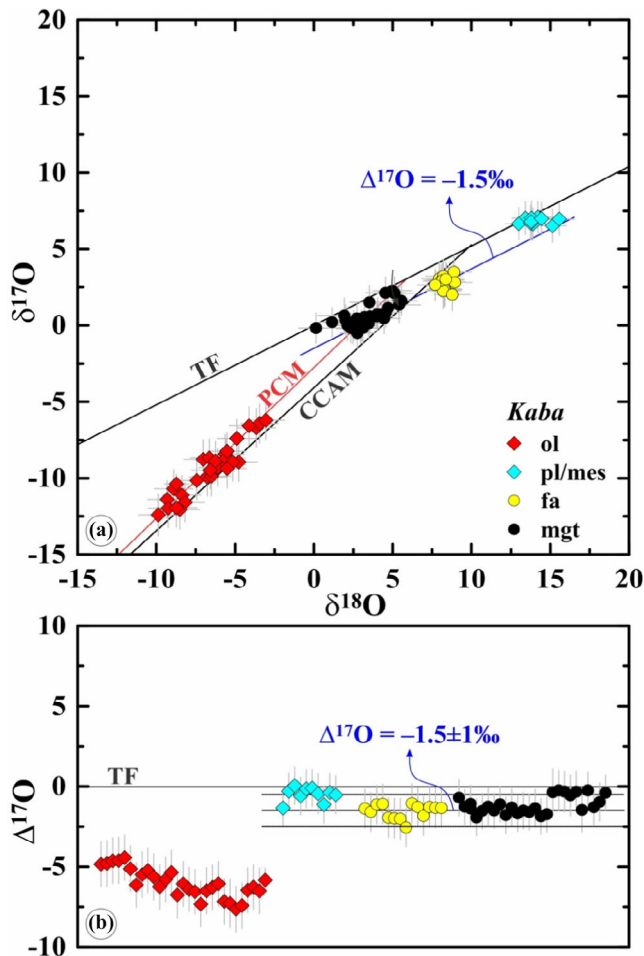
Fig. 13. Oxygen-isotope compositions of olivine phenocrysts and plagioclase/mesostasis in type I chondrules, and aqueously formed fayalite and magnetite in the $CV_{oxB}3.1$ carbonaceous chondrite Kaba. The terrestrial fractionation line (TFL), carbonaceous chondrite anhydrous mineral (CCAM) line, and primitive chondrule mineral (PCM) line are shown for reference. In (a), the data are plotted as $\delta^{17}O$ versus $\delta^{18}O$; in (b), the same data are plotted as $\Delta^{17}O$. Chondrule olivines plot along PCM line. Fayalite and magnetite plot along mass-dependent fractionation line with $\Delta^{17}O$ of $-1.5 \pm 1‰$ that corresponds to $\Delta^{17}O$ of aqueous fluid on the CV parent body. Plagioclase/mesostasis are in isotope disequilibrium with chondrule olivines, and plot to the right from the CCAM line, close to the mass-dependent fractionation line defined by fayalite and magnetite. fa = fayalite; mgt = magnetite; ol = forsteritic olivine; pl/mes = plagioclase/mesostasis. (Color figure can be viewed at wileyonlinelibrary.com.)

crystallization as was proposed by Marrocchi et al. (2016). Our mineralogical observations and oxygen-isotope measurements, thermodynamic analysis (Krot et al. 1998; Zolotov et al. 2006), and previously published ^{53}Mn-^{53}Cr ages of fayalite in ordinary and carbonaceous chondrites (Doyle et al. 2015) suggest instead that magnetite and fayalite in COs, MAC 88107, CVs, and UOCs formed in an asteroidal setting

during aqueous fluid–rock interaction. Magnetite formed by oxidation of Fe,Ni-metal $\pm$ sulfide nodules and by direct precipitation from a fluid as evidenced by subhedral grains overgrowing Fe,Ni-metal $\pm$ sulfide nodules. Magnetite formed by oxidation of Fe,Ni-metal contains elevated Cr and Ni concentrations; magnetite that precipitated from an aqueous fluid is compositionally pure $FeFe_2O_4$. Textural occurrences point to three mechanisms of fayalite formation in aqueously altered ordinary and carbonaceous chondrites studied, including (1) replacement of primary amorphous matrix silicates, (2) replacement of secondary magnetite, and (3) direct precipitation from a fluid. Recent TEM observations and hydrothermal experiments further support these mechanisms and confirm that FeO-rich olivine could form during thermal metamorphism, in the presence of an iron-rich fluid (Dobrică et al. 2018; Dobrică and Brearley 2020, 2021).

$\Delta^{17}O$ of Aqueous Fluids on the CO, CV, MAC 88107, and Ordinary Chondrite Parent Asteroids

In the fayalite and magnetite formation mechanisms described above (except formation of fayalite by replacement of amorphous silicates, where oxygen comes from the fluid and amorphous silicates), oxygen in fayalite and magnetite grains measured comes from an aqueous fluid. Therefore $\Delta^{17}O$ of the fayalite and magnetite must correspond to that of the fluid. Oxygen isotopic compositions of fayalite and magnetite in an individual chondrite suggest their formation in equilibrium with a fluid having similar $\Delta^{17}O$. The fact that $\Delta^{17}O$ of fayalite replacing amorphous silicates in UOCs is similar to that of magnetite in UOCs suggests that either the amorphous silicates experienced O-isotope exchange with the fluid prior to the fayalite formation or the fayalite reached equilibrium with the fluid.

The inferred $\Delta^{17}O$ of the fluids on the ordinary chondrite, CO, CV, and MAC 88107 parent bodies (~+4.3 $\pm$ 1.4‰, −0.2 $\pm$ 0.6‰, −1.5 $\pm$ 1‰, and −1.8 $\pm$ 0.8‰, respectively) indicate differences in $\Delta^{17}O$ of aqueous solutions of the ordinary and carbonaceous chondrite parent asteroids. Oxygen isotopic compositions of fayalite and magnetite in an individual chondrite have similar $\Delta^{17}O$, and therefore provide no clear evidence for evolution of oxygen isotopic composition of the fluid during crystallization of magnetite and fayalite in the meteorites studied. If $\Delta^{17}O$ of the fluid was not significantly modified during the fluid–rock interaction and isotopic exchange with anhydrous silicates, then the inferred $\Delta^{17}O$ of the fluids on the UOC, CO, CV, and MAC 88107 parent asteroids may be used as a proxy for $\Delta^{17}O$ of water ices that accreted into these asteroids.
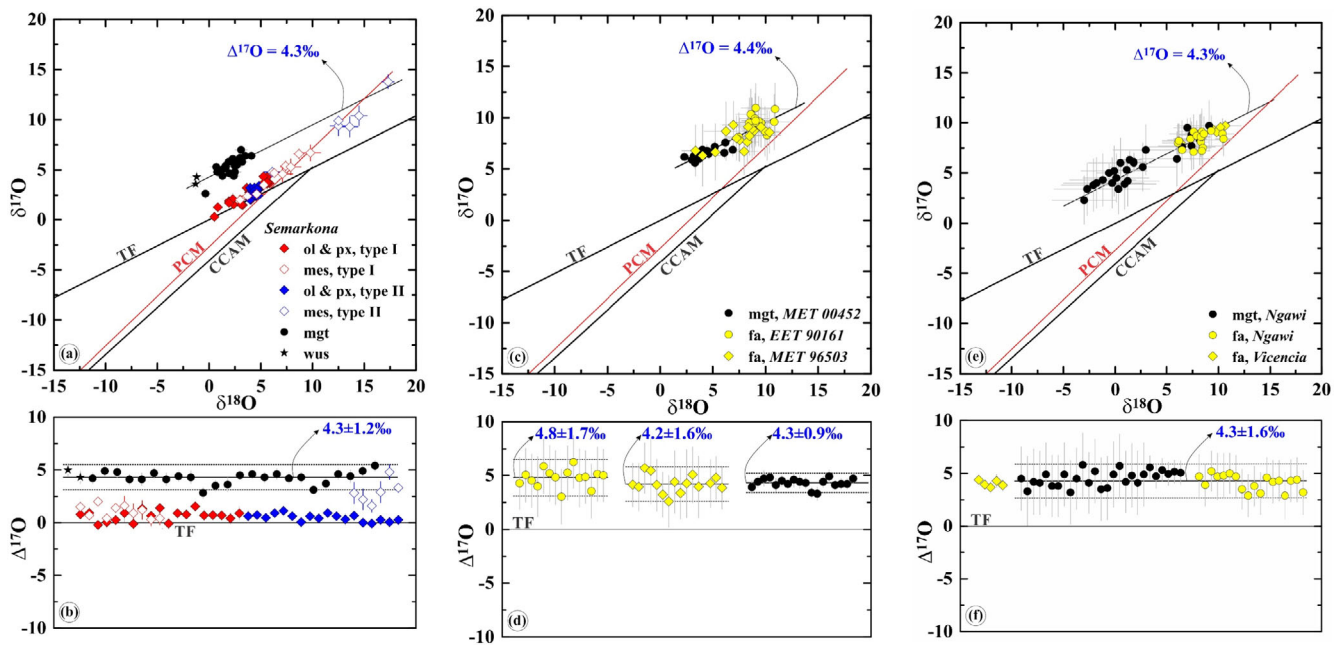
Fig. 14. Oxygen-isotope compositions of olivine and low-Ca pyroxene phenocrysts and mesostasis in chondrules (data from Kita et al. 2010), and aqueously formed magnetite and fayalite from unequilibrated ordinary chondrites (UOCs). a, b) Semarkona. c, d) EET 90161, MET 00452, and MET 96503. e, f) Ngawi and Vicência (data from Keil et al. 2015). The terrestrial fractionation line (TFL), carbonaceous chondrite anhydrous mineral (CCAM) line, and primitive chondrule mineral (PCM) line are shown for reference. In (a), (c), and (e), the data are plotted as $\delta^{17}O$ versus $\delta^{18}O$; in (b), (d), and (f), the same data are plotted as $\Delta^{17}O$. Magnetite and fayalite in UOCs plot along mass-dependent fractionation lines with $\Delta^{17}O$ of ~4–5‰, which correspond to $\Delta^{17}O$ of aqueous fluid on the LL parent body. There are no resolvable differences in $\Delta^{17}O$ of the fluid in different UOCs. Olivine and low-Ca pyroxene phenocrysts in Semarkona chondrules are in isotope disequilibrium with magnetite. Mesostases in type II and some type I chondrules are in isotope disequilibrium with chondrule phenocrysts; their $\Delta^{17}O$ approach to that of aqueous fluid suggesting that mesostases experienced oxygen-isotope exchange with the fluid. fa = fayalite; mes = mesostasis; mgt = magnetite; ol = ferromagnesian olivine; px = low-Ca pyroxene; wus = wüstite. (Color figure can be viewed at wileyonlinelibrary.com.)

Role of Aqueous Fluids in Oxygen Isotopic Exchange in Chondrule Mesostasis and Some Minerals of Refractory Inclusions

In most chondrules from carbonaceous chondrites of petrologic type 2–3.0 (e.g., Acfer 094 [C3.0 ungrouped], Yamato-81020 [CO3.0], and CR2–3s), olivine and low-Ca pyroxene phenocrysts, plagioclase, and glassy mesostases are in oxygen isotopic equilibrium, i.e., within an individual chondrule, these minerals have the same $\Delta^{17}O$ (within uncertainty of SIMS measurements), suggesting crystallization from a melt having approximately constant $\Delta^{17}O$ (e.g., Ushikubo et al. 2012; Tenner et al. 2013, 2015). In contrast, olivine phenocrysts and plagioclase/feldspathic mesostasis in Kaba and UOCs are in oxygen isotopic disequilibrium (Figs. 13 and 14), indicating postcrystallization oxygen-isotope exchange that affected only the plagioclase/feldspathic mesostasis (Bridges et al. 1999; Kita et al. 2010). A similar conclusion was reached by Rudraswami et al. (2011) based on oxygen-isotope disequilibrium between chondrule phenocrysts and plagioclase/mesostasis in the

Allende chondrules. On a three-isotope oxygen diagram (Fig. 13a), the olivine phenocrysts in the Kaba chondrules plot along the PCM line, whereas the plagioclase grains/mesostasis deviate to the right from the PCM line and plot along the mass-dependent fractionation line with $\Delta^{17}O$ of ~−1.5‰ defined by the Kaba magnetite and fayalite, suggesting the exchange resulted from interaction with the fluid. Plagioclase/feldspathic mesostasis in Kaba chondrules have nearly the same (within uncertainty of our SIMS measurements) $\Delta^{17}O$ as magnetite and fayalite, indicating that the exchange was nearly complete. The same process must have affected anorthite; perovskite; and, possibly, melilite in nonigneous fine-grained spinel-rich and fluffy Type A CAIs and AOAs from Kaba and UOCs, which are systematically ^{16}O-depleted relative to uniformly ^{16}O-rich spinel, forsterite, and Al, Ti-diopside (Krot et al. 2019a; Ebert et al. 2020). The mineralogically controlled oxygen isotopic exchange also affected grossite, krotite, Zr- and Sc-rich silicates, and oxides (davisite, eringaite, kangite, lakargiite, Y-rich perovskite, tazheranite, thortveitite, and zirconolite) in
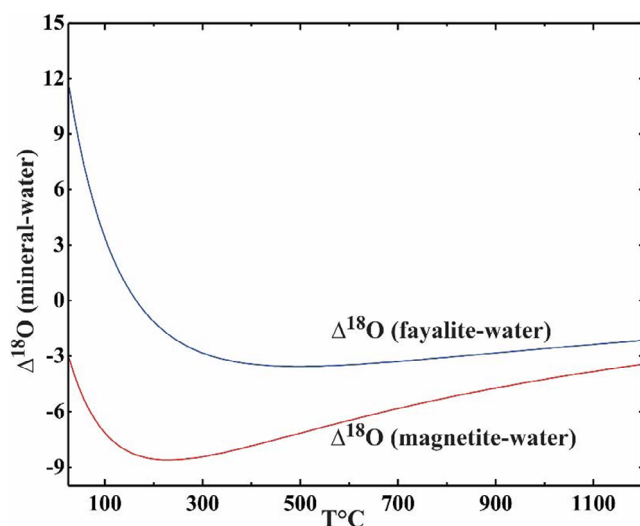
Fig. 15. $\Delta^{18}O$ versus temperature for magnetite-water and fayalite-water (from Zheng 1991, 1993). Equilibrium thermodynamic calculations of water–rock interaction predict formation of fayalite below 300 °C. In the temperature range of 75–300 °C, the equilibrium fractionation between fayalite and magnetite is between 6 and 15‰, which is in the range of the differences in $\delta^{18}O$ values between fayalite and magnetite in MAC 88107, CVs, and UOCs (Figs.12–14). (Color figure can be viewed at wileyonlinelibrary.com.)

grossite-bearing and ultrarefractory CAIs from the metasomatically altered CV and CO chondrites (Krot et al. 2019b, 2019c).

It has been previously shown that the presence of water leads to significantly enhanced oxygen-diffusion rates in many silicates compared to those under dry conditions (e.g., Farver [2010] and references therein). In plagioclase, the oxygen-diffusion coefficient under wet (hydrothermal) conditions (Giletti et al. 1978) is considerably higher than that under dry conditions (Yurimoto et al. 1989; Ryerson and McKeegan 1994; fig. 6a in Krot et al. 2019a). Under the inferred temperature of metasomatic alteration experienced by Kaba, 200–300 °C (Zolotov et al. 2006), a 10 μm-sized crystal of anorthite (typical grain sizes of plagioclase in Kaba chondrules) would completely exchange its oxygen isotopic composition with an aqueous fluid within ~0.1–0.001 Ma (fig. 6b in Krot et al. 2019a). This time scale may not be unreasonable for a duration of alteration on the CV parent asteroid. We note, however, that the duration of aqueous fluid activity on the CV parent asteroid is still poorly constrained.

Sources of Water in Ordinary and Carbonaceous Chondrite Parent Asteroids

It is generally accepted that aqueous alteration on the chondrite parent asteroids resulted from melting of

water ices that accreted together with the initially anhydrous silicates, Fe,Ni-metal, and sulfide grains (e.g., Zolensky et al. 2008; Brearley and Krot 2013; Krot et al. [2015] and references therein). To explain the differences in mineralogy, bulk chemical, and isotopic compositions of chondrite groups, it is suggested that accretion of chondrite asteroids took place shortly after chondrule formation (e.g., Alexander et al. 2008; Scott and Krot 2014). The relatively old ^{53}Mn-^{53}Cr ages of aqueously produced minerals, such as fayalite, kirschsteinite, and carbonates, in UOCs and CCs, 3–5 Ma after CV CAIs (Fujiya et al. 2012; Doyle et al. 2015; MacPherson et al. 2017), suggest an early addition of water ices, most likely contemporaneously with accretion of the chondrite parent bodies rather than during subsequent regolith gardening. Considering the inferred accretion ages of ordinary and carbonaceous chondrite parent bodies, ~2–3.5 Ma after CV CAIs (Fujiya et al. 2012), and the thermal structure of the 2–3 Ma-old protoplanetary disk (e.g., Ciesla and Cuzzi 2006; Morbidelli et al. 2016), these bodies most likely accreted outside the water–snow line. As a result, the chondrite water ices must have recorded oxygen-isotope composition of the nebular gas from which the water condensed in close proximity to the chondrule-forming regions plus water ices from different disk regions, which may have largely avoided thermal processing (e.g., outer solar system). We note that a dual origin of water, from the inner and outer solar system, has been inferred for a CM asteroid by Piani et al. (2018) based on oxygen-isotope compositions of carbonates and estimated D/H of water in the Paris CM carbonaceous chondrite.

The inferred $\Delta^{17}O$ of the fluids on the UOC, CO, CV, and MAC 88107 parent bodies (+4.3 ± 1.4‰, −0.2 ± 0.6‰, −1.5 ± 1‰, and −1.8 ± 0.8‰, respectively) indicate some differences in $\Delta^{17}O$ of aqueous solutions of the ordinary and carbonaceous chondrite parent asteroids. However, fayalite and magnetite in individual meteorites studied here have similar $\Delta^{17}O$, and therefore provide no clear evidence for (1) the presence of multiple sources of water ices in these meteorites or (2) evolution of $\Delta^{17}O$ of an aqueous fluid during crystallization of these minerals. We infer that anhydrous minerals of these meteorites had only a minor effect on the oxygen-isotope composition of aqueous fluids. In contrast, the extensively altered CM and CI chondrites have a range of $\Delta^{17}O$ values of calcite, dolomite, and phyllosilicates, which appear to correlate with the degree of aqueous alteration of the host meteorites (e.g., Benedix et al. 2003; Jenniskens et al. 2012).

If $\Delta^{17}O$ of the fluid was not significantly modified during fluid–rock interaction and isotopic exchange with anhydrous silicates, then the inferred $\Delta^{17}O$ of the fluids

on the CO, CV, UOC, and MAC 88107 chondrite parent asteroids may be used as a proxy for $\Delta^{17}O$ of water ices that accreted into these asteroids. This in turn may allow one inferring the source regions of these water ices.

The observed differences in $\Delta^{17}O$ of fayalite–magnetite assemblages in UOCs, COs, MAC 88107, and CVs indicate that water ices that accreted into their parent asteroids had different oxygen-isotope compositions, suggesting spatial and/or temporal variations in the oxygen-isotope compositions of water ices in the protoplanetary disk. The $\Delta^{17}O$ of magnetite and fayalite in these meteorites, however, are not as anomalous as the compositions of magnetite in cosmic symplectites ($\Delta^{17}O \sim +80‰$) in the ungrouped carbonaceous chondrite Acfer 094 (Sakamoto et al. 2007) and of unidentified grains in acid-insoluble organic matter ($\Delta^{17}O \sim +500‰$) in the CR carbonaceous chondrite Yamato 793495 (Hashizume et al. 2011). It is suggested that these isotopically anomalous materials formed during photodissociation of CO at low temperatures either in the protosolar molecular cloud (Yurimoto and Kuramoto 2004; Krot et al. 2020) and/or in the outer part of the protoplanetary disk (Lyons and Young 2005). Based on these observations, we infer that water ices that accreted into the parent bodies of OCs, COs, CVs and MAC 88107 were largely of a local origin rather than being delivered from the outer solar system. This conclusion is consistent with the inferred isotopically light composition of hydrogen in chondritic water compared with the isotopically heavy cometary water (Alexander et al. 2012). It is, however, inconsistent with the outer solar system origin (i.e., outside Jupiter's orbit) of the carbonaceous chondrite parent bodies inferred from their bulk Cr, Ti, Mo, and W isotopic compositions (e.g., Warren 2011; Van Kooten et al. 2016; Kruijer et al. 2017).

CONCLUSIONS

1. We characterized the mineralogy, petrology, and oxygen-isotope compositions of magnetite and nearly pure fayalite (Fa_{95-100}) from several weakly metamorphosed carbonaceous chondrites: Y-81020 (CO3.05), EET 90043 (CO3.1), MAC 88107 (CO3.1-like), and Kaba (oxidized Bali-like CV3.1), and UOCs: Semarkona (LL3.00), MET 00452 (LL3.05), MET 96503 (LL3.05), EET 910161 (LL3.05), Ngawi (LL3.0−3.6 breccia), and Vicência (LL3.2). Fayalite and magnetite in these meteorites associate with phyllosilicates, Fe,Ni-sulfides, ±hedenbergite, and ±kirschsteinite, and occur in all major chondritic components—chondrules, matrix, and refractory

inclusions (except OCs, where CAIs and AOAs are exceptionally rare).

2. Fayalite and magnetite in UOCs, COs, CVs, and MAC 88107 are in oxygen-isotope disequilibrium with chondrule olivine and low-Ca pyroxene phenocrysts, and plot along mass-dependent fractionation lines with a slope of ~0.5, but slightly different $\Delta^{17}O$ ($4.3 \pm 1.4‰$, $-0.2 \pm 0.6‰$, $-1.5 \pm 1‰$, and $-1.8 \pm 0.8‰$, respectively). Oxygen-isotope compositions of chondrule mesostasis/plagioclase in Kaba and Semarkona chondrules are in isotopic disequilibrium with chondrule phenocrysts; their $\Delta^{17}O$ approach those of fayalite and/or magnetite in their host meteorites.

3. The mineralogical observations, oxygen-isotope compositions, recently reported experimental data, and previously published thermodynamic analysis suggest that

− Fayalite and magnetite in COs, CVs, UOCs, and MAC 88107 resulted from fluid–rock interaction on the chondrite parent asteroids that occurred at low water-to-rock mass ratios (0.1−0.2) and elevated temperatures (~100−300 °C; Fig. 15).

− $\Delta^{17}O$ of the fayalite and magnetite reflects oxygen-isotope compositions of aqueous fluids on the host meteorite parent bodies.

− Under the inferred conditions of alteration, mesostasis/plagioclase in chondrules from Kaba and Semarkona experienced oxygen-isotope exchange with an aqueous fluid.

− The mineralogically controlled oxygen-isotope exchange may have also affected CAIs and AOAs in the metasomatically altered CVs, COs, and UOCs.

4. Although oxygen-isotope exchange between aqueous fluids and anhydrous silicates on the chondrite parent bodies must have somewhat modified $\Delta^{17}O$ of aqueous fluids, the lack of significant variations of $\Delta^{17}O$ of magnetite and fayalite within an individual chondrite implies that this modification was insignificant. If this is the case, the inferred $\Delta^{17}O$ of the fluids could be used as a proxy for $\Delta^{17}O$ of water ices that accreted into ordinary and carbonaceous chondrite parent bodies. The observed differences in $\Delta^{17}O$ of fayalite–magnetite assemblages in UOCs, CVs, COs, and MAC 88107 suggest that water ices that accreted into the ordinary chondrite and carbonaceous chondrite parent asteroids had different oxygen-isotope compositions, implying spatial and/or temporal variations in oxygen-isotope compositions of water in the protoplanetary disk. The inferred near-terrestrial compositions of the chondrite water ices are inconsistent with a significant influx of isotopically

heavy water ($\Delta^{17}O > 100‰$), which is hypothesized to be present in the outer solar system.

Editorial Handling—Dr. Alan E. Rubin

REFERENCES

Abreu N. M. and Brearley A. J. 2011. Deciphering the nebular and asteroidal record of silicates and organic material in the matrix of the reduced CV3 chondrite Vigarano. *Meteoritics & Planetary Science* 46:252–274.

Alexander C. M. O'D., Barber D. J., and Hutchison R. 1989. The microstructure of Semarkona and Bishunpur. *Geochimica et Cosmochimica Acta* 53:3045–3057.

Alexander C. M. O'D., Grossman J. N., Ebel D. S., and Ciesla F. J. 2008. The formation conditions of chondrules and chondrites. *Science* 320:1617–1619.

Alexander C. M. O'D., Bowden R., Fogel M. L., Howard K. T., Herd C. D. K., and Nittler L. R. 2012. The provenances of asteroids, and their contributions to the volatile inventories of the terrestrial planets. *Science* 337:721–723.

Amelin Y., Krot A. N., Hutcheon I. D., and Ulyanov A. A. 2002. Lead isotopic ages of chondrules and calcium-aluminum-rich inclusions. *Science* 297:1678–1683.

Benedix G. K., Leshin L. A., Farquhar J., Jackson T., and Thiemens M. H. 2003. Carbonates in CM2 chondrites: Constraints on alteration conditions from oxygen isotopic compositions and petrographic observations. *Geochimica et Cosmochimica Acta* 67:1577–1588.

Bouvier A. and Wadhwa M. 2010. The age of the solar system redefined by the oldest Pb-Pb age of a meteoritic inclusion. *Nature Geoscience* 3:637–641.

Brearley A. J. 1993. Matrix and fine-grained rims in the unequilibrated CO3 chondrite, ALHA77307: Origins and evidence for diverse, primitive nebular dust components. *Geochimica et Cosmochimica Acta* 57:1521–1550.

Brearley A. J. 1996. The nature of matrix in unequilibrated chondritic meteorites and its possible relationship to chondrules. In *Chondrules and the protoplanetary disk*, edited by Hewins R. H., Jones R. H., and Scott E. R. D. Cambridge: Cambridge University Press. pp. 137–152.

Brearley A. J. 1999. Origin of graphitic carbon and pentlandite in matrix olivines in the Allende meteorite. *Science* 285:1380–1382.

Brearley A. J. 2009. Matrix olivines in the metamorphosed CK chondrite NWA 1628: Possible affinities to olivines in the matrices of oxidized CV3 chondrites and dark inclusions (abstract #1791). 40th Lunar and Planetary Science Conference. CD-ROM.

Brearley A. J. and Jones R. H. 1998. Chondritic meteorites. In *Planetary materials*, edited by Papike J. J. Washington, D.C.: Mineralogical Society of America. pp. 1–398.

Brearley A. J., and Krot A. N. 2013. Metasomatism in the early solar system: The record from chondritic meteorites. In *Metasomatism and the chemical transformation of rock*, edited by Harlov D. E. and Austrheim H. Berlin: Springer-Verlag. pp. 659–789.

Bridges J. C., Franchi I. A., Sexton A. S., and Pillinger C. T. 1999. Mineralogical controls on the oxygen isotopic compositions of UOCs. *Geochimica et Cosmochimica Acta* 63:945–951.

Caplan C. E., Huss G. R., Hammer J. E., Ogliore R. C., and Nagashima K. 2015. Crystal orientation effects for oxygen-isotope measurements of magnetite and chromite (abstract #5333). 78th Annual Meeting of the Meteoritical Society.

Cassen P. 2001. Nebular thermal evolution and the properties of primitive planetary materials. *Meteoritics & Planetary Science* 36:671–700.

Choe W.-X., Huber H., Rubin A. E., Kallemeyn G. W., and Wasson J. T. 2010. Compositions and taxonomy of 15 unusual carbonaceous chondrites. *Meteoritics & Planetary Science* 45:531–554.

Choi B.-G. and Wasson J. T. 2003. Microscale oxygen isotopic exchange and magnetite formation in the Ningqiang anomalous carbonaceous chondrite. *Geochimica et Cosmochimica Acta* 67:4655–4660.

Choi B.-G., McKeegan K. D., Leshin L. A., and Wasson J. T. 1997. Origin of magnetite in oxidized CV chondrites: In situ measurement of oxygen isotope compositions of Allende magnetite and olivine. *Earth and Planetary Science Letters* 146:337–349.

Choi B.-G., McKeegan K. D., Krot A. N., and Wasson J. T. 1998. Extreme oxygen-isotope compositions in magnetite from unequilibrated ordinary chondrites. *Nature* 392:577–579.

Choi B.-G., Krot A. N., and Wasson J. T. 2000. Oxygen-isotopes in magnetite and fayalite in CV chondrites Kaba and Mokoia. *Meteoritics & Planetary Science* 35:1239–1249.

Choi B.-G., Itoh S., Yurimoto H., Rubin A. E., Wasson J. T., and Grossman J. N. 2008. Oxygen-isotopic composition of magnetite in the DOM 03238 CO3.1 chondrite (abstract #5272). 71st Annual Meteoritical Society Meeting.

Ciesla F. J. and Cuzzi J. N. 2006. The evolution of the water distribution in a viscous protoplanetary disk. *Icarus* 181:178–204.

Clayton R. N., Onuma N., Grossman L., and Mayeda T. K. 1977. Distribution of the pre-solar component in Allende and other carbonaceous chondrites. *Earth and Planetary Science Letters* 34:209–224.

Connelly J. N., Bizzaro M., Krot A. N., Nordlund Å., Wielandt D., and Ivanova M. A. 2012. The absolute chronology and thermal processing of solids in the solar protoplanetary disk. *Science* 338:651–655.

Davidson J., Nittler L. R., Alexander C. M. O'D., and Stroud R. M. 2014. Petrography of very primitive CO3 chondrites: Dominion range 08006, Miller range 07687, and four others (abstract# 1384). 45th Lunar and Planetary Science Conference. CD-ROM.

De Laeter J. R., Böhlke J. K., De Bièvre P., Hidaka H., Peiser H. S., Rosman K. J. R., and Taylor P. D. P. 2003. Atomic weights of the elements: Review 2000 (IUPAC Technical Report). *Pure and Applied Chemistry* 75:683–800.

Dobrică E. and Brearley A. J. 2011. Earliest stages of metamorphism and aqueous alteration observed in the fine-grained materials of two unequilibrated ordinary chondrites (abstract #2092). 42nd Lunar and Planetary Science Conference. CD-ROM.

Dobrică E. and Brearley A. J. 2014. Widespread hydrothermal alteration minerals in the fine-grained matrices of the Tieschitz unequilibrated ordinary chondrite. *Meteoritics & Planetary Science* 49:1323–1349.

Dobrică E. and Brearley A. J. 2020. Amorphous silicates in the matrix of Semarkona: The first evidence for the localized preservation of pristine matrix materials in the most unequilibrated ordinary chondrites. *Meteoritics & Planetary Science* 55:649–668.

Dobrică E. and Brearley A. J. 2021. Iron-rich olivine in the unequilibrated ordinary chondrite, MET 00526: Earliest stages of formation. *Meteoritics & Planetary Science* 55:2652–2669.

Dobrică E., Nuth J. A., and Brearley A. J. 2017a. Experimental hydrothermal alteration of amorphous materials: Insights into early fluid-assisted hydration processes on asteroids (abstract #2865). 48th Lunar and Planetary Science Conference. CD-ROM.

Dobrică E., Nuth J. A., and Brearley A. J. 2017b. Formation mechanism of iron-rich olivine: Experimental constrains into early fluid-assisted hydration and dehydration processes on asteroids (abstract #6342). 80th Annual Meeting of Meteoritical Society.

Dobrică E., Nuth J. A., Rietmeijer F., and Brearley A. J. 2018. Fayalite formation during hydrothermal experiments: Constraints on early fluid-assisted hydration processes on asteroids (abstract #2340). 49th Lunar and Planetary Science Conference. CD-ROM.

Dohmen R., Chakraborty S., Palme H., and Rammensee W. 1998. Solid-solid reactions mediated by a gas phase: An experimental study of reaction progress and the role of surfaces in the system olivine+iron metal. *American Mineralogist* 83:970–984.

Doyle P. M., Jogo K., Nagashima K., Krot A. N., Wakita S., Ciesla F. J., and Hutcheon I. D. 2015. Early aqueous activity on the carbonaceous and ordinary chondrite parent asteroids recorded by secondary fayalite. *Nature Communications* 6:1–10.

Ebel D. S. and Grossman L. 2000. Condensation in dust-enriched systems. *Geochimica et Cosmochimica Acta* 64:339–366.

Ebert S., Nagashima K., Krot A. N., and Bischoff A. 2020. Oxygen-isotope heterogeneity in the Northwest Africa 3358 (H3.1) refractory inclusions—Fluid-assisted isotopic exchange on the H-chondrite parent body. *Geochimica et Cosmochimica Acta* 282:98–112.

Farver J. R. 2010. Oxygen and hydrogen diffusion in minerals. *Reviews in Mineralogy and Geochemistry* 72:447–507.

Fedkin A. V. and Grossman L. 2010. Condensation of the high-FeO silicates in primitive chondrites: Still a problem (abstract #1448). 41st Lunar and Planetary Science Conference. CD-ROM.

Fujiya W., Sugiura N., Hotta H., Ichimura K., and Sano Y. 2012. Evidence for the late formation of hydrous asteroids from young meteoritic carbonates. *Nature Communications* 3:1–6.

Giletti B. J., Semet M. P., and Yund R. A. 1978. Studies in diffusion—III. Oxygen in feldspars: An ion microprobe determination. *Geochimica et Cosmochimica Acta* 42:45–57.

Greshake A. 1997. The primitive matrix components of the unique carbonaceous chondrite Acfer 094: A TEM study. *Geochimica et Cosmochimica Acta* 61:437–452.

Grossman J. N. and Brearley A. J. 2005. On the onset of metamorphism in ordinary and carbonaceous chondrites. *Meteoritics & Planetary Science* 40:87–122.

Grossman J. N. and Rubin A. E. 2006. Dominion Range 03238: A possible missing link in the metamorphic sequence of CO3 chondrites (abstract #1383). 37th Lunar and Planetary Science Conference. CD-ROM.

Grossman L. 2010. Vapor-condensed phase processes in the early solar system. *Meteoritics & Planetary Science* 45:7–20.

Grossman L., Beckett J. R., Fedkin A. V., Simon S. B., and Ciesla F. J. 2008. Redox conditions in the solar nebula: Observational, experimental and theoretical constraints. In *Oxygen in earliest solar system materials and processes*, edited by MacPherson G. J., Mittlefehldt D. W., Jones J. H., and Simon S. B. *Reviews in Mineralogy and Geochemistry* 68:93–141.

Hashizume K., Takahata N., Naraoka H., and Sano Y. 2011. Extreme oxygen isotope anomaly with a solar origin detected in meteoritic organics. *Nature Geoscience* 4:165–168.

Hertwig A., Defouilloy C., and Kita N. T. 2016. SIMS oxygen isotope study of chondrules in the least metamorphosed CV3 chondrite Kaba (abstract #6472). 79th Meteoritical Society Meeting.

Howard K. T., Alexander C. M. O'D., and Dyl K. A. 2014. PSD-XRD modal mineralogy of type 3.0 CO chondrites: Initial asteroidal water mass fractions and implications for CM chondrites (abstract #1830). 45th Lunar and Planetary Science Conference. CD-ROM.

Hsu W., Guan Y., Hua X., Wang Y., Leshin L. A., and Sharp T. G. 2006. Aqueous alteration of opaque assemblages in the Ningqiang carbonaceous chondrite: Evidence from oxygen isotopes. *Earth and Planetary Science Letters* 243:107–114.

Hua X. and Buseck P. R. 1995. Fayalite in the Kaba and Mokoia carbonaceous chondrites. *Geochimica et Cosmochimica Acta* 59:563–578.

Hua X., Huss G. R., Tachibana S., and Sharp T. G. 2005. Oxygen, silicon, and Mn–Cr isotopes of fayalite in the Kaba oxidized CV3 chondrite: Constraints for its formation history. *Geochimica et Cosmochimica Acta* 69:1333–1348.

Huberty J. M., Kita N. T., Kozdon R., Heck P. R., Fournell J. H., Spicuzza M. J., Xu H., and Valley J. W. 2010. Crystal orientation effects in $\delta^{18}O$ for magnetite and hematite by SIMS. *Chemical Geology* 276:269–283.

Hutcheon I. D., Krot A. N., Keil K., Phinney D. L., and Scott E. R. D. 1998. ^{53}Mn-^{53}Cr dating of fayalite formation in the CV3 chondrite Mokoia: Evidence for asteroidal alteration. *Science* 282:1865–1867.

Hutchison R., Alexander C. M. O'D., and Barber D. J. 1987. The Semarkona meteorite: First recorded occurrence of smectite in an ordinary chondrite, and its implications. *Geochimica et Cosmochimica Acta* 51:1875–1882.

Jenniskens P., Fries M. D., Yin Q.-Z., Zolensky M., Krot A. N., Sandford A. A., Sears D., Beauford R., Ebel D. S., Friedrich J. M., Nagashima K., Wimpenny J., Yamakawa A., Nishiizumi K., Hamajima Y., Caffee M. W., Welten K. C., Laubenstein M., Davis A. M., Simon S. B., Heck P. R., Young E. D., Kohl I. E., Thiemens M. H., Nunn M. H., Mikouchi T., Hagiya K., Ohsumi K., Cahill T. A., Lawton J. A., Barnes D., Steele A., Rochette P., Verosub K. L., Gattacceca J., Cooper G., Glavin D. P., Burton A. S., Dworkin J. P., Elsila J. E., Pizzarello S., Ogliore R., Schmitt-Kopplin P., Harir M., Hertkorn N., Verchovsky A., Grady M., Nagao K., Okazaki R., Takeuchi H., Hiroi T., Smith K., Silber E. A., Brown P. G., Albers J., Klotz D., Hankey M., Matson R., Fries J. A., Walker R. J., Puchtel I., Lee C.-T. A., Erdman M. E., Eppich G. R., Roeske S., Gabelica Z., Lerche M., Nuevo M., Girten B., Worden S. P., and The Sutter's Mill Meteorite Consortium. 2012. Radar-enabled recovery of the Sutter's Mill meteorite, a carbonaceous chondrite regolith breccia. *Science* 338:11583–1587.

Jogo K., Nakamura T., Noguchi T., and Zolotov M. Y. 2009. Fayalite in the Vigarano CV3 carbonaceous chondrite: Occurrences, formation age and conditions. *Earth and Planetary Science Letters* 287:320–328.

Jogo K., Nakamura T., Ito M., and Messenger S. 2010. Mn-Cr systematics of secondary fayalites in the CV3 carbonaceous chondrites A 881317, MET 00430 and MET 01074 (abstract #1573). 41st Lunar and Planetary Science Conference. CD-ROM.

Jogo K., Krot A. N., and Nagashima K. 2011. Oxygen-isotope compositions of fayalite and magnetite in CV carbonaceous chondrites Asuka-881317 and MET 00430: Implications for sources of water ice on the CV and ordinary chondrite parent asteroids (abstract). Workshop on Formation of the First Solids in the Solar System, held November 7–9, 2011, in Kauai, Hawaii. LPI contribution no. 1639:9114.

Keil K., Zucolotto M. E., Krot A. N., Doyle P. M., Telus M., Krot T. V., Greenwood R. C., Franchi I. A., Wasson J. T., Welten K. C., Caffee M. W., Sears D. W. G., Riebe M., Wieler R., Santos E., Scorzelli R. B., Gattacceca, J., Lagroix F., Laubenstein M., Mendes J. C., Schmitt-Kopplin P., Harir M., and Moutinho A. L. R. 2015. The Vicência meteorite fall: A new unshocked (S1) weakly metamorphosed (3.2) LL chondrite. *Meteoritics & Planetary Science* 50:1089–1111.

Kim H. Y., Choi B.-G., and Rubin A. E. 2009. Wüstite in the DOM 03238 magnetite-rich CO3.1 chondrite: Formation during atmospheric passage (abstract #5222). 72nd Annual Meteoritical Society Meeting.

Kita N. T., Nagahara H., Tachibana S., Tomomura S., Spicuzza M. J., Fournelle J. H., and Valley J. W. 2010. High precision SIMS oxygen three isotope study of chondrules in LL3 chondrites: Role of ambient gas during chondrule formation. *Geochimica et Cosmochimica Acta* 74:6610–6635.

Kojima T. and Tomeoka K. 1996. Indicators of aqueous alteration and thermal metamorphism on the CV3 parent body: Microtextures of a dark inclusion from Allende. *Geochimica et Cosmochimica Acta* 60:2651–2666.

Krot A. N., Zolensky M. E., Wasson J. T., Scott E. R. D., Keil K., and Ohsumi K. 1997. Carbide-magnetite-bearing type 3 ordinary chondrites. *Geochimica et Cosmochimica Acta* 61:219–237.

Krot A. N., Petaev M. I., Scott E. R. D., Choi B.-G., Zolensky M. E., and Keil K. 1998. Progressive alteration in CV3 chondrites: More evidence for asteroidal alteration. *Meteoritics & Planetary Science* 33:1065–1085.

Krot A. N., Brearley A. J., Petaev M. I., Kallemeyn G. W., Sears D. W. G., Benoit P. H., Hutcheon I. D., Zolensky M. E., and Keil K. 2000. Evidence for in situ growth of fayalite and hedenbergite in MacAlpine Hills 88107, ungrouped carbonaceous chondrite related to CM-CO clan. *Meteoritics & Planetary Science* 35:1365–1387.

Krot A. N., Petaev M. I., and Bland P. A. 2004. Multiple formation mechanisms of ferrous olivine in CV3 carbonaceous chondrites during fluid-assisted metamorphism. *Antarctic Meteorite Research* 17:154–172.

Krot A. N., Hutcheon I. D., Brearley A. J., Pravdivtseva O. V., Petaev M. I., and Hohenberg C. M. 2006. Timescales for secondary alteration of chondritic meteorites. In *Meteorites and the early solar system II*, edited by Lauretta D. and McSween H. Tucson, Arizona: University of Arizona Press. pp. 525–555.

Krot A. N., Doyle P., and Nagashima K. 2013. Secondary fayalite, hedenbergite, and magnetite in the CO3.0–3.1 carbonaceous chondrites Y-81020, EET 90043 and MAC 88107 (abstract #1754). 44th Lunar and Planetary Science Conference. CD-ROM.

Krot A. N., Alexander, C. M. O'D., Nagashima K., Ciesla F. J., Fujiya W., and Bonal L. 2015. Aqueous activity and sources of water on the chondrite parent asteroids. In *Asteroids IV*, edited by Michel P., DeMeo F. E., and Bottke W. F. Tucson, AZ: The University of Arizona Press. pp. 635–661.

Krot A. N., Nagashima K., and Simon S. B. 2017. Diverse alteration of DOM 08006 (CO3.0) and DOM 08004 (CO3.1) and its effect on oxygen isotopic compositions of grossite-bearing refractory inclusions (abstract #1084). 48th Lunar and Planetary Science Conference. CD-ROM.

Krot A. N., Nagashima K., Fintor K., and Pál-Molnár E. 2019a. Evidence for oxygen-isotope exchange in refractory inclusions from Kaba (CV3.1) carbonaceous chondrite during fluid-rock interaction on the CV parent asteroid. *Geochimica et Cosmochimica Acta* 246:419–435.

Krot A. N., Ma C., Nagashima K., Davis A. M., Beckett J. R., Simon S. B., Komatsu M., Fagan T. J., Brenker F., Ivanova M. A., and Bischoff A. 2019b. Mineralogy, petrography, and oxygen isotopic compositions of ultrarefractory inclusions from carbonaceous chondrites. *Geochemistry* 79:125519.

Krot A. N., Nagashima K., Simon S. B., Ma C., Connolly H. C., Huss G. R., Davis A. M., and Bizzarro M. 2019c. Mineralogy, petrography, and oxygen and aluminum-magnesium isotope systematics of grossite-bearing refractory inclusions. *Geochemistry* 79:125295.

Krot A. N., Nagashima K., Lyons J. R., Lee J.-E., and Bizzaro M. 2020. Oxygen isotopic heterogeneity in the early solar system inherited from the protosolar molecular cloud. *Science Advances* 6:eaay2724.

Kruijer T. S., Burkhardt C., Budde G., and Kleine T. 2017. Age of Jupiter inferred from the distinct genetics and formation times of meteorites. *Proceedings of the National Academy of Sciences* 114:6712–6716.

Lauretta D. S. and Buseck P. R. 2003. Opaque minerals in chondrites and fine-grained chondrules rims in the Bishunpur (LL3.1) chondrite. *Meteoritics & Planetary Science* 38:59–79.

Lodders K. 2003. Solar system abundances and condensation temperatures of the elements. *The Astrophysical Journal* 591:1220–1247.

Lyons J. R. and Young E. D. 2005. CO self-shielding as the origin of oxygen isotope anomalies in the early solar nebula. *Nature* 435:317–320.

MacPherson G. J., Nagashima K., Krot A. N., Doyle P. M., and Ivanova M. A. 2017. ^{53}Mn-^{53}Cr chronology of Ca-Fe silicates in CV3 chondrites. *Geochimica et Cosmochimica Acta* 201:260–274.

Makide K., Nagashima K., Krot A. N., Huss G. R., Hutcheon I. D., and Bischoff A. 2009. Oxygen- and magnesium-isotope compositions of calcium-aluminum-rich inclusions from CR2 carbonaceous chondrites. *Geochimica et Cosmochimica Acta* 73:5018–5050.

Marrocchi Y., Chaussidon M., Piani L., and Libourel G. 2016. Early scattering of the solar protoplanetary disk recorded in meteoritic chondrules. *Science Advances* 2:11601001.

Marrocchi Y., Bekaert D. V., and Piani L. 2018. Origin and abundance of water in carbonaceous chondrites. *Earth and Planetary Science Letters* 482:23–32.

Morbidelli A., Bitsch B., Crida A., Gounelle M., Guillot T., Jacobsen S., Johansen A., Lambrechts M., and Lega E. 2016. Fossilized condensation lines in the solar system protoplanetary disk. *Icarus* 267:368–376.

Nagahara H. 1984. Matrices of type 3 ordinary chondrites—Primitive nebular records. *Geochimica et Cosmochimica Acta* 48:2581–2595.

Nagashima K., Krot A. N., and Komatsu M. 2017. ^{26}Al-^{26}Mg systematics in chondrules from Kaba and Yamato 980145 CV3 chondrites. *Geochimica et Cosmochimica Acta* 201:303–319.

Palme H. and Fegley B. 1990. High temperature condensation of iron-rich olivine in the solar nebula. *Earth and Planetary Science Letters* 101:180–195.

Piani L. and Marrocchi Y. 2018. Hydrogen isotopic composition of water in CV-type carbonaceous chondrites. *Earth and Planetary Science Letters* 504:64–71.

Piani L., Yurimoto H., and Remusat L. 2018. A dual origin for water in carbonaceous asteroids revealed by CM chondrites. *Nature Astronomy* 2:317–323.

Pouchou J. L. and Pichoir F. 1984. A new model for quantitative X-ray microanalysis. Part I: Application to the analysis of homogeneous samples. *La Recherche Aerospatiale* 3:13–38.

Rasmussen M. G., Evans B. W., and Kuehner S. M. 1998. Low temperature fayalite, greenalite, and minnesotaite from the Overlook gold deposit, Washington: Phase relations in the system FeO-SiO$_2$-H$_2$O. *Canadian Minerals* 36:147–162.

Rubin A. E. and Li Y. 2019. Formation and destruction of magnetite in CO3 chondrites and other chondrite groups. *Geochemistry* 79:125528.

Rudraswami N. G., Ushikubo T., Nakashima D., and Kita N. T. 2011. Oxygen isotope systematics of chondrules in the Allende CV3 chondrite: High precision ion microprobe studies. *Geochimica et Cosmochimica Acta* 75:7596–7611.

Ryerson F. J. and McKeegan K. D. 1994. Determination of oxygen self-diffusion in åkermanite, anorthite, diopside, and spinel: Implications for oxygen isotopic anomalies and the thermal histories of Ca-Al-rich inclusions. *Geochimica et Cosmochimica Acta* 58:3713–3734.

Sakamoto N., Seto Y., Itoh S., Kuramoto K., Fujino K., Nagashima K., Krot A. N., and Yurimoto H. 2007. Oxygen isotope evidence for remnants of the early solar system primordial water. *Science* 317:231–233.

Scott E. R. D. and Krot A. N. 2014. Chondrites and their components. In *Meteorites and cosmochemical processes*, vol. 1, edited by Davis, A. M., Holland, H. D., and Turekian, K. K. Treatise on Geochemistry. Oxford: Elsevier. pp. 65–137.

Tenner T. J., Ushikubo T., Kurahashi E., Kita N. T., and Nagahara H. 2013. Oxygen isotope systematics of chondrule phenocrysts from the CO3.0 chondrite Yamato 81020: Evidence for two distinct oxygen isotope reservoirs. *Geochimica et Cosmochimica Acta* 102:226–245.

Tenner T. J., Nakashima D., Ushikubo T., Kita N. T., and Weisberg M. K. 2015. Oxygen isotope ratios of FeO-poor chondrules in CR3 chondrites: Influence of dust enrichment and H$_2$O during chondrule formation. *Geochimica et Cosmochimica Acta* 148:228–250.

Tonui E., Zolensky M., Lipschutz M., and Okudaira K. 2001. Petrographic and chemical evidence of thermal metamorphism in new carbonaceous chondrites. *Meteoritics & Planetary Science* 36:A207.

Tonui E. K., Zolensky M. E., Hiroi T., Wang M.-S., and Lipschutz M. E. 2002. Petrographic, chemical and spectroscopic data on thermally metamorphosed carbonaceous chondrites (abstract #1288). 33rd Lunar and Planetary Science Conference. CD-ROM.

Ushikubo T., Kimura M., Kita N. T., and Valley J. W. 2012. Primordial oxygen isotope reservoirs of the solar nebula recorded in chondrules in Acfer 094 carbonaceous chondrite. *Geochimica et Cosmochimica Acta* 90:242–264.

Van Kooten E. M. M. E., Wielandt D., Schiller M., Nagashima K., Thomen A., Larsen K. K., Olsen M. B., Nordlund A., Krot A. N., and Bizzaro M. 2016. Isotopic evidence for primordial molecular cloud material in metal-rich carbonaceous chondrites. *Proceedings of the National Academy of Sciences* 113:2011–2016.

Warren P. H. 2011. Stable-isotopic anomalies and the accretionary assemblage of the Earth and Mars: A subordinate role for carbonaceous chondrites. *Earth and Planetary Science Letters* 311:93–100.

Wasson J. T. and Krot A. N. 1994. Fayalite-silica association in unequilibrated ordinary chondrites—Evidence for aqueous alteration on a parent body. *Earth and Planetary Science Letters* 122:403–416.

Weinbruch S., Palme H., Muller W. F., and El Goresy A. 1990. FeO-rich rims and veins in Allende forsterite: Evidence for high temperature condensation at oxidizing conditions. *Meteoritics* 25:115–125.

Weisberg M. K. and Prinz M. 1998. Fayalitic olivine in CV3 chondrite matrix and dark inclusions: A nebular origin. *Meteoritics & Planetary Science* 33:1087–1111.

Weisberg M. K., Prinz M., Clayton R. N., Mayeda T. K., Grady M. M., Franchi I., Pillinger C. T., and Kallemeyn G. W. 1996. The K (Kakangari) chondrite grouplet. *Geochimica et Cosmochimica Acta* 60:4253–4263.

Weisberg M. K., Zolensky M. K., and Prinz M. 1997. Fayalitic olivine in matrix of the Krymka LL3.1 chondrite: Vapor-solid growth in the solar nebula. *Meteoritics & Planetary Science* 32:791–801.

Yurimoto H. and Kuramoto K. 2004. Molecular cloud origin for the oxygen isotope heterogeneity in the solar system. *Science* 305:1763–1766.

Yurimoto H., Morioka M., and Nagasawa H. 1989. Diffusion in single crystals of melilite. I—Oxygen. *Geochimica et Cosmochimica Acta* 53:2387–2394.

Zheng Y.-F. 1991. Calculation of oxygen isotope fractionation in metal oxides. *Geochimica et Cosmochimica Acta* 55:2299–2307.

Zheng Y.-F. 1993. Calculation of oxygen isotope fractionation in anhydrous silicate minerals. *Geochimica et Cosmochimica Acta* 57:1079–1091.

Zolensky M., Krot A. N., and Benedix G. 2008. Record of low-temperature alteration in asterois. In *Oxygen in the solar system*, edited by MacPherson G. J. *Reviews in Mineralogy and Geochemistry* 68:429–463.

Zolotov M. Y., Mironenko M. V., and Shock E. L. 2006. Thermodynamic constraints on fayalite formation on parent bodies of chondrites. *Meteoritics & Planetary Science* 41:1775–1796.

SUPPORTING INFORMATION

Additional supporting information may be found in the online version of this article.

Table S1. Electron microprobe analyses of chondrule olivines and pyroxenes and secondary fayalite, hedenbergite, and kirschsteinite in CO3-like and CO3 carbonaceous chondrites MAC 88107, EET 90043 and Y-81020 measured for oxygen isotopic compositions.

Table S2. Representative electron microprobe analyses of magnetite in EET 90043.

Table S3. Electron microprobe analyses of chondrule olivines, pyroxenes and plagioclase and secondary fayalite in Kaba.

Table S4. Representative electron microprobe analyses of fayalite in matrices of unequilibrated ordinary chondrites.

Fig. EA1. Combined X-ray elemental maps in Mg (red), Ca (green) and Al (blue) of a polished thin section MAC 88107, *50* (CO3.1-like). Locations of chondrules and mineral grains measured for oxygen isotopic compositions are numbered. The numbers correspond to object number listed in Tables 2, 3 and EA1.

Fig. EA2. BSE images of fayalite grains from MAC 88107, *50* measured for oxygen isotopic compositions. Spots numbers correspond to analysis number listed in Table 3. fa = fayalite; hed = hedenbergite; mgt = magnetite; sf = sulfide.

Fig. EA3. BSE images of magnetite grains in chondrules and matrix of MAC 88107, *50* measured for oxygen isotopic compositions. Spot numbers correspond to analysis number listed in Table 3. chd = chondrule; fa = fayalite; hed = hedenbergite; mgt = magnetite; ol = olivine; px = low-Ca pyroxene; sf = sulfide; mx = matrix.

Fig. EA4. BSE images of chondrules and chondrule fragments from MAC 88107, *50* measured for oxygen

isotopes. Spots analyzed are numbered. Numbers correspond to analysis number listed in Tables 2 and EA1. chd = chondrule; chr = chromite; fa = fayalite; frg = fragment; gl = glass; hed = hedenbergite; mgt = magnetite; ol = olivine; px = low-Ca pyroxene.

Fig. EA5. BSE images of fayalite grains from EET 90043, *7* measured for oxygen isotopic compositions. Spots numbers correspond to analysis number listed in Table 3. Images in "a", "c", "f", "h", "k", "m", "o", "q" and "s" were taken before SIMS measurements; regions outlined in these images are shown in detail in "b", "d, e", "g", "i, j", "l", "n", "p", "r", and "t", respectively. chd = chondrule; fa = fayalite; frg = fragment; mgt = magnetite; ol = olivine; px = low-Ca pyroxene; sf = sulfide.

Fig. EA6. BSE images of magnetite grains in chondrules and matrix of EET 90043, *7* measured for oxygen isotopic compositions. Spots numbers correspond to analysis number listed in Table 3. chd = chondrule; met = Fe,Ni-metal; mgt = magnetite; mx = matrix; ol = olivine; px = low-Ca pyroxene; sf = sulfide.

Fig. EA7. BSE images of chondrules and chondrule fragments from EET 90043, *7* measured for oxygen isotopes. Spots analyzed are numbered. Numbers correspond to analysis number listed in Table 2. chd = chondrule; fa = fayalite; frg = fragment; mgt = magnetite; ol = olivine; px = low-Ca pyroxene.

Fig. EA8. BSE images of magnetite grains from Y-81020, *56* (CO3.05) measured for oxygen isotopic compositions. Spot numbers correspond to analysis number listed in Table 2. met = Fe,Ni-metal; mgt = magnetite; ol = olivine; px = low-Ca pyroxene; sf = sulfide.

Fig. EA9. Combined X-ray elemental maps in Mg (red), Ca (green) and Al (blue) of a polished thin section Kaba, *1052-1* (CV3.1). Locations of regions studied for oxygen isotopic compositions are numbered.

The numbers correspond to object number listed in Tables 4 and 5.

Fig. EA10. BSE images of chondrule #2 from Kaba, *1052-1*. Spots measured for oxygen isotopic compositions are numbered. The numbers correspond to analysis number listed in Tables 4 and 5. alt = secondary alteration minerals; mgt = magnetite; ol = olivine; sf = sulfide.

Fig. EA11. BSE images of chondrules #6 (a−h) and #1 (i−n) from Kaba, *1052-1*. Spots measured for oxygen isotopic compositions are numbered. Numbers correspond to analysis number listed in Tables 4 and 5. Spots with cracks or holes have red numbers; these spots were not plotted in Fig. 13. mgt = magnetite; ol = olivine; sf = sulfide.

Fig. EA12. BSE images of chondrules #4 (a−g) and #10 (h−k) from Kaba, USNM 1052-1. Spots measured for oxygen isotopic compositions are numbered. Numbers correspond to analysis number listed in Tables 4 and 5. Spots with cracks or holes have red numbers; these spots were not plotted in Fig. 13. fa = fayalite; mgt = magnetite; ol = olivine; phyl = phyllosilicates; px = low-Ca pyroxene; sf = sulfide.

Fig. EA13. Combined X-ray elemental maps in Mg (red), Ca (green) and Al (blue) of a polished thin section Kaba, *SG2* (CV3.1). Locations of regions studied for oxygen isotopic compositions are numbered. The numbers correspond to object number listed in Tables 4, 5, and EA3.

Fig. EA14. BSE images of chondrules #3 (a−c), #7 (d−j), #9 (k−l), #8 (m−n), and #2 (o−p) from Kaba, SG2 with measured oxygen isotopic compositions of plagioclase/mesostasis and/or magnetite. Spot number corresponds to analysis number listed in Tables 4 and 5. Spots with cracks or holes have red numbers; these spots were not plotted in Fig. 13. mgt = magnetite; ol = olivine; phyl = phyllosilicates; px = low-Ca pyroxene; sf = sulfide.

Fig. EA15. Combined X-ray elemental maps in Mg (red), Ca (green) and Al (blue) of a polished thin section Kaba, *HX3* (CV3.1). Locations of regions studied for oxygen isotopic compositions are numbered. The numbers correspond to object number listed in Tables 4, 5, and EA3.

Fig. EA16. BSE images of chondrules #1 (a−f) and #2 (g−k) from Kaba, HX3. Spots measured for oxygen isotopic compositions are numbered. Numbers correspond to analysis number listed in Tables 4 and 5. o = olivine; p = plagioclase/mesostasis.

Fig. EA17. Combined X-ray elemental maps in Mg (red), Ca (green) and Al (blue) of a polished thin section Kaba, *35794* (CV3.1). Locations of regions studied for oxygen isotopic compositions are numbered. The numbers correspond to object number listed in Table 5 and EA3.

Fig. EA18. BSE images of fayalite in chondrules and matrix regions from Kaba, *35794*. Spots measured for oxygen isotopic compositions are numbered. Numbers correspond to analysis number listed in Table 5. fa = fayalite; mgt = magnetite; sf = sulfide.

Fig. EA19. Combined X-ray elemental maps in Mg (red), Ca (green) and Al (blue) of a polished thin section Kaba, *MP57* (CV3.1). Locations of regions studied for oxygen isotopic compositions are numbered. The numbers correspond to object number listed in Table 5 and EA3.

Fig. EA20. BSE images of magnetite grains in chondrules #4 (a−e) and #5 (f−i) from Kaba, *MP57* measured for oxygen isotopic compositions. The spot numbers correspond to analysis number listed in Table 5. Spots with cracks or holes have red numbers; these spots were not plotted in Fig. 13. met = Fe,Ni-metal; mgt = magnetite; sf = sulfide.

Fig. EA21. (a) Combined X-ray elemental map in Mg (red), Ca (green) and Al (blue) and (b) BSE map of a polished thin section Semarkona, *1805-5* (LL3.00). Locations of regions with magnetite measured for oxygen isotopic compositions are numbered. The numbers correspond to object numbers listed in Tables 6 and EA4.

Fig. EA22. BSE images of magnetite grains in Semarkona, *1805-5* measured for oxygen isotopic compositions. The spot numbers correspond to analysis number listed in Table 6. Spots with cracks or holes have red numbers; these spots were not plotted in Fig. 14. crb = Fe,Ni-carbides; met = Fe,Ni-metal; mgt = magnetite; sf = sulfide.

Fig. EA23. (a) Combined X-ray elemental map in Mg (red), Ca (green) and Al (blue) and (b) BSE map of a polished thin section Semarkona, *4128-4* (LL3.00). Locations of regions with magnetite measured for oxygen isotopic compositions are numbered. The numbers correspond to object numbers listed in Tables 6 and EA4.

Fig. EA24. BSE images of magnetite grains in Semarkona, *4218-4* measured for oxygen isotopic compositions. The spot numbers correspond to analysis number listed in Table 6. Spots with cracks or holes are indicated in red; these were not plotted in Fig. 14. crb = Fe, Ni-carbides; met = Fe,Ni-metal; mgt = magnetite; sf = sulfide; wus = wüstite

Fig. EA25. BSE map of a polished thin section MET 00452, *16* (LL3). Locations of regions with magnetite measured for oxygen isotopic compositions are numbered. The numbers correspond to object numbers listed in Tables 6 and EA4.

Fig. EA26. BSE images of magnetite grains in MET 00452, *16* measured for oxygen isotopic compositions. The spot numbers correspond to analysis number listed

in Table 6. Spots with cracks or holes are indicated in red; these were not plotted in Fig. 14. met = Fe,Ni-metal; mgt = magnetite; sf = sulfide.

Fig. EA27. BSE map of a polished thin section MET 00452, *18* (LL3). Locations of regions with magnetite measured for oxygen isotopic compositions are numbered. The numbers correspond to object numbers listed in Tables 6 and EA4.

Fig. EA28. BSE images of magnetite grains in MET 00452, *18* measured for oxygen isotopic compositions. The spot numbers correspond to analysis number listed in Table 6. Spots with cracks or holes are indicated in red; these were not plotted in Fig. 14. Regions outlined in "a" and "g" are shown in detail in "b−d" and "h−j", respectively. met = Fe,Ni-metal; mgt = magnetite; sf = sulfide.

Fig. EA29. BSE images of fayalite grains in EET 90161, *15* measured for oxygen isotopic compositions. The spot numbers correspond to analysis number listed in Table 6. Spots with cracks or holes are indicated in red; these were not plotted in Fig. 14.

Fig. EA30. BSE images of fayalite grains in MET 96503, *14* measured for oxygen isotopic compositions. The spot numbers correspond to analysis number listed in Table 6.

Fig. EA31. BSE images of magnetite grains in Ngawi, USNM2843-2 measured for oxygen isotopic compositions. The spot numbers correspond to analysis number listed in Table 6. White numbers in black filled circles correspond to SIMS spots acquired using FC-EM-EM. Spots with cracks or holes are indicated in red; these were not plotted in Fig. 14. met = Fe,Ni-metal; mgt = magnetite; sf = sulfide.

Fig. EA32. BSE images of fayalite grains in Ngawi, UCLA44 measured for oxygen isotopic compositions. The spot numbers correspond to analysis number listed in Table 6. Spots with cracks or holes are indicated in red; these were not plotted in Fig. 14.